Università degli Studi di Ferrara

DOTTORATO DI RICERCA IN
FISICA

CICLO XXII

COORDINATORE Prof. Filippo Frontera

Manipulation of charged particle beams through coherent interactions with crystals

Settore Scientifico Disciplinare FIS/01

Dottorando
Dott.Andrea Mazzolari

Tutore
Prof. Vincenzo Guidi

Anni 2007/2009

Index

1. Coherent interactions between charged particles and crystals
    1.1. Channeling
    1.2. The continuum potential approximation
    1.3. Particle motion in the field of atomic planes and axes
        1.3.1. Motion under planar channeling
        1.3.2. Motion under axial channeling
    1.4. Motion in a bent crystal
    1.5. Volume Reflection (VR) and Volume Capture (VC)
    1.6. Multiple Volume Reflection in One Crystal (MVROC)
    1.7. References
2. Fabrication and bending of crystals for channeling
    2.1. Strip like crystals fabrication
        2.1.1. Isotropic etching
        2.1.2. RBS and Channeling-RBS
        2.1.3. RBS-Channeling
    2.2. Anisotropic etching
    2.3. Crystal bending
        2.3.1. Anticlastic deformation in an anisotropic material
        2.3.2. Simulation and experimental
        2.3.3. Holders for strips and multi-strips crystals.
    2.4. A crystals for low energy negative particles channeling
    2.5. References
3. Coherent interactions between positively charged particles and crystals
    3.1. The experimental setup
        3.1.1. Silicon microstrip detectors
        3.1.2. The goniometer
    3.2. Setting up
        3.2.1. Crystal pre-alignment
        3.2.2. Lateral alignment
        3.2.3. Torsion compensation
    3.3. Planar channeling in short bent crystals.
    3.4. Deflection of 400 GeV proton beam by means of axial channeling
    3.5. Single volume reflection in a single crystal
    3.6. Volume reflection dependence on crystal bending radius
    3.7. Multiple volume reflections
        3.7.1. Multiple volume reflections in QM-like crystals
        3.7.2. MVR in multistrip crystals
        3.7.3. Multiple volume reflection in a single crystal
    3.8. Discussion
    3.9. References

4. Coherent interactions between negatively charged particle beams and crystals
    - 4.1. Planar channeling and VR of negative particles
    - 4.2. Deflection of negative particles by axial channeling
    - 4.3. Emission of radiation in the VR process
        - 4.3.1. Radiation from bent crystals
        - 4.3.2. Experimental setup
        - 4.3.3. The spectrometer method
        - 4.3.4. The amorphous contribution
        - 4.3.5. VR Spectra
    - 4.4. Discussion
    - 4.5. References

Introduction

In the last years, the field of channeling and related phenomena aimed to particle-beam steering has received a tremendous impulse by the advent of a new generation of silicon crystals, which resulted in significant performance increase and lead to the discovery of novel phenomena.

The first key factor was the usage of silicon crystals exploiting secondary deformations, which provide extremely uniform bending an optimal sample thickness across the beam. Moreover, the holder to impart the primary curvature is designed to keep apart all the material but silicon from the trajectory of the beam.

A second key factor which lead to performance improvement is the quality of the crystal surfaces by using properly tailored chemical etchings. In particular, the entry face of the crystal plays an important role, because it is the surface accepting incoming beam particles.

Lastly, significant contribution was due to the characterization of the samples with a variety of techniques. A thorough characterization allows fine adjustment of the experimental parameters for crystal fabrication and certification of its quality prior to installation in the accelerator.

In this thesis it will be shown the procedures for manufacturing of crystal realized at Sensors and Semiconductor Laboratory of Ferrara University. The fabrication methods, based on revisitations of micromachining techniques, allow obtaining high quality crystals, which lead to performance increase as well as to the discovery of new effects in the interaction with positively and negatively charged particle beams at CERN facilities.

As it will be shown in this thesis, the geometry and the quality of the realized crystals allowed attaining a record 83% efficiency when operated to deflect a 400 GeV proton beam at the H8 line at CERN by means of planar channeling and contributed to the observation of volume reflection.

The same crystal generation enabled to observe multiple volume reflection in both a series and in a single crystal and to successfully achieve deflection of negatively charged particle beams through either channeling or volume reflection.

Coherent phenomena in crystals may be the basis for halo collimation for current hadron colliders (e.g. the LHC). An efficient collimation system is a necessary condition to run the accelerator at its top luminosity and to prevent damage of its sophisticated superconductive magnets. This smarted collimation scheme is currently being under investigation in the pilot UA9 experiments, which investigate crystal-assisted schemes for halo collimation in the CERN SPS through channeling of protons. The first and preliminary results of UA9 experiment shows good perspectives on the possibility to collimate the LHC beam by using bent crystals.

Chapter 1

Coherent interactions between charged particles and crystals

1.1. Channeling

A large variety of physical phenomena may occur in interaction between charged particles and matter. For example Rutherford scattering, energy loss, nuclear reactions, x-ray production etc…If the target material is homogenous and isotropic the impact parameter of any interaction is independent of the orientation between particle beam and target. When the target material is monocrystalline the yields of physical processes and the impact parameters are function of orientation between target and particle beam. This is due to the so called "channeling" effect. From an intuitive point of view if the particle impinge on the crystal not so close to the atomic planes, in order to prevent strong interaction with nuclei, and with direction close to planes (planar channeling) or an axis (axial channeling), with high probability it will be subject to correlated scattering events on the atomic planes. Because of the periodic crystal structure the particle will undergo a series of small-angle collisions, resulting in a steering effect which causes the particle to oscillate between atomic planes or wander among crystal axis, leading to a reduction of close-encounter related events.

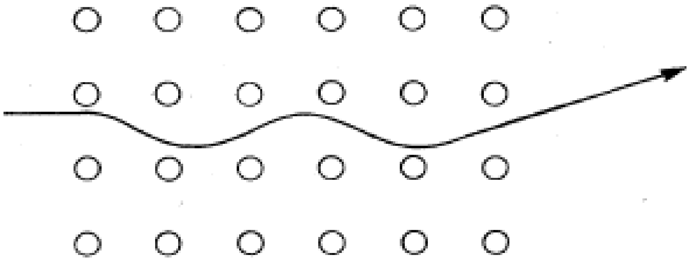
Figure 1.1: schematic representation of planar channeling

Channeling was discovered during low energy ions implantation and by computer [1.1]simulations, which consider this effect as unwanted because it alters the desiderate ions implantations profile and then theoretically studied by Lindhard [1.2] and experimentally beams from Van der Graaf accelerators as tools for materials characterization[1.3]. Based on the ideas from Tsyganov [1.4] to deflect high energy particles beam using bent crystals, high energy channeling have been investigated by different institutes in USSR, USA, CERN. Apart from the possibility to deflect high energy particle beam, different subjects have been investigated in such experiments, like channeling radiation [1.5-8], bremsstrahlung radiation [1.8-11], life time of short lived particles[1.12], pair creation [1.13-15], beam extraction [1.16-19], beam collimation, [1.20] measurements of particles magnetic momentum [1.21-23], radiation damage [1.24-25]. A new generation of experiments recently carried on at CERN characterized by the use of short bent crystals and high resolution detectors allowed to discover new effect which were not previously discovered and which will be described in this thesis.

1.2. The continuum potential approximation

The potential describing the interaction between an ion (atomic number Z_1) and an isolated atom (atomic number Z_2) can in general be expected to be a quite complicated function of several parameters such as the masses, the distance between ion and atom, the relative velocity, the atomic numbers and the impact parameter. In order to simplify the problem it is usual to assume a two-body like interaction and it is neglected any velocity dependence of the atom-ion interaction potential. This is a reasonable assumption keeping in mind that channeling interactions are "gentle" small-angle. Under such assumption the interaction can be described by a static potential similar to the one of diatomic molecules. This still remain a complex problem to be treated theoretically, involving a Hartree-Fock approach. In order to further simplify the ion-atom potential a well working approximation consist in modeling the interaction potential following the Thomas-Fermi model, where the interaction potential is given by

$$V(r)=\frac{Z_i Ze^2}{r}\phi\left(\frac{r}{a_{TF}}\right) \tag{1.1}$$

Here r is the distance between the particle and the atom, $a_{TF}=0.8853a_0(Z_1+Z_2)^{-1/3}$ and a_0 is the Bohr radius. The term $\phi(r/a_{TF})$ is a screening function which takes into account the charge distribution of the atom. The Thomas-Fermi approach cannot take into account such detailed features as electronic shell structure of the atoms, but it is a good approximation to Hartree-Fock calculations. A widely used analytical form for ϕ is given by Molière [1.26]

$$\phi(r/a_{TF})=\sum_{i=1}^{3}\alpha_i e^{-\frac{\beta_i r}{a_{TF}}} \tag{1.2}$$

,

where α=(0.1;0.55;0.35) and β=(6.0;1.2;0.3). An alternative form for ϕ is given by Lindhard [1.2],

$$\phi(r/a_{TF})=1-\left(1+\left(\frac{Ca}{r}\right)^2\right)^{-1/2} \tag{1.3}$$

Where C is a standard constant with value of $\sqrt{3}$.

From a classical point of view a particle is channeled if it is incident on the row or plane at an angle below the "critical angle", i.e. an angle small enough so as not to feel the individual atom potential, but an averaged one[1.27]. Lindhard showed [1.2] that for incidence close to an axis (axial channeling) this angle is given by $\psi_a=(2Z_1Z_2e^2/dE)^{1/2}$ while for incidence close to a plane (planar channeling) we have $\psi_p=(2\pi nZ_1Z_2e^2a/E)^{1/2}$ where d is the spacing in the atomic row, E is the particle energy, n the atomic areal density. Under this assumption we may consider the motion of the particle as the motion in an averaged potential. Considering a particle at distance ρ from an atomic row we have

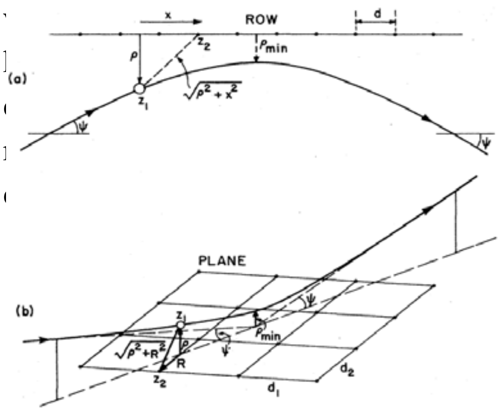

Figure 1.2: a collision of channeled particle with axis (a) or plane (b)

$$V = \frac{1}{d}\int_{-\infty}^{\infty} V[(\rho^2 + x^2)^{1/2}]dx \qquad (1.4)$$

while for the planar case we have

$$V_P(x) = n\int_{0}^{\infty} 2\pi R V(x^2 + R^2)^{1/2}\, dR \qquad (1.5)$$

is the distance between the ion and an atom of the plane, see Fig. [1.2].

The potential experienced by the ion will be the sum of the potentials of all the atomic rows in the axial channeling regime, and of all the planes in the planar mode. Axial potential is the total potential at a point r in the plane normal to the axis, i.e.

$$U_R(\boldsymbol{\rho}) = \sum_i V_R(|\mathbf{r} - \boldsymbol{\rho}_i|) - U_R^{\min} \qquad (1.6)$$

where $\boldsymbol{\rho}_i$ are the positions of the atomic rows measured in the plane normal to the axis and $U_R^{\min}$ is a constant subtracted in order to make the minimum value of $U_R(\boldsymbol{\rho})$ equal to zero. For the planar potential we have

$$U_P(\mathbf{x}) = \sum_i V_P(|\mathbf{r} - \mathbf{x_i}|) - U_P^{\min} \qquad (1.7)$$

In Fig [1.3] the planar and axial potentials for silicon for planes (110) and axis <111> respectively are represented.

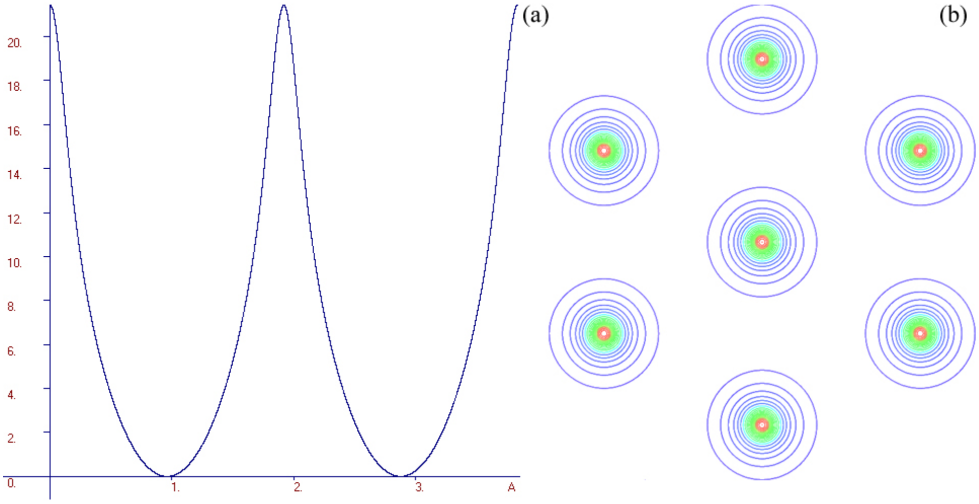

Eq (1.1) planar potential for (110) silicon planes, (b) axial potential for <111> axis.

1.3. Particle motion in the field of atomic planes and axes

Channeled particles travels at small angles with respect to atomic rows or planes, so interactions with atoms of the crystal may be consider as elastic. Neglecting energy losses the longitudinal component of the momentum may be treated as constant.

1.3.1 Motion under planar channeling

Let's consider as first the motion of a particle under planar channeling moving in the potential *U(x)*, we have:

$$E=\sqrt{p_x^2c^2+p_z^2c^2+m^2c^4}+U(x)=const \qquad \text{Eq (1.2)}$$

Remembering that the angle $\vartheta=p_x/p_z$ is small, we may write

$$\frac{p_x^2c^2}{2E_z}+U(x)+E_z=const \qquad \text{Eq (1.3)}$$

where $E_z=\sqrt{p_z^2c^2+m^2c^4}$. The sum of the first two terms of the last relation is often regarded as "transverse energy" in the literature. Since p_z is constant it is easy to show that transverse energy is conserved, i.e.

$$E_T=\frac{p_x^2c^2}{2E_z}+U(x)=\frac{p_z^2c^2}{2E_z}\vartheta^2+U(x)=const \qquad \text{Eq (1.4)}$$

Assuming $E_z\approx E$ and remembering that $pc^2=vE$ where v is the particle velocity, we have

$$E_T=\frac{pv}{2}\theta^2+U(x)=const \qquad \text{Eq (1.5)}$$

Considering that

$$\theta=\frac{p_x}{p_z}=\frac{v_x}{v_z}=\frac{d_x}{d_z} \qquad \text{Eq (1.6)}$$

for any potential *U(x)* we may calculate the particle trajectory integrating the equation

$$dz=\frac{dx}{\sqrt{\frac{2}{pv}[E_T-U(x)]}} \qquad \text{Eq (1.7)}$$

Differentiating (1.7) with respect to *z* we obtain

$$pv\frac{d^2x}{dz^2}+U'(x)=0 \qquad \text{Eq (1.8)}$$

approximating the *U(x)* potential with an harmonic shape

$$U_h(x)=U_0\left(\frac{2x}{d_p}\right)^2 \qquad \text{Eq (1.9)}$$

Eq. (1.8) describes an harmonic motion and particle motion is described by the equations

$$x = \frac{d_p}{2}\sqrt{\frac{E_T}{U_0}}\sin\left(\frac{2\pi z}{\lambda}+\varphi\right)$$
$$\vartheta = \sqrt{\frac{2E_T}{pv}}\cos\left(\frac{2\pi z}{\lambda}+\varphi\right) \qquad \text{Eq (1.10)}$$

with

$$\lambda = \pi d_p\sqrt{\frac{pv}{2U_0}} \qquad \text{Eq (1.11)}$$

In planar channeling particles regime oscillates between atomic planes, for example for channeling among (110) silicon planes the oscillation period has an average value of 58 μm at 400 GeV.

During the passage through the crystal, some particles may leave their bound states due to multiple Coulomb scattering both on the nuclei (MSN) and electrons (MSE) of the crystal atoms (dechanneling process). The particle scattering on the crystal nuclei occurs in a "nuclear corridor" near the crystal planes, around which the atomic nuclei vibrate due to thermal energy. The vibration induces a Gaussian distribution $P_n(x) \sim \exp(-x^2/u_\perp^2)$ of the effective transverse distance x of the nuclei from the planes, where $u_\perp = \sqrt{2}u_1$ and u_1 is the amplitude of the thermal vibrations at the operational temperature. The amplitude u_1, which is the measure of the "nuclear corridor" width, is much smaller than the channel width d_p for the main crystal planes. For instance, for (110) silicon channels at the room temperature one has $6u_1/d_p=0.23$. Particles approaching too close, i.e. at a distance less than the so called "critical approach distance" are readily dechanneled due to MSN. Experimental data show that a good approximation for the critical approach distance is $r_c=2.5u_1$ [1.28].

This factor also limits the capture efficiency in channeling states at the entry face in the crystal to a maximum value of

$$P_c = 1 - 2r_c/d_p = 0.805 \qquad \text{Eq (1.12)}$$

Particles impinging on the crystal entry face at a distance with respect to the atomic planes less than r_c are readily dechanneled due to scattering from atomic nuclei. The initial transverse energy of these particles is larger than the critical value $E_{xc}=U_{ef}(r_c)$. The MSN produces a rapid increase of the transverse energy, hence the particle dechannel. The probability of such a process grows exponentially with the distance l from the crystal entry face with a typical constant L_n called nuclear dechanneling length. The value of L_n is proportional to the quantity U_{ob}-E_{xc}[1.29]. Particles with an initial transverse energy smaller than the critical value E_{xc} can be also dechanneled due to multiple scattering on the electrons of the crystal atoms (MSE). The electron dechanneling probability also increases exponentially with the ratio l/L_e, where L_e is the electron dechanneling length. For 400-GeV/c protons in a straight (110) silicon crystal L_e is about 20 cm according to the extrapolation of the available data [1.7]. In addition, for positive particles under planar channeling it can be found [1.30] that

$$L_e \simeq \frac{256}{9\pi^2}\frac{pv}{\ln(2m_ec^2\gamma/I)-1}\frac{a_{TF}d_p}{Z_ir_em_ec^2} \qquad \text{Eq (1.13)}$$

The nuclear dechanneling length L_n is much shorter than the electron dechanneling length L_e, i.e. $L_n << L_e$.

In long crystals with a length $L >> L_n$, in a simplified scenario, particles with an initial transverse energy E_{xo} in the range $E_{xc} < E_{xo} < U_{ob}(R)$ are quickly dechanneled due to the MSN. Particles with $E_{xo} < E_{xc}$ are dechanneled due to the MSE all along the crystal length. The initial part of the crystal dominated by the MSN has a negligible length. For this reason, the particle dechanneling in long crystals is characterized by a dechanneling length, which is well approximated by the electron dechanneling length, i.e. $L_d \approx L_e$.

1.3.2 Motion under axial channeling

As previously described, particles incident on a crystal aligned with a crystalline axis may be subject to axial channeling provided that their incidence angle is less than a critical one. With good approximation it is possible to consider the potential of an isolated string as

$$U(\rho) = \frac{Z_i Z e^2}{a_i} \ln\left(1 + \frac{3a_{TF}^2}{(\rho+u)^2}\right) \qquad \text{Eq (1.14)}$$

Where a_i is the interatomic spacing in the string and ρ the distance from the string. In this case we have conservation of trasversal energy E_T and of angular momentum J.

Considering a particle incident on a crystal axis at angle Ψ, then $\Psi\rho = d\rho/dz$ and $\Psi\varphi = \rho d\varphi/dz$ are the projections toward the axis and perpendicular to it. The angular momentum is $J = p\Psi\varphi\rho = p\rho^2\, d\varphi/dz$, so we may write

$$E_T = \frac{pv}{2}\psi^2 + U(\rho) = \frac{pv}{2}\left(\frac{d\rho}{dz}\right)^2 + \frac{J^2}{2M\gamma\rho^2} + U(\rho) \qquad \text{Eq (1.15)}$$

From the last equation we find

$$z = \int \frac{d\rho}{\sqrt{\frac{2}{pv}[E_T - U(\rho)] - \frac{J^2}{p^2\rho^2}}} + const \qquad \text{Eq (1.16)}$$

Considering that $d\varphi = (J/pr^2)dz$ we have

$$\phi = \int \frac{\frac{J}{r^2}dr}{\sqrt{2M\gamma(E_T - U(r)) - \frac{J^2}{r^2}}} + const \qquad \text{Eq (1.17)}$$

The last two equations defines the motion of a particle subject to axial channeling.

1.4. Motion in a bent crystal

Intuitively if particles are channeled in a bent crystal, they will follow the bending of planes or axis provided that the centrifugal force acting on the particle does not overcome the force confining the particle between the atomic planes or axis. This idea was first proposed by Tsyganov in 1976 [1.4] and experimentally confirmed in Dubna in 1979 [1.31].

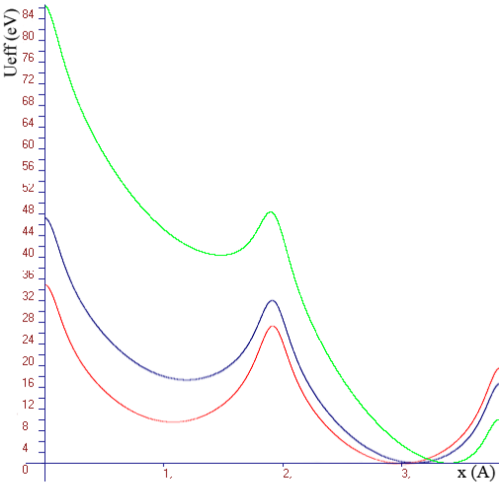

Figure 1.4: planar potential for (110) silicon planes bent at radius 2 (green), 5 (blue), 10 (red) m

Let's consider particles channeled in a bent crystal. Due to the presence of a centrifugal force, the equation of motion in a system comoving with the particle becomes

$$pv\frac{d^2x}{dz^2}+U'(x)+\frac{pv}{R(z)}=0 \qquad \text{Eq (1.18)}$$

Assuming that the bending radius is constant we have

$$pv\frac{d^2x}{dz^2}+U'(x)+\frac{pv}{R(z)}=0 \qquad \text{Eq (1.19)}$$

This means that we may consider the particle moving in a effective potential

$$U(x)=U(x)+\frac{pv}{R}x \qquad \text{Eq (1.20)}$$

In Fig. [1.4] the Silicon (110) planar potential is plotted for different bending radius. Increasing the bending radius the depth of the potential well decreases, and its minimum becomes closer to the atomic planes. In correspondence of the "critical radius" [1.4],

$$R_c=\frac{pv}{U'(x_c)}=\frac{pv}{\pi Nd_pZ_iZe^2} \qquad \text{Eq (1.21)}$$

where $U'(x_c)$ is the interplanar electric field calculated at the critical approach distance x_c, the well disappears and channeling is no more possible. Bending of the crystal lowers the depth of the potential well, decreasing the dechanneling length from the value $L_e(R)=L_e(\infty)$ to $L_e(R)\,\square\,L_e(\infty)(1-R_c/R)^2$, where $L_e(\infty)$ is the dechanneling length for a flat crystal

Particle deflection by axis is achieved by means of "hyperchanneling" and "doughnut-scattering" mechanisms. While in planar channeling a channeled particles travels between adjacent atomic planes, the majority of axially channeled particles are free to wander between atomic strings. Particles with no enough transversal energy do not pass from an atomic string to another one is defined "hyperchanneled". Such particle follows the bent axis. Deflection by axes is possible also through the "doughnut-scattering" mechanism. Particles which enter in the crystal aligned to the axis are subject to an equalization of transversal momentum around the axis over a length λ. After such length the particle distribution in the angle space appears as a ring (doughnut) with a radius equal to the critical angle. Particles not subject to hyperchanneling (over barrier particles) can be deflected by crystal axis through the doughnut-scattering mechanism provided that the "Shulga-Greenenko" condition [1.32-33] is satisfied, i.e. that

$$k = \frac{\lambda L}{(R\psi)^2} < 1 \qquad \text{Eq (1.22)}$$

where L is the crystal thickness, R the bending radius and Ψ the axial critical angle. Assuming that such condition is fulfilled it is possible to achieve high efficiency deflection of the axial-channeled beam by means of both hyperchanneling and doughnut-scattering mechanism.

1.5. Volume Reflection (VR) and Volume Capture (VC)

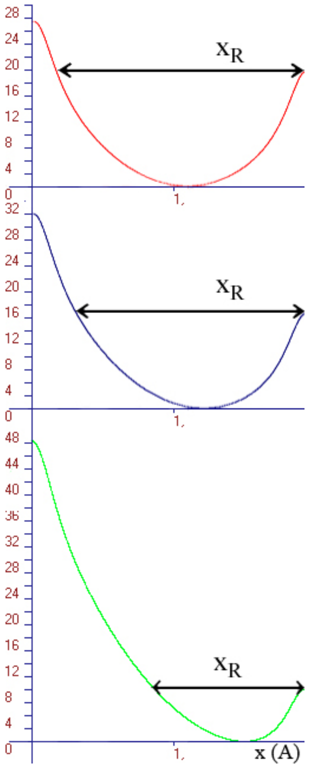

Figure 1.5: Changing of potential well shape and depth as function of crystal bending radius. x_r is the interplanar region available for channeling

Let us consider a bent crystal and a charged particle impinging on it. If the particle's trajectory is aligned within the critical angle with crystal planes it is captured in channeling regime. Taratin [1.29, 34], by using computer simulations found that quasi-channeled particles, corresponding to such particles entering in the crystal at a distance smaller than the distance x_r which defines the critical transverse energy for channeling, (see Fig [1.5]), are subject to Volume Capture (VC) or Volume Reflection (VR). Later, an analytical description of the VR process have been suggested by Maisheev [1.35]. Let us consider particles impinging on the crystal aligned with the crystal planes as in Fig [1.5] and at a distance with respect to the atomic planes less than the critical approach distance. A small fraction of particles, labeled as (1), are captured in channeling states (Volume Capture) due to dissipative processes which leads to a noticeable loss of transverse energy. The remaining fraction, labeled as (2), is subject to volume reflection, i.e. are deflected on the opposite side of the crystal bend. Deflection angle is comparable with the channeling critical angle.

Now let us consider the case that the crystal is aligned with respect to the particle beam in such a way that the particle trajectory becomes tangent to the crystal planes inside the bulk of the crystal, as in Fig. [1.6](b). Such particles will fall in quasi-channeling states inside the bulk of the crystal. Particles labeled as (1) are volume captured inside the volume of the crystal, while particles labeled as (2) are volume reflected of a quantity approximately 1.5 θ_c.

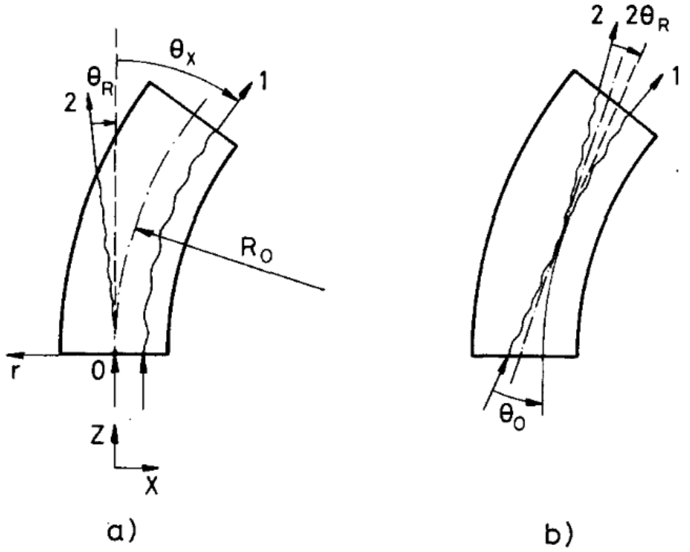

Figure 1.6 (a) particles subject to VR at the entrance on the crystal (b) particles subject to VR in the crystal bulk.

While VC has been used to increase the angular acceptance in channeling regime, and both experimentally [1.36-38] and theoretically [1.39-40] deeply studied in 1980 years, VR have been experimentally discovered only in recent experiments [1.41] and its features and peculiarities understood in experiments which will be described in this thesis. VC efficiency increases as decreasing beam energy [1.42]. Being VC antagonist to VR process the last one becomes highly efficient at high beam energy. For high energy particle beam manipulation VR offers big advantages with respect to channeling, providing a larger acceptance, (equal to the crystal bending radius) and efficiency close to 100%. In spite of this, the deflection angle is not so strongly dependant on crystal bending radius as it is for channeling and is comparable to the channeling critical angle.

Fig 1.7 summarizes interactions which can happen between a charged particle and a crystal. In Fig 1.7a-b straight crystal interacts with charged particles, which may see the crystal as an amorphous material or may be captured under channeling regime (only planar regime is shown for simplicity). In this case they will oscillate between the confining atomic planes with average period λ. If the crystal is bent as in Fig 1.7b-c and the particle trajectory becomes tangent to the crystalline planes inside the volume of the crystal it may be captured under channeling regime in the crystal bulk or it may undergo volume reflection.

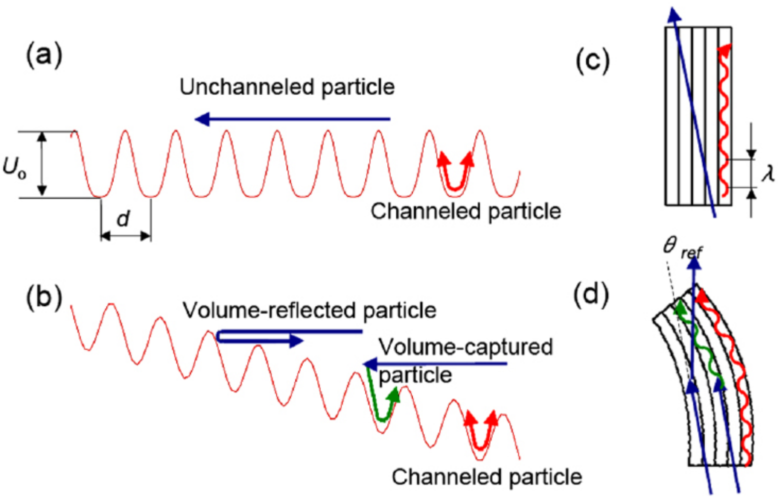

Fig 1.7 Periodic planar potential in a straight crystal for positively charged particles. The arrows show a channeled particle with oscillatory motion in the potential depth and a nonchanneled particle, whose transverse energy is greater than the depth of the potential well *Uo*. (c) Schematic representation of the particle trajectories in a straight crystal. (b) Periodic planar potential in a bent crystal for positively charged particles. The arrows show volume-reflected, volume-captured, and channeled particles. (d) Schematic representation of the particle trajectories in a bent crystal.

In order to amplify the deflection angle it is possible to use a sequence of crystals properly disposed in such a way to multiply the deflection of each crystal (Multiple Volume Reflection from a sequence of crystals) or it is possible to use multiple volume reflection in one crystal (MVROC), which will be described in the following paragraph.

1.6. Multiple Volume Reflection in One Crystal (MVROC)

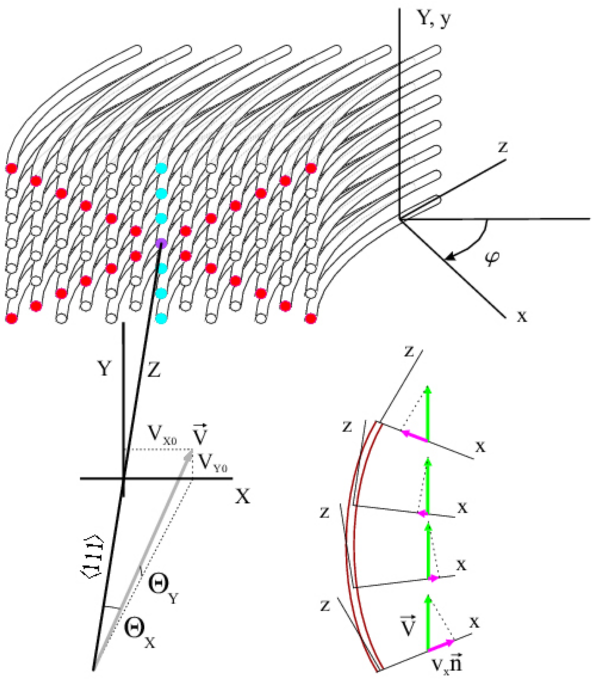

Figure 1.7 Rapresentation of a particle incident on bent silicon crystal close to <111> axis. *XYZ* is the laboratory reference system, while *xyz* is comoving with the particle and the *z* axis is always tangent to che crystal bent planes. Particle *x* component changes along the crystal, so the the vector (v_x,v_y) may become tangent to different planes

Under proper alignment between particle beam and crystal axis it is possible to excite VR from both crystal main plane and skew planes. This leads to multiple volume reflection in a single crystal, whose peculiarity is an increase of deflection angle and deflection efficiency about 90%. Let us consider a bent Silicon crystal with <111> axis and (110) channeling planes. Let the reference system *xyz*, oriented as in Fig. 1.7, be commoving with the impinging particle. Let us assume XYZ as a laboratory reference system. We consider the motion of the charged particle in the transversal *xy* plane. In laboratory frame the horizontal particle velocity is function of the position in the crystal, we have infact $v_x=v_x(z)=V_x-V\varphi(z)$, $\varphi(z)=z/R<<1$. Differently, the vertical particle velocity is constant,

$v_y=V_y$.

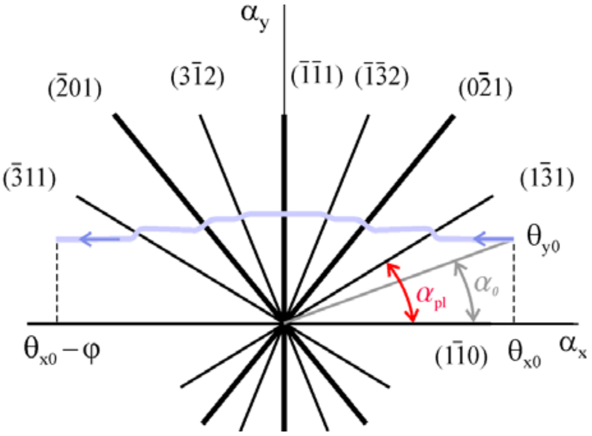

Fig 1.8 a particle incident at angles Θ_{x0}, Θ_{y0} is subsequently reflected by skew planes and main plane. Vertical deflecions due to skew planes cancels each other, while deflections along horizontal directions sum up increasing deflection angle.

Due to changes in the horizontal component of velocity, under proper alignment between crystal and particle beam the particle transversal velocity (v_x, v_y) may become tangent to the skew planes, allowing VR from them. Reflection from skew planes will be characterized by deflection in both horizontal and vertical directions as Fig. 1.8 depicts. Deflection angles are given by $\vartheta_x=-\vartheta_R * cos a$ and $\vartheta_y=-\vartheta_R * cos a$ where α is the inclination angle of the plane, and ϑ_R is the deflection angle for a single VR from the given skew plane bent at radius $R/sin(\alpha)$. Since cos $(\pi-\alpha)$=-cos α and sin $\alpha>0$ for any $0<\alpha<\pi$, choosing the horizontal incidence angle such that $\theta_{X0}\approx V_{X0}/V=\varphi/2$ horizontal deflections sum up, while vertical deflections from symmetrical skew planes cancels each other. In order to involve in the VR process the largest number of skew planes it necessary to minimize the angle $\theta_{Y0}\approx V_{Y0}/V$. However such an angle should not be too small, otherwise particle will be subject to interaction with be volume captured by crystal axis instead of interacting with crystal planes. In order to exactly determine this angle it is necessary to realize simulations of the particle motion in the bent crystal, in any case a good criterion is to keep Θ_{Y0} larger than about 4-5 times the axial critical angle.

To involve the reflection from a plane with inclination α_{pl} a particle should impinge on the crystal at an angle α_0=arctan$(V_{Y0}/V_{X0})>\alpha_{pl}$ Due to this, the crystal bending angle has to satisfy the condition

$$\varphi=2\frac{V_{X0}}{V}=2\frac{V_{X0}}{V_{Y0}}\vartheta_{Y0}=2\vartheta_{Y0}\cot\alpha_0>2\vartheta_{Y0}\cot\alpha_{pl} \qquad \text{Eq (1.23)}$$

For example, if we consider the skew planes $(\bar{1}01)$ and $(0\bar{1}1)$ for which α_{pl}=30° we have $\varphi>3.46\,\Theta_{Y0}$. While for single volume reflection in a single crystal interaction is realized in the interaction with only the main plane, multiple volume reflection in a single crystal is due to interaction with many planes and involves alignment of the crystal in both horizontal and vertical directions. As a consequence the deflection angle depends on the vertical positioning of the crystal, which may allow or not interaction with some of the skew planes. In particular, deflection angle increases as the number of skew planes involved in the interaction with the crystal. In the best conditions multiple volume reflection in a single crystal allows to amplify the deflection angle up to a value of about 5 times the angle obtainable by single volume reflection. Acceptance of the phenomena at full deflection angle is not simply given by crystal bending angle and to predict it simulations are needed. For example it is predicted by simulations that for 400 GeV protons subject to multiple volume reflection in a single crystal of thickness 4 mm and bending angle 400 μrad [1.43] acceptance is about 80 μrad in the horizontal direction, and 50 μrad in the vertical one.

References

[1.1] Piercy G. R. *et al.*, Phys. Rev. Lett. **10** 399 (1963)

[1.2] Lindhard J., K. Dan. VVidensk. Selsk. Mat. Fys. Medd. **34** 1 (1965)

[1.3] Feldman L. C. *et al.*, *Materials Analysis by Ion Channeling: Submicron Crystallography*. 1982, Riverport Academic Press.

[1.4] Tsyganov E. N., Fermilab Preprint TM-682, TM-684 Batavia (1976)

[1.5] Filatova N. A. *et al.*, Phys. Rev. Lett. **48** 488 (1982)

[1.6] Filatova N. A. *et al.*, Nucl. Instr. and Meth. . **194** 239 (1982)

[1.7] Carrigan R. A. and Ellison J., eds. *Relativistic Channeling, pag 39*. 1987, Plenum Press: New York.

[1.8] Andersen J. U. *et al.*, Phys. Scr. **24** 588 (1981)

[1.9] I. A. Grishaev G. D. K. a. B. I. S., Sov. Phys. JETP. **45** 229 (1977)

[1.10] Palazzi G. D., Rev. Mod. Phys. **40** 611 (1968)

[1.11] Timm U., Fortschr. Phys. **17** 765 (1969)

[1.12] Carrigan R. A., Phys. Rev. Lett. **35** 306 (1975)

[1.13] Belkacem A. *et al.*, Phys Rev. Lett. **54** 2667 (1985)

[1.14] Belkacem A. *et al.*, Phys. Rev. Lett. **53** 2671 (1984)

[1.15] Cue N. and Kimball J. C., Nucl. Instrum. Methods Phys. Res. B. **2** 29 (1984)

[1.16] Asseev A. *et al.*, Phys. Rev. ST Accel. Beams. **1** 22801 (1998)

[1.17] Murphy C. T. *et al.*, Nucl.Instrum.Meth.B. **119** 231 (1996)

[1.18] Carrigan R. A. *et al.*, Nucl. Instr. Meth. **90** 128 (1994)

[1.19] Afonin A. G. *et al.*, Nucl. Instr. Meth. B. **234** 14 (2005)

[1.20] Afonin A. G. *et al.*, Phys. Rev. Lett. **87** 094802 (2001)

[1.21] Baublis V. V. *et al.*, Nucl. Instr. Meth. B. **90** 150 (1994)

[1.22] Chen D. *et al.*, Phys. Rev. Lett. **69** 3286 (1992)

[1.23] Khanzadeev A. V. *et al.*, Nucl. Instr. Meth. B. **119** 226 (1996)

[1.24] Wang G. H. *et al.*, Nucl. Instr. and Meth. **218** 669 (1983)

[1.25] Baker S. I. *et al.*, Nucl. Instr. and Meth. B. **90** 119 (1994)

[1.26] Molière G., Z. Naturforsch A. **2** 133 (1974)

[1.27] Leibfried C. L. G., J. Appl. Phys. **34** 2821 (1963)

[1.28] J.S.Forster, Nuclear Physics B **318**(1989)

[1.29] Taratin A. M. and Scandale W., Nucl.Instr.Meth. B **262** (2007)

[1.30] Biryukov V. M. *et al.*, *Crystal Channeling and Its Application at High-Energy Accelerators*. 1997 Berlin: Springer.

[1.31] Elishev A. A. *et al.*, Phys . Lett. B. **88** 387 (1979)

[1.32] Shulga N. F. and Greenenko A. A., Phys. Lett. B. **353** 373 (1995)

[1.33] Shulga N. F. and Greenenko A. A., Phys. Lett. B. **454** 161 (1999)

[1.34] Taratin A. M. and Vorobiev S. A., Nucl. Instrum. Methods Phys. Res., Sect. B. **512** 26 (1987)

[1.35] Maisheev V. A., Phys. Rev. ST Accel. Beams. **10** 084701 (2007)

[1.36] Andreev V. A. *et al.*, Pis'ma Zh. Eksp. Teor. Fiz. **36** 340 (1982)

[1.37] Andreev V. A. *et al.*, Pis'ma Zh. Eksp. Teor. Fiz. **39** 340 (1984)

[1.38] Andreev V. A. *et al.*, Pis'ma Zh. Eksp. Teor. Fiz. **44** BII (1986)

[1.39] Taratin A. M. and Vorobiev S. A., Zh. Theor. Fiz. **55** 598 (1985)

[1.40] Sumbaev D. I., Zh. Eksp. Theor. Fiz. **54** 1352 (1968)

[1.41] Ivanov Y. M., Pis'ma Zh. Eksp. Teor. Fiz. **84** 372 (2006)

[1.42] Biryukov V., Phys. Lett. A. **205** 340 (1995)

[1.43] Tikhomirov V. *et al.*, Submitted to Jour. Appl. Phys.

Chapter 2

Fabrication and bending of crystals for channeling

In a first generation of high-energy channelling experiments it was employed silicon crystals because of the availability of this material as single crystals of high crystalline quality. Such crystals were some centimetre thick along the beam, and bent through mechanical bending devices which were not able to impart a uniform bending radius [5.1-7]. Crystal bending exploited a primary bending imposed to the crystal. With the aim to realize shorter crystals and to provide uniform bending radius, two new generations of crystals were realized. Bending mechanism of such crystals relies either on "anticlastic deformation" (AD) use exploited by strip-like crystals [5.8] or on the "quasi-mosaic" (QM) effect exploited by quasi-mosaic crystals [5.9]. Both of them manifests as secondary curvatures due to a main imposed primary bending. Such curvatures are a multiple of the imposed main one, and for this reason are easily adjustable and allows realization of bending devices which can be placed far from the particle beam.

A second distinctive feature of the new generation of crystals is a higher quality of the crystal surfaces, i.e. of the surface over which the beam impinges and of the surface parallel to the particle beam. In the following we will describe as first the crystals preparation technique, and then their bending, focusing in particular to the strip-like crystals realized at the Sensors and Semiconductors Laboratory of Ferrara University.

2.1. Strip like crystals fabrication

Crystal fabrication requires dicing of the sample starting from either a wafer or an ingot to size the crystal to the wanted dimensions. This operation is normally accomplished by mechanical cut of base material. Such operation alters the original quality of the crystal, leading to the formation of a superficial "dead layer" with a great number of defects and crystalline disorder, which does not act as an active layer for channeling. Typically, preparation of suitably shaped crystals involves dicing of all crystal surfaces, both normal (entry face) and parallel to the beam direction. In order to realize crystals of the highest crystalline quality, we studied and optimized two methods based on wet isotropic and anisotropic chemical etchings. Such methods are borrowed from micro-fabrication techniques of silicon, were revisited and adapted to the case of sample preparation for channeling.

Both the preparation methodologies stars from Silicon wafers with low "miscut", i.e. the misalignment between orientation of the optical wafer surface and the crystallographic planes. This requirement is needed to increase the crystal portion available for channeling and to facilitate pre-alignement of the crystal with respect to the beam, operation carried on with an optical system (see Cap 3). Miscut of the starting wafers is measured with a high resolution diffractometer (Philips MRD X-Pert PRO™) available at Physics Institute of Padova University. In particular, are selected crystals with miscut lower than 1 mrad.

2.1.1 Isotropic etching

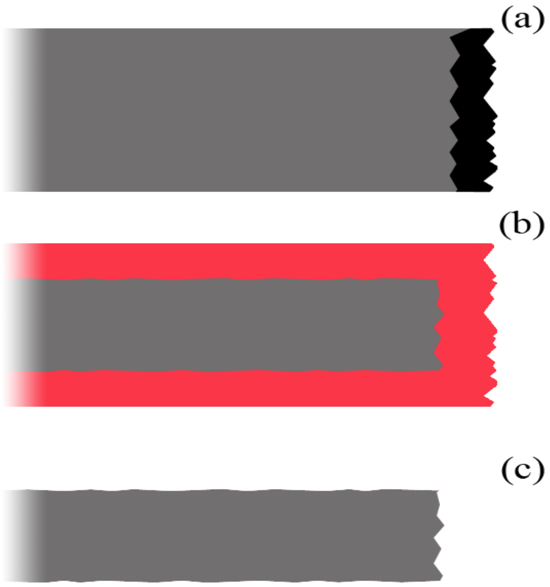

Figure 2.1 Removal of lattice damaged region induced by mechanical dicing. Region black in (a) rapresent damaged layer generated during crystal dicing. (b) The crystal is immersed in etchig solution, a layer of SiO_2 (red) is created on all the crystal surfaces. SiO_2 is removed by HF leaving a damage free crystal surfaces.

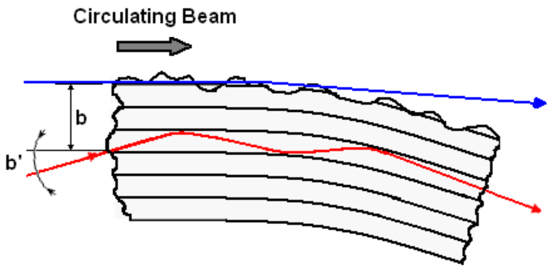

Figure 2.2 Schematic (not to scale) of the application of bent crystal for beam steering. The impact parameter b and the impinging angle of beam b′ are shown. The surface roughness R_a of the lateral face of the crystal (parallel to beam direction) is required to be lower than the impact parameter b (~ 100 nm for beam halo of LHC) for beam steering using the channelling effect.

A previous work [5.10] demonstrated that chemical etching was efficient for removal of the dead layer induced by mechanical dicing of the crystal surfaces. However, the process of etching resulted in significant roughness (R_a ~ 140 nm) of the surface in spite of its crystalline quality. Etching was conceived for application at the entry face of the crystal and thereby a relatively rough morphology was not a problem. On the strength of recently proposed usage of a crystal in modern hadron colliders and, in particular, of the constraint on the roughness of the lateral faces, an innovative methodology to treat the crystal's surface was developed. Crystals were diced from a commercially available wafer using a "Disco DAD 3220" dicer, equipped with fine-grit blade to minimize the mechanical damage during the cut. In such machine is mounted a gentle diamond blade with average grains size of 1μm and thickness 150 μm rotating at the speed of 30.000 rpm. The wafer to be diced is mounted on a chuck and held in position by vacuum. The rotating blade accomplishes cutting operations positioning on the wafer with micrometer resolution. In order to remove the damaged region induced by the cutting process, we etched the whole crystal in an acid solution made of HF, HNO_3, and CH_3COOH (HNA) [5.11]. Such etching mixture is widely used in silicon micromachining.Nitric acid readily oxidizes Si to SiO_2, which is eroded by HF, acetic acid serves as a solvent and makes the reaction more controllable. Such etching mixture is particularly suited to etch silicon isotropically, i.e. with the same rate independently of the crystallographic orientation. Silicon etching proceeds through the reaction

$$3Si + 12HF + 4HNO_3 \rightarrow 3SiF_4 + 4NO + 8H_2O$$

Acetic acid is used as a diluent, it lowers in fact the etch rate of the reaction, making it more controllable. There is not much difference between the use of water or acetic acid, but the last one is preferred because it results in less dissociation of the nitric acid, which preserves its oxidizing power over a wider range of dilution than water. From the tri-axial plot of Fig. 2.3 we gain the etch rate for any composition of the HNA etch solution. In the region of low HF concentration the etching process is diffusion-controlled, so different silicon materials are etched at the same rate. In the high HNO_3 region the process is surface controlled, so we have a light dependence of the etch rate as function of crystallographic orientation.

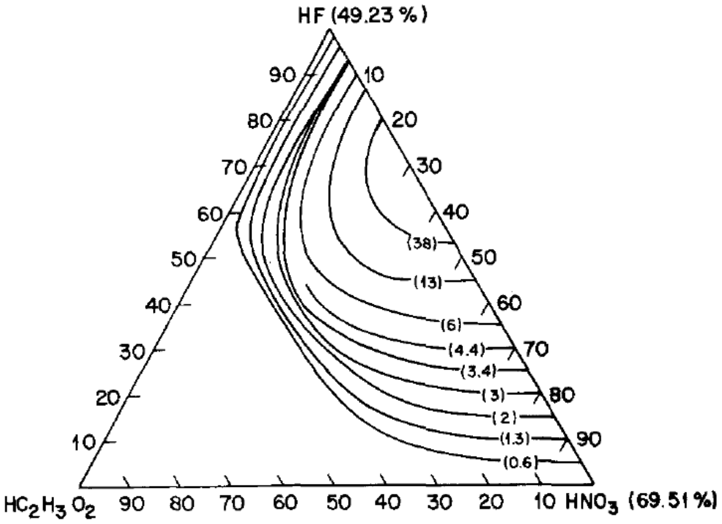

Figure 2.3 Iso-etch curves for silicon etch in HF:HNO_3 system, $HC_2H_3O_2$ (acetic acid) is used as diluent

The morphology and geometry of etched surfaces is dependent of the relative etchants concentrations as showed in Fig. 2.4, where the red spot corresponds to HNA concentrations used in the etching solution employed for samples preparation. Assuming that lattice damage affect the diced crystal in the same way independently of the crystalline direction and with the aim to obtain a low roughness of the surfaces parallel to the beam we choose a composition of the etching mixture made of 2 parts of HF, 15 parts of HNO_3 and 15 parts of acetic acid. This choice positions the HNA composition in a region of low HF concentration, and allows obtaining low roughness surfaces.

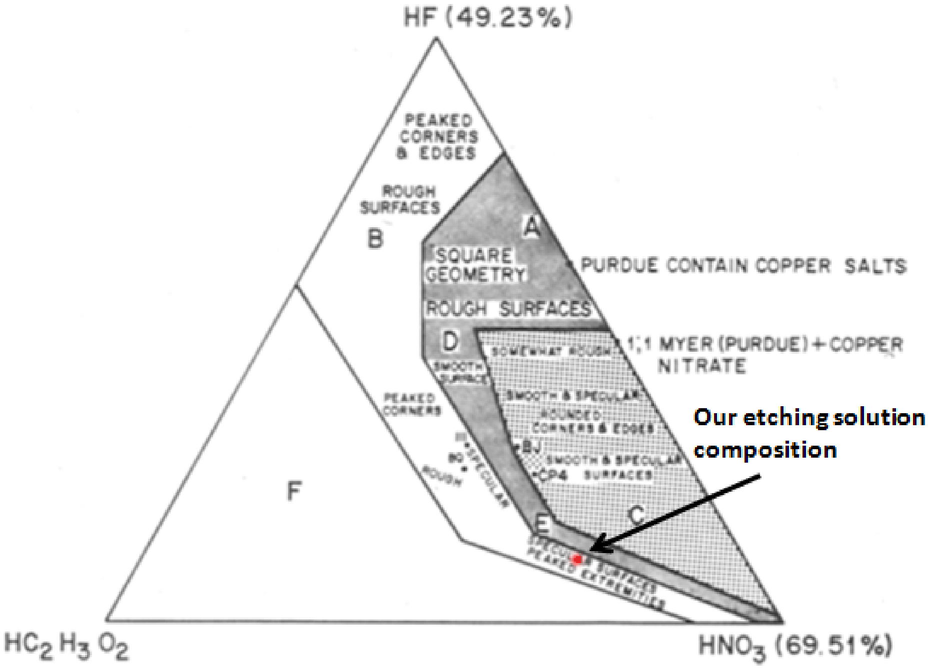

Figure 2.4 morphology of etched silicon crystals as function of HNA solution composition

After testing the solution on silicon wafers with different orientations we found that etch rate is 1 µm/min independently of crystal orientation. This confirmed that the etching solution isotropically etch silicon. The average size of the diamond grains contained in the dicing blade has size 1 µm, so it is reasonable that the lattice damage has an extension of the same order, so we choose and etching time of 2 min. The surface of the silicon crystals achieved through the procedure of dicing assisted by chemical etching was analysed from the standpoint of morphology and crystalline perfection, and compared to the surface just after the dicing process. Rutherford Back Scattering in Channelling condition (c-RBS) and Atomic Force Microscopy (AFM) were used for the purpose.

2.1.2. RBS and Channeling-RBS

Rutherford Backscattering (RBS) is a nuclear technique widely used to study composition of samples under analysis [5.12]. It is based on collisions between atomic nuclei and involves measuring the number and energy of ions in a beam which backscatter after colliding with atoms in the near-surface region of a sample at which the beam has been targeted. With this information, it is possible to determine atomic mass and elemental concentrations versus depth below the surface. In the case the target material is crystal, orienting it in channeling alignment (Channeling- RBS) it is possible to determine the crystalline quality. When a sample is bombarded with a beam of low energy particles, the vast majority of particles are implanted into the material and do not escape. Energy exchange occurs because of Coulombic forces between nuclei in close proximity to each other. However, the interaction can be modeled accurately as an elastic collision using classical physics. The energy measured for a particle backscattering at a given angle depends upon two processes. Particles lose energy while they pass through the sample, both before and after a collision. The amount of energy loss is dependent on that material's stopping power. A particle will also loose energy as the result of the collision itself. The collisional lost depends on the masses of the projectile and of the target atoms. The number of backscattering events that occur from a given element in a sample depend upon two factors: the concentration of the element and the effective size of its nucleus. For scattering at the sample surface the only energy loss mechanism is momentum transfer to the target atom. The ratio of the projectile energy after a collision to the projectile energy before a collision is defined as the kinematic factor.

$$K=\frac{E_{scattered}}{E_{incidend}}=\left(\frac{\left(1-\left(\frac{M_1\sin\theta}{M_2}\right)^2\right)+\frac{M_1\cos\theta}{M_2}}{1+\frac{M_1}{M_2}}\right)^2 \qquad (2.1)$$

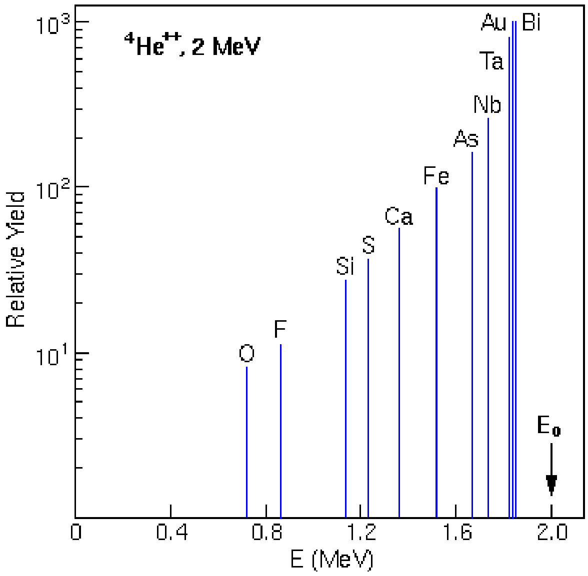

Figure 2.5 Relative yields for He backscattering from selected elements at an incident He energy of 2 MeV. The energies for He backscattering from these elements when present at the surface of a sample are also displayed. RBS is over 100 times more sensitive for heavy elements than for light elements, due to the larger scattering cross sections of the heavier elements.

Where E is ion energy, M_1 and M_2 are mass of incident ion and mass of target atom and θ is the scattering angle. From this relation it's clear that it is convenient to use light atoms as probes. The relative number of particles backscattered from a target atom into a given solid angle for a given number of incident particles is related to the differential scattering cross section. The scattering cross section is basically proportional to the square of the atomic number of the target atom. Only a small fraction of the incident particles undergoes a close encounter with an atomic nucleus and are backscattered out of the sample. The vast majority of the incident ions end up implanted in the sample. When probing, particles penetrate to some depth in a dense medium, projectile energy dissipates due to interactions with electrons (electronic stopping) and to glancing collisions with the nuclei of target atoms (nuclear stopping). This means that a particle which backscatters from an element at some depth in a sample will have measurably less energy than a particle which backscatters from the same element on the sample surface. The amount of energy a projectile loses per distance traversed in a sample depends on the projectile, its velocity, the elements in the sample, and the density of the sample material. Typical energy losses for 2 MeV $^{++}$He range between 100 and 800 eV/nm. After passing through a target with a finite thickness the probing ions will not only lose energy, but they will also no longer be monoenergetic. Instead, they will have distribution about the energy which is predicted by energy loss calculations.

2.1.3. RBS-Channeling

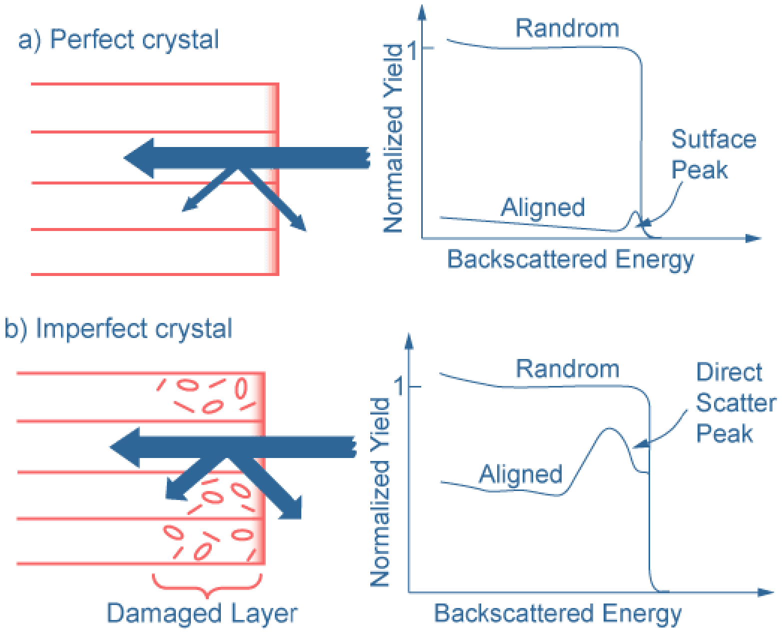

Figure 2.6 Channeling RBS working principle. (a) schematic RBS spectra for a perfect single crystal. In channeling alignment it is observed a strong reduction of the yield. (b)

In addition to elemental compositional information, RBS can also be used to study the structure of single crystal samples. When a particle is channeled, the rows of atoms in the lattice are aligned parallel to the incident ion beam. The bombarding ion will backscatter from the first few monolayers of material at the same rate as a non-aligned sample, giving a "surface peak" in the RBS-Channeling spectra, but backscattering from buried atoms in the lattice will be drastically reduced since these atoms are shielded from the incident ions by the atoms in the surface layers. For example, the back- scattering signal from a single crystal Si sample which is in channeling alignment along the <100> axis will be approximately 3% of the backscattering signal from a non-aligned crystal, or amorphous or poly-crystalline Si. By measuring the reduction in backscattering when a sample is in channeling, it is possible to quantitatively measure and profile the crystal perfection, and to determine crystal orientation. As depicted in Fig. 2.6 (a) for a perfect crystal yield for channeling orientation is much lower than for random orientation. For a not perfect crystal yield is higher than amorphous case but lower than for a perfect crystal. On diced and chemically treated samples C-RBS was carried out with 2.0 MeV $^{4}He^{+}$ and $^{1}H^{+}$ beams in IBM geometry, depicted in Fig 2.7.

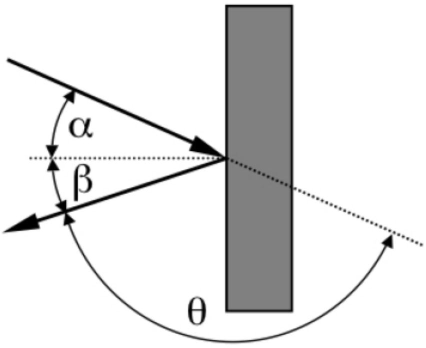

Figure 2.7 scheme of IBM geometry used in C-RBS analysis. α is the incident angle, β the exit angle and θ the scattering angle. In our case θ=160°

As quantifier of the crystalline quality we use the quantity $\chi_{\min}$, defined as the ratio of the RBS yield under channelling alignment and random condition measured at the surface. The higher the degree of crystalline order in the lattice the lower the surface $\chi_{\min}$ due to the reduction of dechanneling from the defects in the crystal. The quality of the surface was correlated with preparation methodology for direct comparison with previously reported results [5.10] and the stringent condition for halo cleaning in hadron machines. The C-RBS spectrum of etched sample in random and aligned condition is reported in Fig. 2.8 for $^4He^+$ (a) and $^1H^+$ (b) beams.

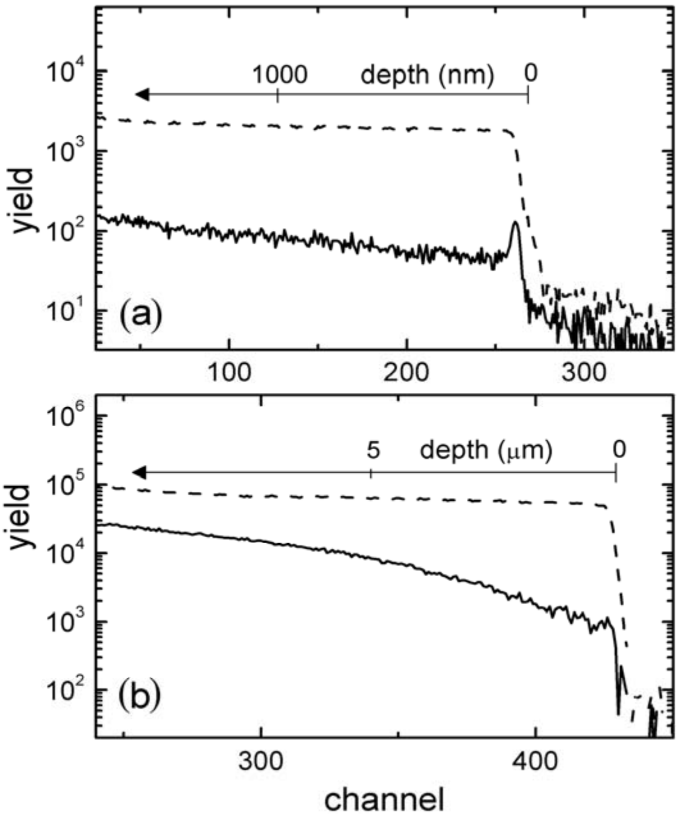

Figure 2.8 C-RBS spectra on silicon crystal oriented along the [110] direction, after chemical etching, using (a) α particles and (b) protons, E_0=2.0 MeV, IBM geometry, scattering angle θ=160°. The dashed spectra refer to random orientation of the crystal. The investigation was carried out down to about 1.5 μm and 10 μm deep into the crystal for α particles and protons, respectively. For both alpha particles and protons the surface $\chi_{\min}$ (2.2% and 2%, respectively) is close to the semiempirical value for a perfect crystal (see Ref. [5.13]).

Analyzed region extends over 1.5 and 10 μm, respectively. The pronounced surface peak in the α particle spectrum is due to the random scattering from the first atomic layers, before that the crystal potential starts to focus the beam at the centre of the channels. The peak is strongly reduced in the spectrum with protons due to the lower energy loss, which in turn leads to a lower depth resolution. The regular shape and the low yield of the c-RBS spectra for both α particles and protons indicate the high quality of the crystalline lattice and the low level of dislocations and defects.

The standard surface roughness, R_a, was measured by means of Atomic Force Microscopy (AFM). Figure 2.9 collects AFM images of the (110) surface just after cut (a), after the chemical etching described in this work (b), and after the etching imparted according to Ref. [5.10](c). The scrapes due to the effect of the blade on silicon surface are normal to the direction of the cut, which are barely visible after etching. Quantitative results are reported in Tab. I.

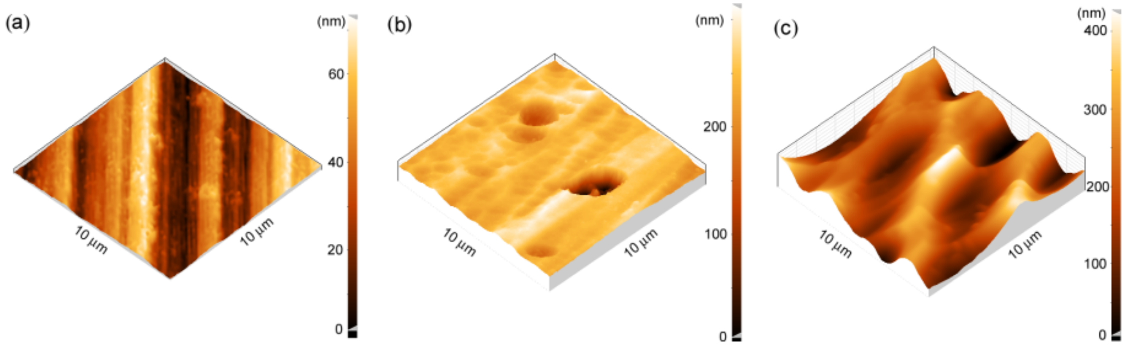

Figure 2.9 AFM pictures of the silicon crystal: (a) just as-cut; (b) after etching according to the procedure here described (c) after chemical etching according to the procedure in Ref. [5.10]. The scrapes due to the blade are visible in the as-cut sample, while they are nearly completely removed after chemical etching. The procedure of etching here described, based on fast and homogeneous oxidation of silicon and subsequent erosion of silicon oxide, allows removal of the surface "dead layer" without formation of undesired craters worsening the surface flatness. R_a is more than 5 times lower with respect to the preparation methodology according to Ref. [5.10].

Table I Standard roughness R_a and surface χ_{min} (using α particles) of silicon crystals just after cut and after chemical etching. R_a is defined as follows: $R_a = \frac{1}{n \times m} \sum_i \sum_j \left| z(i,j) - \bar{z} \right|$ where $z(i,j)$ is a height record of an $n \times m$ image and $\bar{Z}$ is the height average. Results are based on AFM and c-RBS analysis, respectively, and are compared with numerical data from Ref. [5.10].

	R_a (nm)		χ_{min}	
Sample	Ref. [5.10]	This work	Ref. [5.10]	This work
As cut	15±5	15±5	(16±1)%	(16±1)%
Etching	135±10	23±5	(4.1±0.2)%	(2.2±0.2)%

Chemical etching highly removed lattice defects from the surface as highlighted by the surface χ_{min}=2.2% for α particles, which equals the semiempirical values for a perfect silicon crystal along the [110] axial direction (χ_{min}~2%, see Ref.[5.13, 14]]), and improves previously achieved result [5.10] (surface χ_{min}=4.1%). For protons, surface χ_{min} gives about 2% a value in agreement with the semiempirical value also in this case. Table I summarises the results of AFM and c-RBS and gives quantitative comparison with numerical data of Ref. [5.10]. In short, the two main benefits can be envisaged in the chemical etching described in this work: firstly, it improves the effectiveness in removal of the surface damaged layer, providing better crystal quality. Secondly, it yields a very smooth surface (below 25 nm) as compared with previous results, and consistent with the requirement for beam collimation.

2.2. Anisotropic etching

With the aim to realize strip crystals without inducing any lattice damage during their fabrication we developed a fabrication technique based on silicon anistrotropic etching This mode allows to engrave a silicon crystal and, differently from the isotropic etching allows to realize complex structures in silicon, among them also multi-strip crystals, which will be described later.

In contrast to previously used isotropic etchings, there is class of chemical reactions based on alkaline solutions whose erosion rate depends on the crystalline orientation. In particular, planes (110) show the highest etch rate, (111) planes are the most resistant and (100) are in between. Indeed, anisotropic etching is a widely employed technique in modern micro-machining of Si [5.15]. Thus, with proper choice of the components of the solution, anisotropic erosion would results in a high-precision cut of a crystal (see Fig.2.10). A widely used silicon anisotropic etchant is Potassium Hydroxide (KOH). With the identification of H_2O and OH^- as reactant the overall reaction is

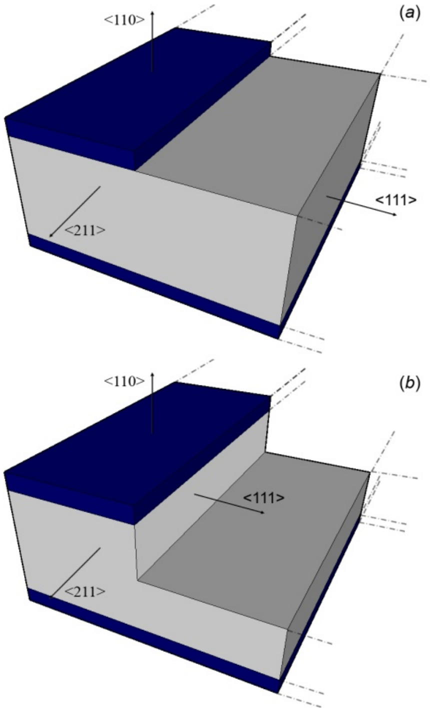

Figure 2.10 Schematic view of fabrication of a silicon crystal via anisotropic etching. (a) sample after patterning with Si_3N_4 (dark regions) and prior to chemical attack; (b) the unmasked areas undergo etching along the <110> direction while negligible erosion occurs along the <111> direction. Proper timing allows one to make controlled indentations or complete cut of the sample

$$Si + 2H_2O + 2OH^- \rightarrow 2H_2 + SiO_2(OH)_2^{2-}$$

Empirically [5.16] it have been found that for KOH solutions with concentrations in the range 10-60% the silicon etch rate is given by the relation

$$R = k_0[H_2O]^4[KOH]^{1/4}e^{-E_a/KT} \qquad (2.2)$$

Where k_0=4500 µm/h*(mol/L)$^{-4.25}$, E_a=0.60 eV for (110) planes, k_0=2480 µm/h*(mol/L)$^{-4.25}$ and E_a=0.595 eV for (100) planes. Table II summarizes etch rate for different planes of Silicon.

Table II Etch rate for different silicon planes in 30% KOH at 70°C. (110) planes are etching much faster (111) planes.

Crystallographic orientation	Etch rate (µm/min)
(100)	0.797
(110)	1.455
(211)	1.319
(221)	0.714
(311)	1.436
(331)	1.160
(111)	0.005

Exploiting anisotropic behavior of silicon in KOH solutions Si crystals were prepared. Starting material are 4-inches (110) Si wafers with the wafer's flat oriented perpendicular to <111> direction. A 100 nm layer of Si_3N_4 was deposited onto all faces of the wafer through low-pressure chemical vapor deposition and patterned with standard photolithographic techniques [5.17] with the masking pattern aligned with the wafer's flat. The wafer was immersed in KOH solution (40% weight concentration) with the Si_3N_4 pattern as a masking layer [5.18] and kept at 70°C until the holes where completed, which resulted in erosion of uncovered regions on the wafer.

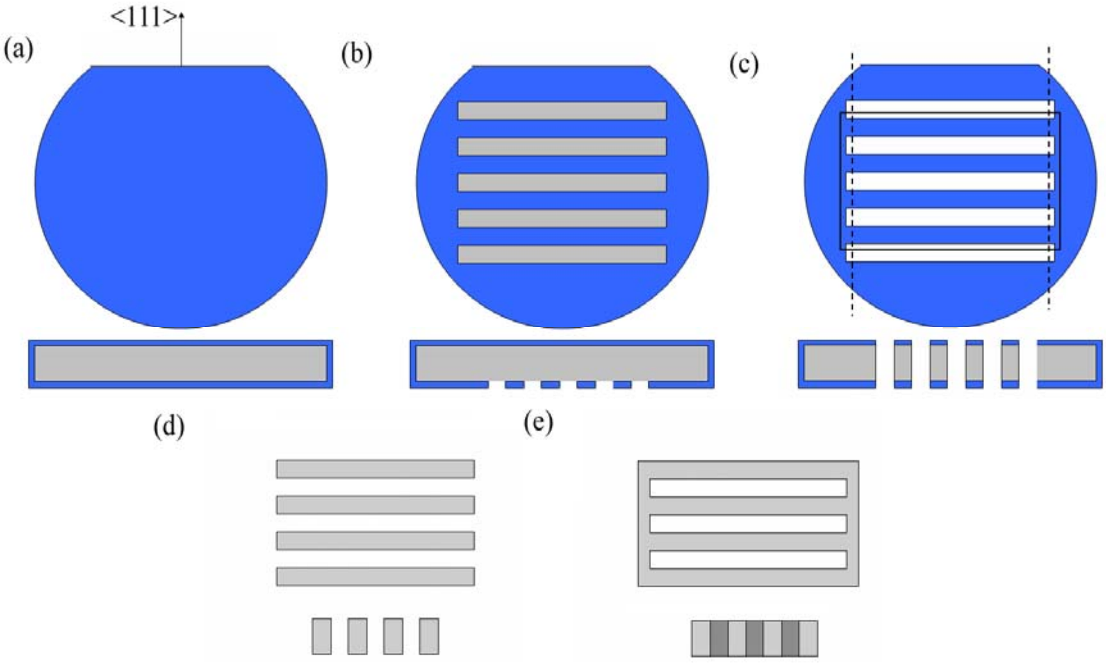

Figure 2.11 Fabrication of crystals for channeling (not to a scale) (*a*) deposition of a uniform 100-nm thick Si_3N_4 layer, (*b*) pattering of Si_3N_4, (*c*) anisotropic KOH etching and mechanical dicing along either the dashed line to release a series of independent strip-like crystals or the solid line to manufacture a multi-strip crystal with a frame, (*d*, *e*) final removal of the Si_3N_4 film. Masking by KOH resistant Si_3N_4 thin film patterned onto the surfaces of the Si crystal allows fabrication of rather complex geometries.

For the experimental parameters of the solution we chose, the etch rate of (111) planes is negligible with respect to the (110) planes so that chemical erosion proceeds as depicted in

Fig. 2.10b. The protecting layer of Si_3N_4 is finally removed from lateral surfaces using HF 49%, leaving a wafer with regularly equi-shaped rectangular slots.

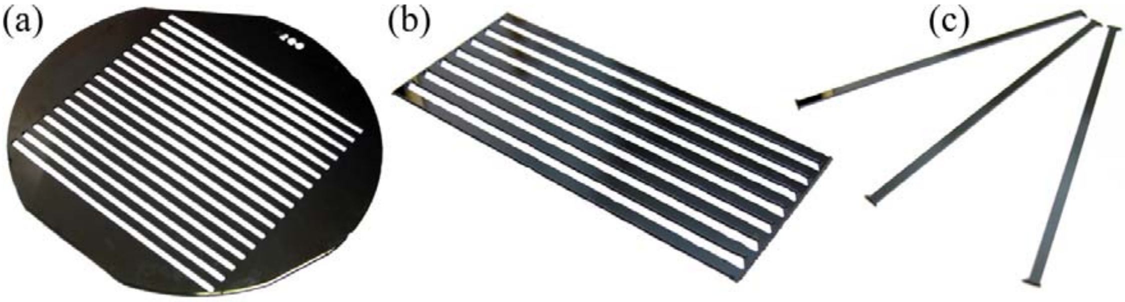

Figure 2.12 From left to right: a 4'' silicon wafer with full passing holes realized by anisotropic etching. A silicon multistrip and silicon strips obtained by mechanical dicing of the wafer

Then, the wafer can be cut in such a way to achieve either a batch of independent strips (Fig.2.12c) or a rigid frame interconnecting a series of regularly positioned strips (Fig.2.12b). In the case of strip-shaped crystals, they were sized as $(0.5\text{-}2)\times(0.3\text{-}0.5)\times 70$ mm^3 because these dimensions best matched the requirements for application in the CERN SPS external lines H8 and H4, the first operating with 400 GeV protons, the second with 120-150 GeV negative particles. The other geometry was studied to excite multiple volume reflection as a result of deflection of the particles with each strip [5.19]. Spacing and thickness of multi-strip crystals varies in the range 0.5 to 2 mm. More generally, the pattern of the photolithographic mask enables the achievement of a strip with any size of more complex structures that can be achieved by dicing the wafer parallel or perpendicularly to the lattice directions. Morphological investigation of the roughness of the crystal surface was done by atomic-force microscopy (AFM). Analysis was carried out over one of the (110) surfaces of the samples, i.e., to the lateral surface of the crystal, which are the planes first interacting with halo-beam

particles. Clear evidence of ultra-flat surface with a roughness down to the monolayer level was achieved over a relatively wide scan (10×10 μm^2). Standard roughness is a quantifier of the flatness of a surface, which is defined as $R_a = \frac{1}{n \times m}\sum_i^n \sum_j^m \left|z(i,j) - \bar{z}\right|$, where $z(i,j)$ is the height record of an $n\times m$ image and $\bar{z}$ is the height average. Standard roughness featured R_a=0.25 nm, i.e., R_a was decreased by nearly two orders of magnitude with respect to preparation by mechanical dicing assisted by isotropic chemical etch.

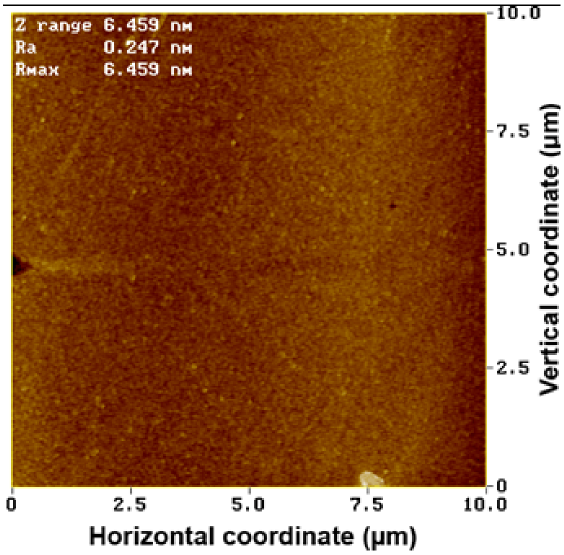

Figure 2.13 AFM image taken over a 10×10 μm^2 area on the lateral surface of the crystal. Standard roughness keeps down to the sub-nanometric level for the sample under study.

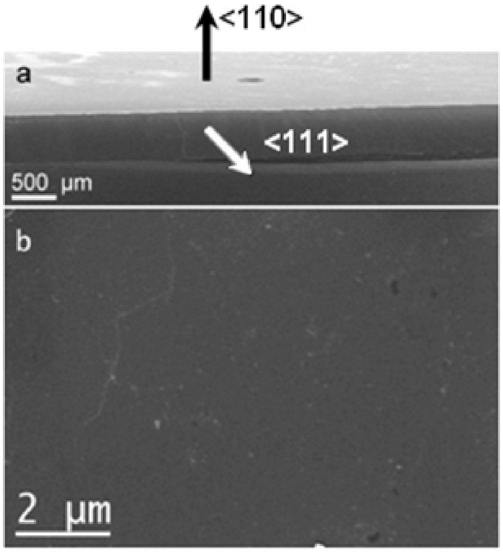

Figure 2.14 SEM images of the crystal, a) tilted view of the flat crystal upper surface and of the smooth <111>-oriented entry face, which is marked by an arrow. b) magnified view at normal incidence of the <111> entry face, showing very uniform morphology.

The sample was analyzed by scanning and transmission electron microscopy (SEM and TEM). Fig 2.14*a* shows a panoramic view of the sample. The SEM image highlights the homogeneity of the upper (110) surface of the sample and the uniformity of the (111)-oriented side face. This latter features some vertical steps, due some alignment mismatch between the mask and the <111> direction. At higher magnification, the SEM image of Fig. 2.14b shows that the surface of the entry face is very smooth and homogeneous.

For TEM characterization of the entry surface of the crystal and the sub-surface region, a cross-section specimen was prepared through a conventional process of mechanical polishing and ion milling. The TEM bright-field image shown in Fig. 2.15*a* highlights a straight termination of the crystal surface, and the contrast variations indicate that the preparation resulted in a smooth edge-shaped sample with no evidence of mechanical damage introduced by the thinning procedure. No lattice defect was observed in the sub-surface region of the sample. Indeed, the ripples in the bright-dark contrast fringes of the TEM bright-field image arise from a gradual increase of the projected thickness of the wedge-thinned specimen. Presence of extended defects in the Si lattice, such as dislocations, is ruled out. Such defects would have introduced local distortions in atomic positions and therefore the variation of intensity for the diffracted electron beam would have resulted in abrupt variation of the image contrast. The observation at high resolution (see Fig. 2.15*b*) shows an ordered arrangement of atomic columns, which is preserved up to the crystal surface, i.e., the crystal is terminated with atomically sharp ordering. The electron diffraction pattern of Fig. 2.15*c* confirms that the exit direction of the beam is parallel to the <111> crystal direction. Similar observations over different area of the sample confirmed previous determinations.

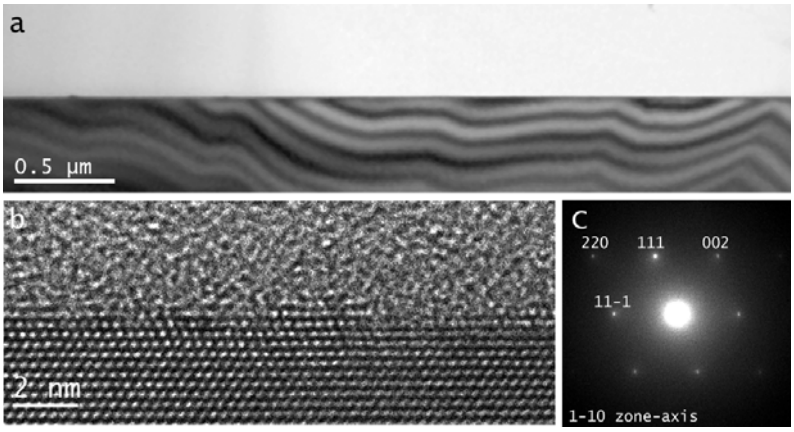

Figure 2.15 TEM characterization of the entry face of the crystal. *a*) low-magnification panoramic view of the entry face as visible in the cross-sectioned specimen. The white-black contrast fringes are due to smooth variation of sample thickness. *b*) High-resolution image of the ordered and atomically sharp termination of the crystal surface. The amorphous material above the crystal is the embedding epoxy used in the preparation of the cross-section sample. *c*) Electron diffraction pattern of the sample, indicating that the surface is parallel to the <110> direction.

2.3. Crystal bending

Elastic strips or tapes (wires) are commonly used in industrial applications. When such strips are bent, the longitudinal strains, which are purposely induced, are accompanied by lateral strains in the width direction of the strip. As a result, the strip takes the shape of a saddle, i.e., it bends to a surface in which the two principal curvatures are opposite in sign. This effect is referred to as anticlastic deformation (AD). For an amorphous material, if the longitudinal radius of curvature, i.e., the primary radius of curvature, R, into which the strip is being bent is large, the cross section is found to deform to an arc of a circle with secondary radius $R_A = R/v$, where v is Poisson's ratio [5.20]. Thus, although the extent of AD is not large, it may cause practical difficulties. As an example, the edges of the magnetic tapes used in computer applications are found to wear because of it. Similar difficulties are encountered in the bending of the long metallic plates used to form the adjustable working sections of wind tunnels. The consequent AD of the plates is found to interfere with the air flow. Although possible remedies to counteract anticlastic deformation do exist, e.g. by proper tapering of the edges on the concave sides of the tapes or plates, there are applications in which AD is desirable. A significant example is particle-beam steering through channeling in a crystal. As one might expect, AD of an anisotropic material, as needed for channeling experiments, would lead to significant dependence of the curvature ratio R/R_A on the chosen crystallographic direction.

2.3.1. Anticlastic deformation in an anisotropic material

We herewith review some concepts of anticlastic deformation in a isotropic material that are necessary for understanding further modelling. A typical strip crystals is 70x2x0.5 mm^3 wide (see Fig. 2.16). Thereby, the shape of the crystal is such that the theory of a mechanical beam can be worked out extensively.

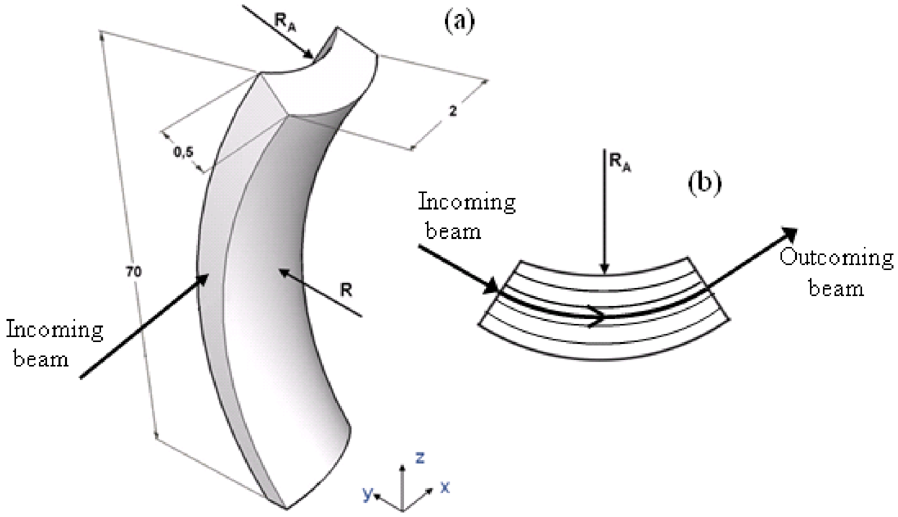

Figure 2.16a Sketch of a bent silicon strip for channeling experiments. Anticlastic deformation with radius R_A arises as a result of primary bending with radius R. Quotes are expressed in mm and represent typical values for high-energy experiments. (b) Cross-section of the crystal; the incoming particles are captured by the potential of atomic planes and the beam is being deflected.

Crystalline silicon exhibits FCC cubic symmetry and diamond lattice with each atom on the centre of a tetrahedron with four nearest-neighbour atoms at the four vertexes. Thereby, Young's modulus and Poisson's ratio are direction dependent [5.21]. As for any FCC symmetry, the elastic properties are completely characterized by only 3 independent constants. For Si, the compliance matrix, ***S***, referred to the canonical base **<e>** = {<100>, <010>, <001>}, (where <100>, <010>, <001> are main crystalline axes of the cubic cell), takes the form:

$$\boldsymbol{S}^{<e>} = \begin{pmatrix} 7.678 & -2.144 & -2.144 & 0 & 0 & 0 \\ & 7.678 & -2.144 & 0 & 0 & 0 \\ & & 7.678 & 0 & 0 & 0 \\ & & & 12.531 & 0 & 0 \\ & Sym & & & 12.531 & 0 \\ & & & & & 12.531 \end{pmatrix} \mathrm{x}10^{-3} MPa \qquad (2.3)$$

In channelling experiments, the crystal is bent to a relatively modest curvature and the primary deformation is imparted at the edges of the strip through a mechanical couple of moment ***M*** by clamping onto a rigid holder which will be described later. Such a system can be modelled as a homogeneous and anisotropic bar under infinitesimal deformations and small displacement, supported at its ends by kinematics and concentrated supports and bent by a point-like couple of forces at its edges, as shown in Fig. 2.17.

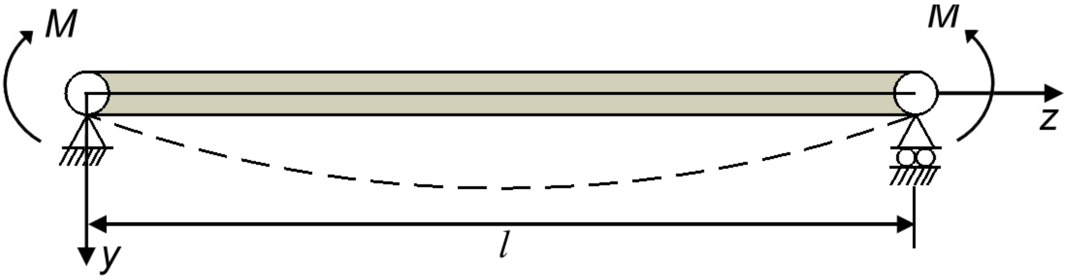

Figure 2.17a Schematic representation of bending of a beam of length *l* under the action of a couple of moments applied at its ends.

The displacement of the strip along *y* direction is given by [5.22]

$$v(x,y,z)=\frac{1}{2\,a_{33}R}\left(-a_{13}x^2+a_{23}y^2+a_{33}(lz-z^2)-a_{35}xz\right) \tag{2.4}$$

where a_{ij} are the 6x6 coefficients of $\mathbf{S}^{<e>}$. Presence of the z^2 term is related to the imposed principal bending while the x^2 term shows that *x-y* cross section is deformed as a parabola, giving rise to anticlastic bending, whose magnitude is linearly proportional to the imposed bending. The mostly direct observable physical quantity is the principal curvature while anticlastic deformation is quantified by the secondary curvature. Thus, the ratio R_A/R determines the extent of anticlastic deformation in dimensionless units. Differently from the case of an isotropic material, the ratio between anticlastic and principal bendings is determined by the two components of the elastic compliance tensor. For our applications, the region of interest is the central part of the crystal so that R_A/R is calculated at x=0, y=0, $z=l/2$:

$$\frac{R_A}{R}=-\frac{a_{33}}{a_{13}} \tag{2.5}$$

It should be remarked that a_{33} cannot vanish; thereby it is impossible to find a bent silicon crystal without anticlastic deformation. Moreover, R and R_A have opposite signs, i.e., the crystal takes the shape of a saddle. It should be remarked that Eq. (3) holds for crystals narrow enough in the width direction such to develop a plain stress regime. In fact, by increasing the crystal width, b, the system tends to behave like a plate under plain strain condition, thus preventing anticlastic deformation [5.23]. As reported in [5.23-25], an estimator of this behaviour is the “Searle parameter”,

$$\beta=\frac{b^2}{Rt} \tag{2.6}$$

where t is crystal thickness. If $\beta<1$, anticlastic bending arises on the whole crystal width (beam-like behaviour). Conversely, if $\beta>>1$, anticlastic bending is remains only in the external regions of the crystal (plate like behaviour). As will be demonstrated in the following, we will always deal with the case $\beta<<1$. The ratio in Eq. (2.5) is orientation dependent so that designing a bent crystal for channeling and volume reflection experiments demands its knowledge for any orientation of the strip. For planar channeling and volume reflection, the (110) planes were found to be best efficient, namely the crystal is to be oriented with such axis along y axis in Fig. 2.17. The remaining two directions are to be chosen and R/R_A should be studied as a function of the base, **<m>**, with the vectors parallel to the sides of the crystal.

Thereby, the compliance tensor in the base **<m>** is linked to $\mathbf{S}^{<e>}$ through a similarity transformation:

$$\boldsymbol{S}^{<m>} = \boldsymbol{K}\boldsymbol{S}^{<e>}\boldsymbol{K}^{T} \tag{2.7}$$

K being the rotation matrix connecting the **<e>** base to the **<m>** base.

2.3.2. Simulation and experimental

In order to study the orientation dependence of strained silicon strips, several crystals of size 2x0.5x70 mm^3 were diced from a 0.5 mm thick (110) silicon wafer, and the induced lattice damage was removed by isotropic etching previously described. The wafer's "flat", i.e., the cut done by the manufacturer for better usage of the wafer was parallel to the $(1\bar{1}0)$ plane. The crystals were cut at some inclination, θ, with respect to the flat (see Fig.3 and Tab. I) and all of them were oriented with the <110> direction along y axis. The ratio R_A/R was studied by bending the crystal through the holder typically used in channeling experiments and which will be described later.

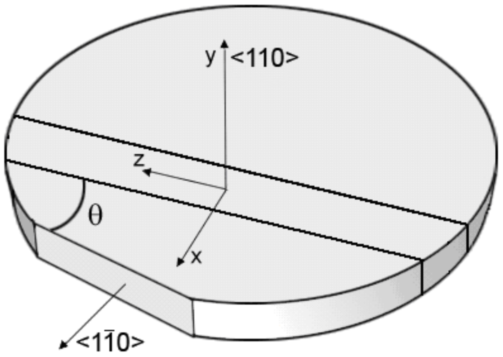

Figure 2.18 Silicon crystals are diced from a (110) wafer. The length of 70 mm is achieved at several angles θ with respect to the wafer's flat. The Y axis is always the <110> direction, while x and z vary as function of θ

Table III Ratio between anticlastic and principal bending radii as a function of *θ*: comparison between theoretical model, measurements and FEM simulations.

θ(deg)	R_A/R (measured)	R_A/R (theoretical)	R_A/R (FEM)
0	-3.52	-3.59	-3.58
15	-3.98	-4.00	-4.00
35.26	-6.31	-6.20	-6.15
45	-6.82	-6.80	-6.73
60	-4.72	-4.70	-4.67
75	-3.16	-3.15	-3.14
90	-2.75	-2.76	-2.75

The principal and anticlastic radii were measured by means of a white-light profilometer (Veeco NT1100) capable of recording the profiles of the bent crystal with height resolution of 3 nm. In order to make the surface orientation independent of the alignment with respect to the profilometer objective, tilt and piston terms were removed via software.

Fig. 2.19 shows a typical profile of the strip taken in a central region 2x2 mm^2 wide, which exhibits a saddle-like surface as predicted by elasticity theory.

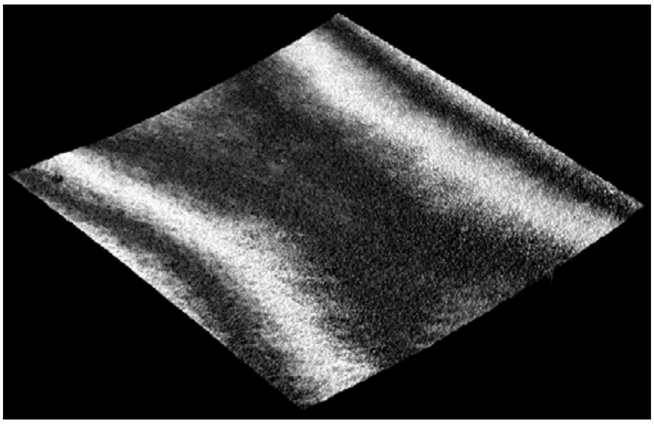

Figure 2.19 Deformation of the crystal surface when bent by the holder. The crystal is diced at *θ*=35.26°. A saddle deformation is visible thanks to interference fringes.

Fig. 2.20 illustrates the experimentally recorded levels of R_A/R for the values of θ in Tab. I. Clear signature of orientation dependence is observed with the ratio R_A/R attaining its maximum for the direction <1/√2 1/√2 1> and its minimum for the direction <100>. Such trend reflects the behaviour of Poisson coefficient for a (110) plane [5.21]. Moreover, it should be noted that the crystalline orientation θ = 35.26° corresponds to a crystal with the <111> axis along the beam direction, i.e., the most favourable condition to study axial channeling.

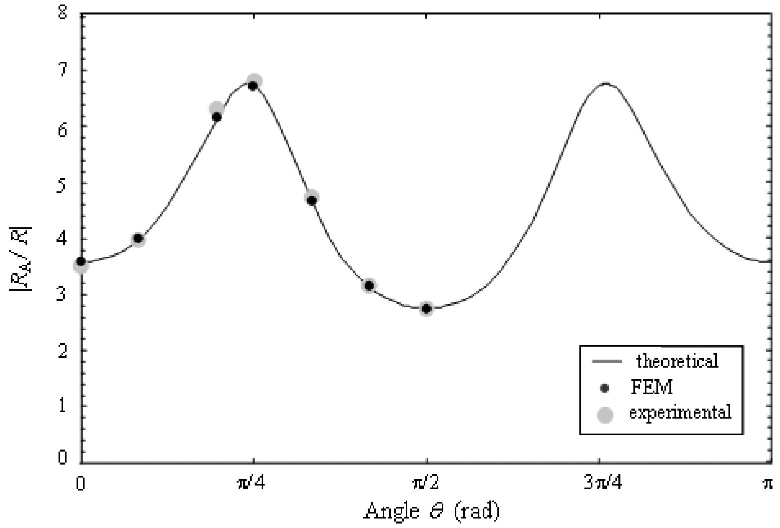

Figure 2.20 Ratio $|R_A/R|$ as function of θ (for its definition see Fig. 2.18). Experimental data are compared with FEM simulation and with the model. The figure shows that the ratio |RA/R| is direction dependent as expected from a crystal.

The expected ratio of $|R_A/R|$ versus the angle θ, reported in Fig. 2.20, has been obtained analytically by calculating the ratio $|a_{33}/a_{13}|$, which is the Poisson ratio for the corresponding crystalline direction, according to classical mechanical beam theory. Fig. 2.20 also includes experimental results for the ratio $|R_A/R|$, which are in good agreement to theoretical values for each crystalline direction.

It should be remarked that Eq. (2.4) holds true for the ideal case of concentrated supports at the edges of the strip but, in practice, clamping of the crystal mounted on the holder occurs over a finite region. Thereby, distortion of the shape of the bent crystal from a saddle is expected, particularly in proximity of the holder jaws. To our knowledge, an analytical formulation including a non point-like constrain does not exist in literature. With the purpose to take into account information about the portion of crystal not influenced by the presence of holder jaws, Finite Element Method (FEM) simulations based on STRAUS7 software (release 2.3.3) have been worked out considering the geometry of the holder used in this work (see Fig. 4), which is routinely used in channeling experiment. Furthermore, according to the works in Ref. [5.24, 25] aimed to a more homogeneous bending, we also considered the possibility to realize new clamping conditions to hold the crystal. A sketch of the FEM mesh is given in Fig. 2.20. Since the deformation of the crystal is expected to be not appreciably affected by the whole holder structure, only the jaws of the holder have been modelled in our numerical simulation. The silicon crystal was modelled as 3D anisotropic cubic bricks elements, whereas the aluminium supports of the holder were modelled as isotropic 3D elements.

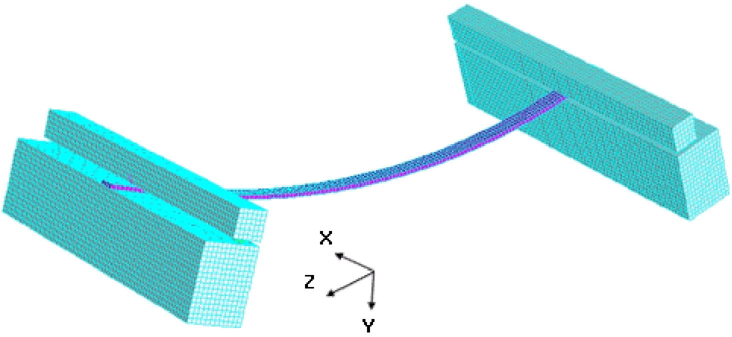

Figure 2.21 Mesh of a Si strip mounted on the holder jaws for FEM. The strip (2x0.5x70 mm3) is simulated by 528-brick elements, whereas 36496 bricks elements model the holder supports.

Both the strip and the holder were considered homogeneous elastic bodies under small strains. The strip was assumed to be perfectly bonded to the holder supports. Bending of the silicon strip is achieved by imposing rotations of both the lower aluminium jaws along the *x* axis, obtaining a symmetric flexure of the crystal in the *yz* plane. Fig. 2.22a shows the dependence of $|R_A/R|$ as a function of coordinate *z* for the first half of the strip bent at $R = 1.5$ m for some crystalline orientations.

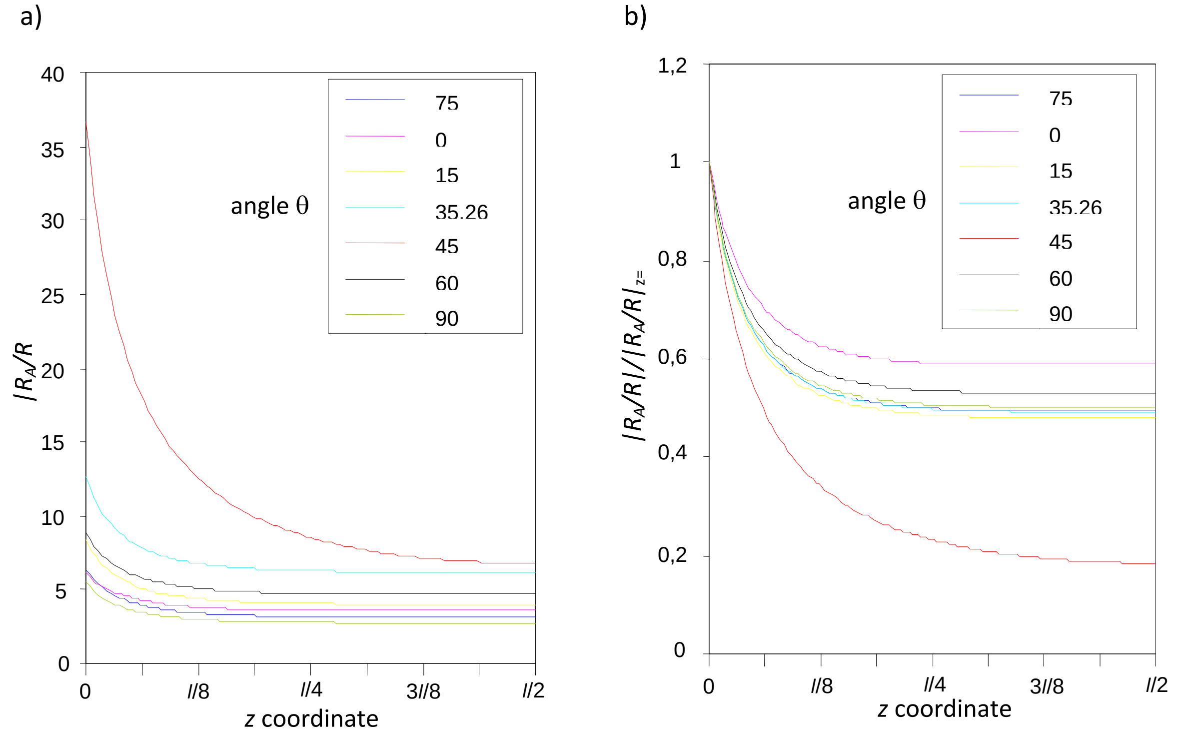

Figure 2.22 FEM-simulated values of $|R_A/R|$ along the length of a (2x0.5x70 mm^3) bent crystal for some crystalline orientations and $R = 1.5$ m The numerical values agree with the theoretical prediction based on Eq.(3) except for a small region of the crystals close to the holder jaws.

The same results are shown in Fig. 22b expressed as normalized ratio at the beginning of the strip, i.e., $|R_A/R|/|R_A/R|_{z=0}$. It should be noted that, the Searle parameter is equal to 6.67 $\cdot 10^{-4}$ for the crystals under study, i.e., the beam-like regime is fully satisfied. In fact, for most of the crystals, experimental and numerically simulated $|R_A/R|$ largely agrees with the beam theory as shown in Fig. 2.19. The ratio $|R_A/R|$ is distorted only in proximity of the jaws within an extension estimated to be about *l*/8 on each side for all the crystalline orientations, except for $\theta = 45°$, as showed in Figure 22b. In the latter case, the maximum of the ratio $|R_A/R|$ is attained, thus stronger deformation takes more space to be damped [17]. This achievement is consistent with the experimentally gained criterion for which the central third of the crystal can safely be used for channeling experiments. FEM analysis has shown that this is in fact a prudent criterion.

The size of the crystals considered above is currently under use for channelling experiments at CERN with protons at 400 and 120 GeV energy. However, in sight of exploitation of channelling for halo collimation in future experiment in the Large Hadron Collider (LHC) with an intense proton beam 7-TeV in energy, longer crystals are demanded for this application. As claimed in Ref.[5.26] as long a crystal as 10 mm along the beam is optimal for 0.2 mrad bending. Thereby, numerical simulations have been extended to bent a 10x0.5x70 mm^3 crystal. In this case, we conservatively simulated the case of large bending ($R = 1.5$ m) for channelling applications for which, beam-like regime takes place, the Searle parameter being $1.67x10^{-3}$. Figs.23a,b show the ratio $|R_A/R|$ along the length of the bent crystals are similar to those obtained for the 2 mm width strip.

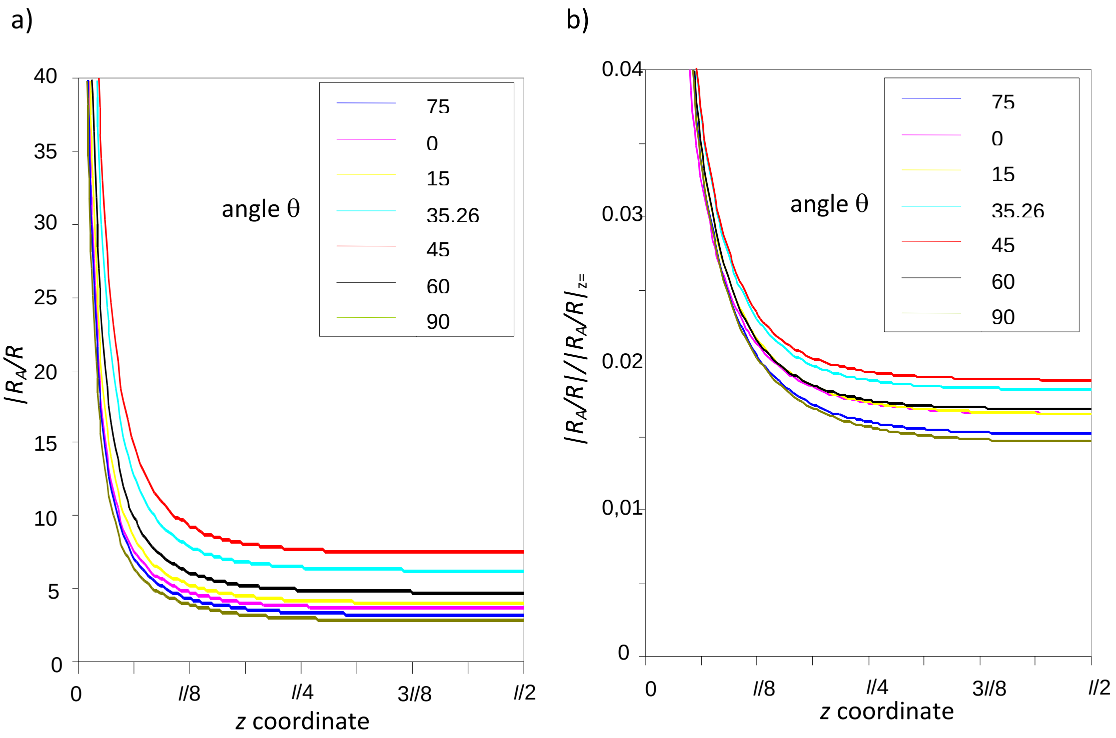

Figure 2.23 FEM-simulated values of $|R_A/R|$ along the length of a (10x0.5x70 mm^2) bent crystal for some crystalline orientations and $R = 1.5$ m. The numerical values at the middle of the crystals slightly differ with respect the theoretical prediction.

As expected, in proximity of the holder jaws, $|R_A/R|$ is larger than for the 2-mm crystals. Conversely, in the middle of the 10 mm width strips, $|R_A/R|$ is slightly smaller than for the 2-mm crystals. From the figures it comes clear a weak dependence of $|R_A/R|$ on crystal orientation, i.e., for sufficiently large bent crystals, the region affected by the constraints is almost invariant with the crystalline orientation. The inversion in the trend of $|R_A/R|$ along z coordinate calls forward an effect of anisotropy of silicon that was neglected for the shorter crystal. Based on Eq.(2), the term a_{35} couples x and z coordinates, giving rise to an anisotropy-driven torsion effect. Such torsion is negligible in proximity of the jaws because of the constraints, while it attains its maximum across the central part of the crystal. Numerical results confirm the unimportance of this effect for the 2 mm width crystals though it starts playing a role for the wider crystal at the position where it is most effective, thus decreasing the ratio $|R_A/R|$ on the central part of the crystal.

In order to assess the effect induced by different geometries of the holder jaws, numerical simulations of a mechanical holder with circular aluminium jaws 3.00 mm in diameter have been performed and the results shown in Figs 24 and 25, for a crystal width of 2 and 10 mm, respectively.

On can see that the distortion effects due to circular jaws are restricted almost to the first eighth of the crystal length and rapidly vanish going toward the middle of the strip for all the crystalline orientations considered here. This effect can be mostly appreciated for the narrower crystal (Fig. 2.24) because it leads to a constant ratio nearly all over the crystal. However, it holds true also for the wider crystal (Fig. 2.25) though the ratio starts gradually increasing on the strength of the above-mentioned anisotropy-driven torsion. In any case the effect of circular jaws leads to performance improvement.

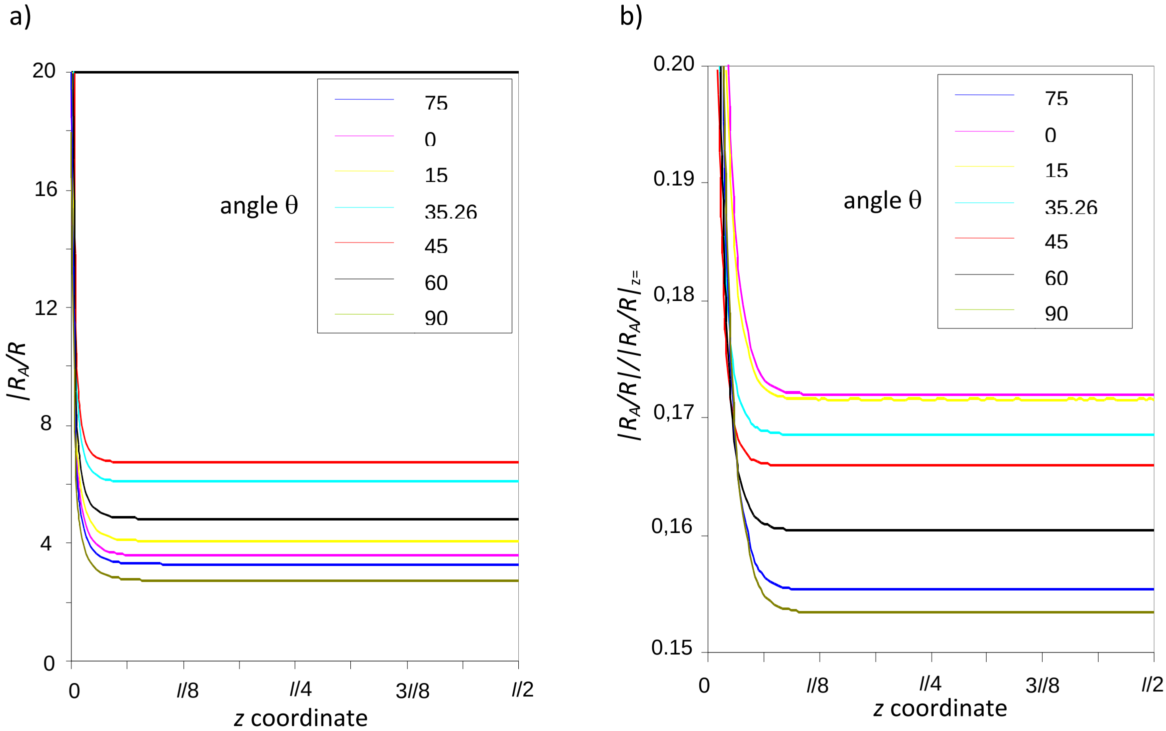

Figure 2.24 FEM-simulated values of $|R_A/R|$ along the length of a (2x0.5x70 mm^3) bent crystal for some crystalline orientations and R=1.5 m. Circular jaws having a diameter of 3 mm have been simulated.

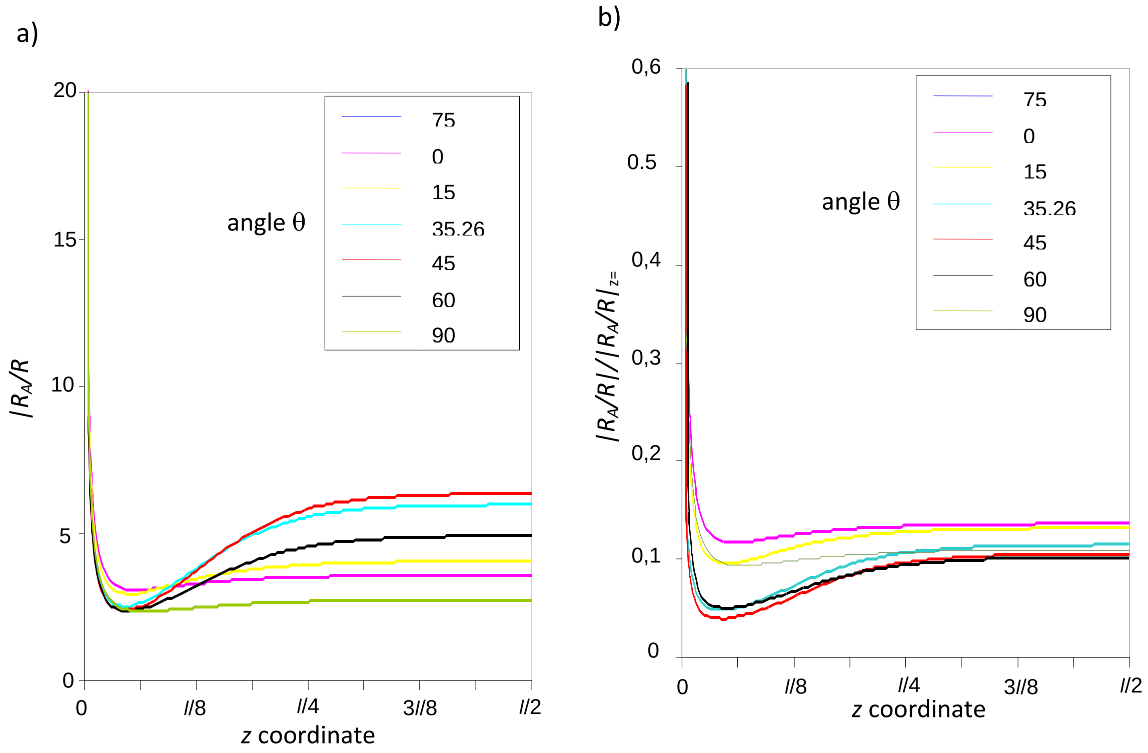

Figure 2.25 : FEM-simulated values of $|R_A/R|$ along the length of a (10x0.5x70 mm^3) bent crystal for some crystalline orientations and R=1.5m. Circular jaws having a diameter of 3 mm have been simulated.

2.3.3. Holders for strips and multi-strips crystals.

In order to impart to the crystal the desiderated bending and to keep it in position with respect to the beam special holders have been designed. Two different kind of holders were realized to bend single strip crystals or multi-strip crystals. The holders to bend single strip crystals were initially designed in collaboration with the Russian Institute for High Energy Physics IHEP and is based on deformation control technology. Since 2007 holders for strips and multi-strip have been designed in mechanical workshop of physics department and INFN of Ferrara University.

Figure 2.26 (a) holder of a single strip crystal. Acting on the bolts highlighted with a red circle the holder is mechianically deformed, acting on the screw highlighted with a green circle it is adjusted torsion. (b) a strip crystal mounted on the holder.

Acting on the bolts highlighted in red in the Fig 2.26a the holder is mechanically deformed allowing adjustment of the relative distance of the surfaces over which crystal lean on. Adjusting the distance between such surfaces it is possible to adjust the main crystal bending radius, and keeping in mind the ratio between anticlastic and main bending radius it is possible to obtain the wanted deflection angle.

Such scheme provides flexibility for bending though, on the other hand, mechanical strain due to holder deformation propagates through the holder and alters planarity and parallelism of surfaces where crystal lean on inducing torsion of the crystal. In order to correct for torsional effects a screw (highlighted in green) is used. Such screw based torsion compensation system demonstrated to be very effective, allowing to obtain torsions of less than 1μrad/mm.

Non flatness of surfaces where the crystal lean on is not important for the single-strip crystal, but is crucial for a good reciprocal alignment of the strips in a multi-crystal. In order to minimize the deformations induced on such surfaces by the mechanical deformations imparted to the holder we developed a new holder kind. Differently from the previous, the new one is a rigid holder, which does not allows the possibility to adjust bending radius, but provides a good flatness and parallelism of the surfaces where the crystal lean on.

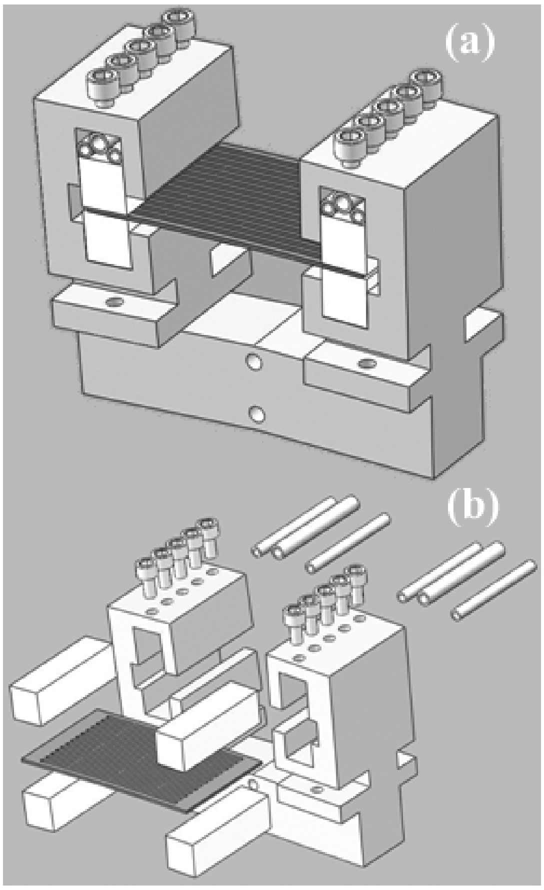

Figure 2.27 (a) schematic view of a multi-strip crystal assembled on its holder (b) an exploded view of the holder and crystal assembly.

Fig. 2.78a is a schematic of the holder realized for multi-crystals, whose details can be appreciated in the exploded view of Fig. 2.27b. A rigid frame of two unparallel cavities serves to host the edges of the multi-crystal with the components to fasten it to the holder itself. The cavities are reciprocally inclined in order to impart to the crystal the wanted curvature. The holder was electro-eroded from a mono-block of ergal which was selected because of its good elastic properties and the possibility to be used under vacuum environment. Electro-erosion guaranteed very precise sizing, low roughness and high planarity of the surfaces.

Two stainless 9×9×30 mm^3 parallelepiped at each of the crystal edges were used to clamp the crystal. Steel was used because it can be worked mechanically with high accuracy and importantly it offers a relatively high Young modulus. Glass might be an alternative material that can be finished with superior planarity though its lower Young modulus caused it to deform under the action of the screws.

The surfaces in contact to the crystal (9×30 mm^2) were manufactured with very high planarity over the whole surface. White-light optical profilometry was performed to measure the planarity through a VEECO™ NT1100 instrument, equipped with a stitching system. Data acquisition is taken over a region of interest (ROI) then scanning is continued on a neighbouring ROI partly overlapped with the previous one. The software is capable of proper interpretation of the region of overlap, resulting in scanning over as wide an area as 10×10 cm^2. A profile of one of the surfaces in contact with the crystal is shown in Fig. 2.28. Hereinafter, the peak-to-valley difference is assumed as a measure of planarity. A vary flat surface was observed over most of the surface with some degradation in proximity of the edges. Planarity was measured to be 150 nm excluding the 1 mm edge of the block.

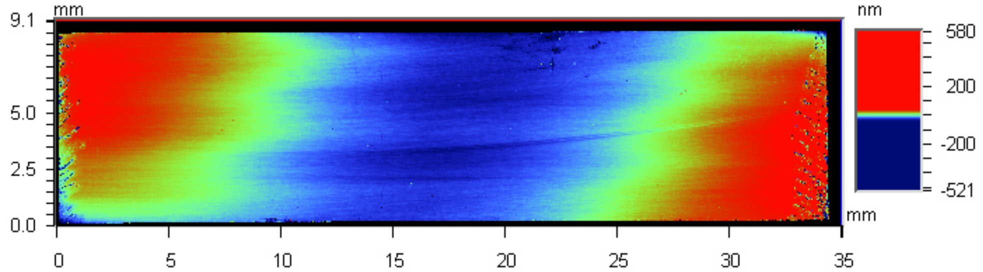

Figure 2.28 Interferometric characterization of the surface of a steel block used in the clamping of a multi-strip crystal. Excluding the 2mm edge planarity is 150 nm

Final clamping was achieved thanks to an array of five low-thread screws at each of the crystal edges. The localized deformation field induced by the screws as applied directly onto the parallelepipeds was found to alter the parallelism of the strips, thereby a damping system of three pipes at each side softened the deformation. The pipes were made of harmonic steel. Another critical point was the thickness of the parallelepipeds in the direction perpendicular to the crystal. In fact, such dimension was empirically chosen to be sufficiently thick as to make the total misalignment of the strip to be sufficiently mild. Finally, the wafer from which the crystal was fabricated should exhibit a planarity comparable to that of the parallelepiped onto which the crystal is laid. We used 1.5 µm planarity 4'' silicon wafers as a starting material, which was brought to 300 nm planarity over areas of 9x27mm^2 by means of polishing operations.

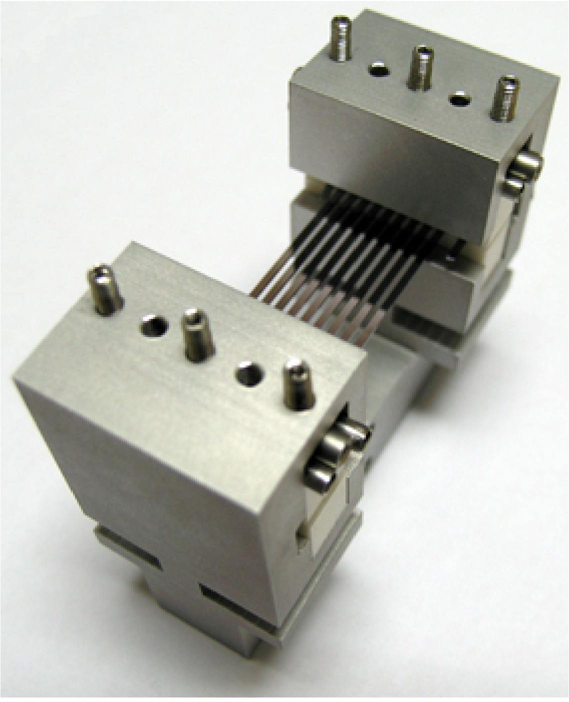

Figure 2. 29 A multi-strip crystal mounted in the holder.

The multi-crystal was inserted and fastened into the holder for bending (See Fig. 2.29). Optical profilometry was carried out on the central part of the crystal, i.e., on the portion of the crystal that is supposed to interact with the particle beam and to provoke VR at each strip. Fig. 2.30 shows the deformation profile of the array of strips. Coordinate z in the figure is along the direction orthogonal to the crystal.

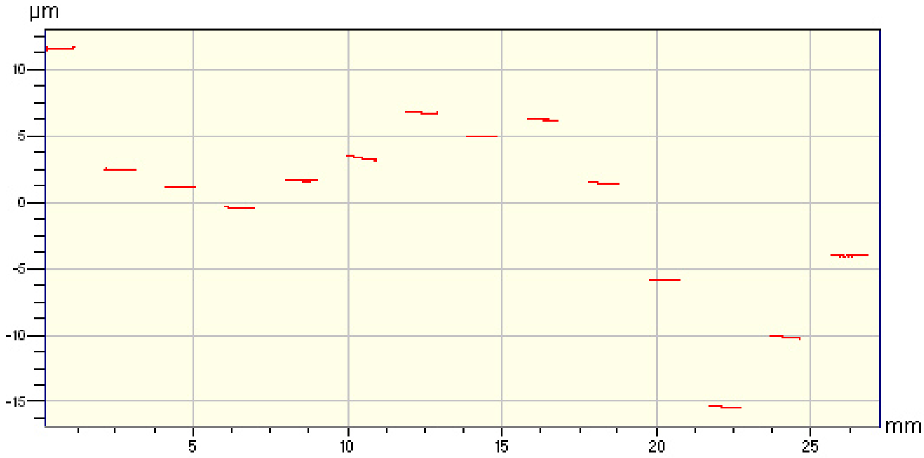

Figure 2.30 Fig XX: interferometric measurement of a multi-crystal. Each segment represents a strip. All the crystals are aligned within 120 µrad.

Analysis yields an average deflection angle α = (220±10) µrad. A quantifier of the quality of a multi-crystal for efficient steering of a particle beam is the dispersion in the alignment of the crystals, β. For an efficient deflector, the alignment dispersion should be less (possibly much less) than the acceptance of the crystal, α, thus leaving a wide angular region where channelling plays no role and in which MVR only steers the beam. In our case, it held an r.m.s. value of $\beta = 70 < \alpha = 220$ µrad.

2.4. A crystals for low energy negative particles channeling

As will be shown later, operation with high-energy negatively charged particles was succefully accomplished. Due to the wealth of accelerator machines operating at moderately low energy, we designed a crystal for operation in this regime, which exploit the quasi-mosaic curvature. Dechanneling length of negative particles is about 10 times shorter than for positive counterparts. Manipulation of low energy (for example 1 GeV) particles by means of channeling requires the use of very short crystals, with thickness of some tens of microns. Thin quasi mosaic crystals are the ideal solution for this purpose.

As a plate of anisotropic material is bent by a point-like mechanical couple of strength M_1 at the edges, as depicted in Fig. 2.31(a), a deformation field (u,v,w) along the (x,y,z) directions, respectively, holds [5.22] under the hypothesis of small deformations:

$$
\begin{aligned}
u &= \frac{M_1}{2I_1}\left(2a_{13}xy + a_{36}y^2 + a_{35}yz\right) \\
v &= \frac{M_1}{2I_1}\left(-a_{13}x^2 + a_{23}y^2 + a_{33}(Lz - z^2) - a_{35}y\right. \\
w &= \frac{M_1}{2I_1}\left(a_{35}xy + a_{34}y^2 + a_{33}y(2z - L)\right)
\end{aligned}
\tag{2.8}
$$

where I_1 is the centre-mass inertia momentum of the plate in the x direction, a_{ij} the components of the compliance tensor, which are periodic functions of the crystal orientation.

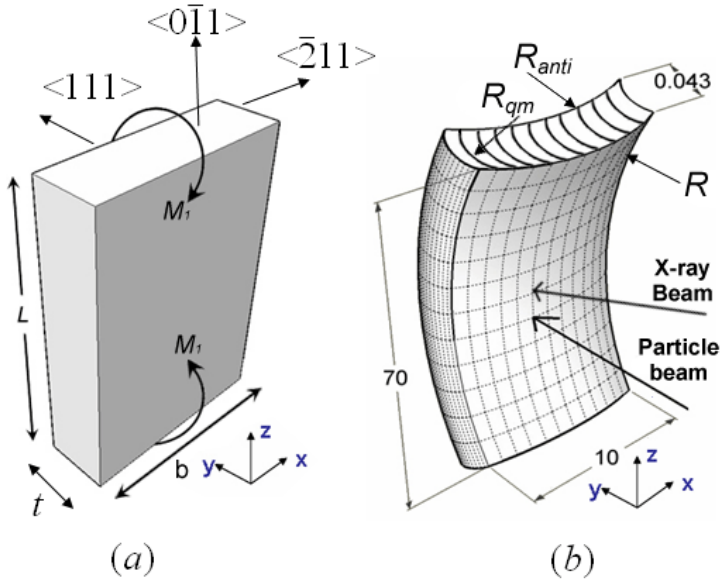

(a) (b)

Figure 2.31 Sketch of the unbent silicon plate with height L and thickness t with the <111> crystallographic axis along y axis. As a couple of forces with momentum M_1 is exerted at its edges crystal bends as in b. (b) External forces generate a primary curvature with radius R, which results in a secondary curvature with radius R_{qm} due to anisotropy-induced deformation. Unwanted anticlastic deformation with radius R_{anti} also appears as a result of primary bending.

For an isotropic material, it holds $a_{ij}=0$ for either $i>3$ or $j>3$ and $i \neq j$. Anticlastic deformation, which have been already described, yields a parabolic profile of deformation proportionally to a_{13}, $v \sim a_{13}x^2$. Anticlastic deformation arises in any material (crystalline or amorphous). While for amorphous materials the coefficient a_{36} is always null, for monocrystalline materials it may be different from zero. In this case the couple of strength M_1 may deform the planes parallel to the coordinate plane y-z to a parabolic shape $u \sim y^2$ through coefficient a_{36}, as schematically shown in Fig. 2.31(*b*). This deformation is called "quasi-mosaic" (QM) [5.9]. If the crystal plate is cut with the crystallographic orientation as in Fig. 2.31(*a*), the calculation of the compliance tensor for Si shows that the a_{36} coefficient is not zero, so the QM-related bending radius equal to $R_{qm} = \left|a_{36}/a_{13}\right| \cdot R$ and anticlastic bending radius equals to $R_{anti} = \left|a_{33}/a_{13}\right| \cdot R$. Therefore, under small deformation regime, both anticlastic and QM deformations are expected in this geometry. Indeed, the presence of anticlastic deformation has negative effect in beam steering because it limits the portion of the crystal aligned for channeling. Although methods to compensate for unwanted anticlastic deformation do exist, e.g., the usage of suitably shaped frames to hold the crystal [5.27], we developed a technique to rule out anticlastic deformation for which no external force is needed other than the bending moment M_1. In fact, anticlastic deformation can be prevented in the case of high-deformation regime, i.e., as Searle parameter β (see Eq 2.6) is much larger than the unity. More precisely, anticlastic deformation is present on the full width of the crystal for $\beta<1$ (low deformation regime, analytically described by Eq. (1)) or is confined on the crystal edges for $\beta > 100$ (high deformation regime)[5.24, 28], so that the central part of the crystal remains flat. Indeed, since the use of very thin crystals is sometimes demanded because of short dechanneling length, the plate deformation regime may easily be attained and, in some cases, is even unavoidable (β is in fact inversely proportional to t).

It is therefore crucial to investigate whether QM deformation is still present in the high-deformation regime and to what extent it does. Thereby, we performed an experiment with a highly deformed Si plate oriented as in Fig. 2.31(*a*) with b=10 mm, L=70 mm. The plate was diced from a 4 inches (111) Si wafer with low miscut (<0.05°), thinned to t=43 μm through a lapping machine. The crystal was bent through a mechanical holder, which ensured reproducible and stable bending. Dechanneling length for positive particles at 2 GeV in (110) silicon is about L_D = 1 mm, thereby for negative particles at the same energy it holds L_D = 0.1 mm, i.e., it by far exceeds the crystal length along the beam direction.

The sizing of the crystal was suggested for operation with some GeV electron beam because there are worldwide many electron facilities operating at an energy of this order of magnitude (e.g., [5.29-31]), for which channeling experiments may be a difficult task with currently available crystals.

HRXRD spectra were collected with a Philips MRD X-Pert PRO™ diffractometer. The kα_1 Cu x-ray beam was conditioned in order to obtain a beam divergence in the diffraction plane of about 40 μrad and a beam spot size of about 0.5x0.15 mm^2. Moreover surface profiles were measured by a white-light profilometer Veeco NT-1100.

Two different curvatures were investigated. The main radius of curvature of the two specimens, R, was measured and reported in Tab. IV (R=45.34 and 35.52 mm). In both cases the regime of high deformation is attained, β being much higher than 1 (see Tab. III) and therefore vanishing of anticlastic deformation is expected on the centre of the sample.

In order to quantify this prediction we measured the anticlastic curvature. In Fig. 2.32 we show the variation of the Bragg angle of a (444) HRXRD reflection as a function of the sample coordinate y (as defined in Fig. 2.30(*b*)) at the center of the sample (z=L/2) for the first specimen in Tab. III. This measure quantifies the local tilt of the (111) planes that are parallel to *x-y* plane and undergo anticlastic bending. Tilt integration allows reconstructing the *x-y* surface profile (Fig. 2.33(*b*) continuous line). In Fig. 2.33(*b*) the measured shape is compared to the parabolic shape predicted by small-deformation theory, i.e. by Eq. (2.8) (dashed line) and to a large-deformation theory prediction (dotted line) as in Refs. [5.24, 28]. As expected, the small-deformation theory does not correctly apply to our sample while good agreement with Refs. [5.24, 25, 28] is obtained. In particular, the *x-y* surface profile highlights a strong reduction of anticlastic bending especially on the center of the crystal (x=0) where it appears quite flat over a large portion of the section. In fact, while, according to the small-deformation theory, the curvature radius associated to anticlastic deformation, R_{anti}, should be 173 mm, the measurements revealed R_{anti}=3660 mm on the centre of the sample. As a second step, we measured the QM curvature R_{qm}, by means of HRXRD as explained in the following. The samples were aligned in order to reach the (224) Bragg reflection conditions with the incoming beam laying in the *x-y* plane at about 56° from the *y*-axis and the reflected beam was collected in transmission mode. More in detail, the (112) planes, containing the <111> axis to be used for channeling, caused the Bragg reflection. X-ray spectra were collected by measuring the reflected intensity during the rotation of the sample around the vertical *z*-axis, perpendicularly to the diffraction plane. Since the (112) crystalline planes were bent, only a part of such planes was under Bragg condition. By tilting the sample, different portions of the planes were set under reflection and therefore the angular width of the scan was a direct measurement of the angular spread due to the curvature of the crystal planes under analysis. In Fig. 2.32, three (224) diffraction spectra on different samples are plotted. The dashed line is relative to a non-bent (flat) sample. The full width at half maximum of the scan is in good agreement with the X-ray beam divergence and therefore provides a measurement of the resolution of the diffractometer. The other two curves pertain to the samples bent at *R*=45.34 and 35.52 mm. Their shape is the convolution of a water-bag distribution with the resolution of the instrument. The broadening of the angular distribution clearly demonstrates that QM bending is present in the samples even in the high-deformation regime

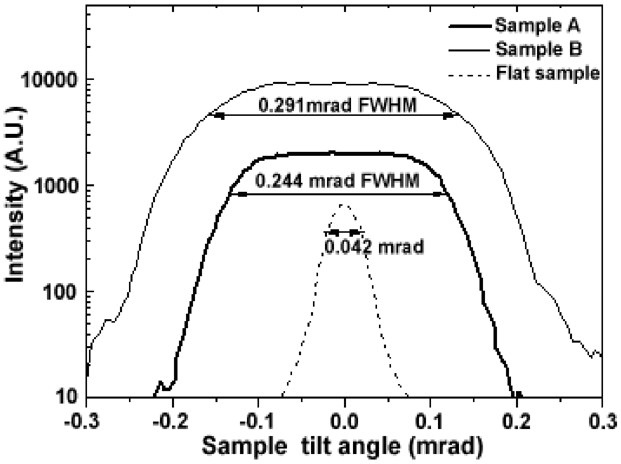

Figure 2.32 High resolution X-ray diffraction scans in the neighborhood the (224) Bragg angle for 3 different samples. A non-bent (flat) samples (dashed line), a sample with a main curvature *R* = 45.34 mm (thick solid line, sample A) and a sample with an *R*=35.52 mm (thin solid line, sample B). FWHM values are indicated by arrows. The intensity scales of the scans are arbitrarily rescaled for the sake of figure clarity.

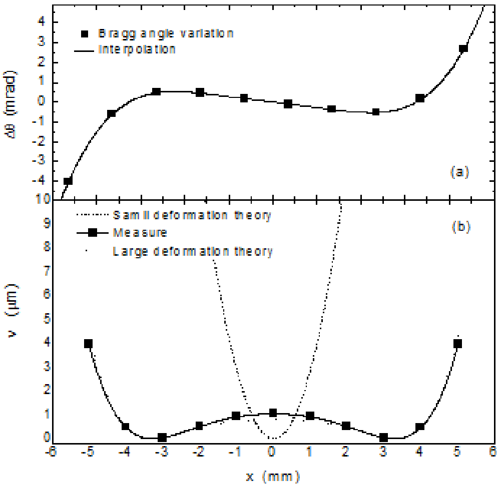

Figure 2.33 Measurement of anticlastic deformation for sample A. (*a*) Tilt of the (111) plane as a function of the lateral *x*- coordinate measured in the middle of the curved sample. (*b*) Integration of the tilt provide the (111) plane profile (continuous line); for comparison the dashed line quantify the profile as estimated by small deformation theory according to Eq. (2.8). As can be noted the real shape shows a strong flattening of the anticlastic deformation due to high deformation regime.

The width of the curves allows the determination of QM bending, θ_{FWHM}, which turned out to be θ_{FWHM}=0.244 mrad and θ_{FWHM}=0.291 mrad for the two samples. Moreover, the radius of curvature of (112) planes due to QM bending can be determined:

$$R_{qm} = \frac{t}{\vartheta_{\mathrm{FWHM}}} \tag{2.9}$$

Table III summarizes the measurements and comparatively reports the expected values of R_{qm} to the corresponding expected radii in the limit of small deformation regime.

Table IV. Summary of measured and calculated quantities of the two bent crystals. *R* is the main curvature radius as measured by optical interferometry, θ_{FWHM} is the width of the (112) x-ray diffraction scans, *t* is the sample thickness, R_{qm} is the secondary curvature due to QM effect measured by XRD and estimated by the small-deformation theory. Last column is the Greenenko-Shul'ga parameter for 1 GeV electron beam; it holds *k*<1 in both cases, i.e., efficient AC is enabled.

Sample	**R (mm)**	**β**	**θ_{FWHM} (mrad)**	**t (um)**	**R_{qm} (mm)**		**k**
					measured	expected	
A	5.34	51	0.244	43	176	54	0.017
B	5.52	65	0.291	43	148	21	0.024

The agreement between measured and theoretical values of R_{qm} is indication that QM deformation is poorly perturbed by the high-deformation regime.

As from Table III It is important to remark that for both the crystals the Greenenko-Shulga (see Eq. 1.22) is much less than the unity, this allows to reach deflection through axial channeling.

The crystal proposed in this work can be directly applied for steering some-GeV negatively charged particle beams with the purpose of collimation/extraction from an accelerator, manipulation of anti-proton beams[5.32], emission of coherent radiation from electrons in an undulator [5.33], and others.

References

[2.1] Baublis, Fermilab preprint FN-608 Batavia(1993)
[2.2] V. M. Biryukov *et al.*, *Crystal Channeling and Its Application at High-Energy Accelerators*. 1997 Berlin: Springer.
[2.3] M. D. Bavizher, IHEP Preprint 89 (1989)
[2.4] Y. A. Chesnokov *et al.* Proc. of PAC-91. 1991. San Francisco.
[2.5] V. V. Jensen *et al.*, CERN SL 92-14(1992)
[2.6] R. A. Carrigan *et al.*, Phys. Rev. Spec. Topics. Acc. and Beams. **5** 043501 (2002)
[2.7] A. Baurichter *et al.*, Nucl. Instr. and Meth. B. **119** 172 (1996)
[2.8] A. G. Afonin *et al.*, Phys. Rev. Lett. **87** 094802-1 (2001)
[2.9] Y. M. Ivanov, J. Exp. Theor. Phys. Lett. . **81** 129
[2.10] Baricordi *et al.*, App. Phys. Lett. **87** 094102 (2005)
[2.11] B. Schwartz and Robbins H., J. Electroch. Soc. **123** 1903 (1976)
[2.12] L. C. Feldman *et al.*, *Materials Analysis by Ion Channeling: Submicron Crystallography*. 1982, Riverport Academic Press.
[2.13] G. D. Mea *et al.*, eds. *Atomic Collisions in Solids Vol. 2, pp. 811–817.* 1975, Plenum: New York.
[2.14] J. H. Barret, Phys. Rev. B. **3** 1527 (1971)
[2.15] V. M. Biryukov *et al.*, Nucl. Instrum. Meth. Phys. Res. B. **234** 23 (2005)
[2.16] H. Seidel *et al.*, J. Electrochem. Soc. **137** 3612 (1990)
[2.17] J. W. Gardner *et al.*, *Microsensors MEMS and Smart Devices*. 2001, New York: Wiley.
[2.18] W. Scandale *et al.*, Rev. Sci. Instrum. **79** 023303 (2008)
[2.19] K. R. Williams *et al.*, Journal of Microelectromechanical Systems. **12** 761 (2003)
[2.20] S. Timoshenko, *Theory of Elasticity*. 1970, New York: McGraw-Hill Companies.
[2.21] J. J. Wortman and Evans R. A., J. Appl. Phys. **36** 1 (1965)
[2.22] S. G. Lekhnitskii, *Theory of Elasticity of an Anisotropic Body*. 1981, Moscow: Mir Publisher.
[2.23] G. F. C. Searle, *Experimental Elasticity*. 1920, Cambridge: Cambridge University Press.
[2.24] S. K. Kaldor and Noyan I. C., Appl. Phys. Lett. **80** 2284 (2002)
[2.25] S. K. Kaldor and Noyan I. C., Mat. Sci. Eng. A. **399** 64 (2005)
[2.26] V. M. Biryukov, Nucl. Instrum. Meth. Phys. Res. B. **234** 23 (2005)
[2.27] Y. M. Ivanov, *CARE Workshop*: CERN.
[2.28] D. G. Ashwell, Journal of Royal Aeronautical Society. **54** 708 (1950)
[2.29] S. Guiducci. Proc. of the 1999 Particle Accelerator Conference. 1999. Piscataway: IEEE.
[2.30] A. Jankowiak *et al.* Proc. of 11th European Particle Accelerator Conference. 2008. Genoa.
[2.31] T. Iijima, Nucl. Instrum. Meth. A. **446** 65 (2000)
[2.32] U. I. Uggerhoj *et al.*, Nucl. Instrum. Meth. B. **207** 4 (2003)
[2.33] M. Tabrizi *et al.*, J. Phys. G: Nucl. Part. Phys. **34** 1581 (2007)

Chapter 3

Coherent interactions between positively charged particles and crystals

In the last years a series of experiment carried on by the collaborations H8-RD22 and UA9 studied coherent interactions between positively and negatively charged particles beams with bent crystals. Such experiments, carried on at CERN with high energy particles, opened up new possibilities to steer particle beams.

3.1 The experimental setup

Experiments have been carried on H8 and H4 extracted lines, with 400GeV protons and 150 GeV positive and negative particles. The experimental setup, whose main components are silicon detectors, a high resolution goniometer and the crystal, have been improved during the years, in the following the main components are described.

3.1.1 Silicon microstrip detectors

The detection system is based on four modules of silicon microstrip telescopes developed by INFN Trieste [5.1]; each module (the box is 12x50 cm^2 and 4 cm thick) consists of a silicon strip detector and its readout electronics. The detector sensitive area (1.92×1.92 cm^2) is a double sided high resistivity silicon microstrip detector, 300 μm thick. The p-side of the detector has a p^+ implantation strip every 25 μm and a readout pitch of 50 μm while the n-side (which is perpendicular to the p-one) has n^+ implantation strips every 50 μm, separated by p^+ blocking strips. The p-side which has the best resolution (thanks to the presence of a floating strip) has been used to measure the horizontal direction in which the crystal deflection takes place. Each detector side has 384 DC-coupled strips; the AC coupling to the electronics is performed with external quartz capacitors. The strips are readout by 3 low noise VA2 (IDEAS) ASICs with a multiplexed readout at 5 MHz; they are glued on a thin substrate of ceramic which provides the distribution of the digital control signals to the ASICs and takes the analog ones to the frontend electronics (the so called repeater boards), which is located near the detectors. This second generation of detectors allows for higher resolution in reconstructing particles trajectory and higher data acquisition rate.

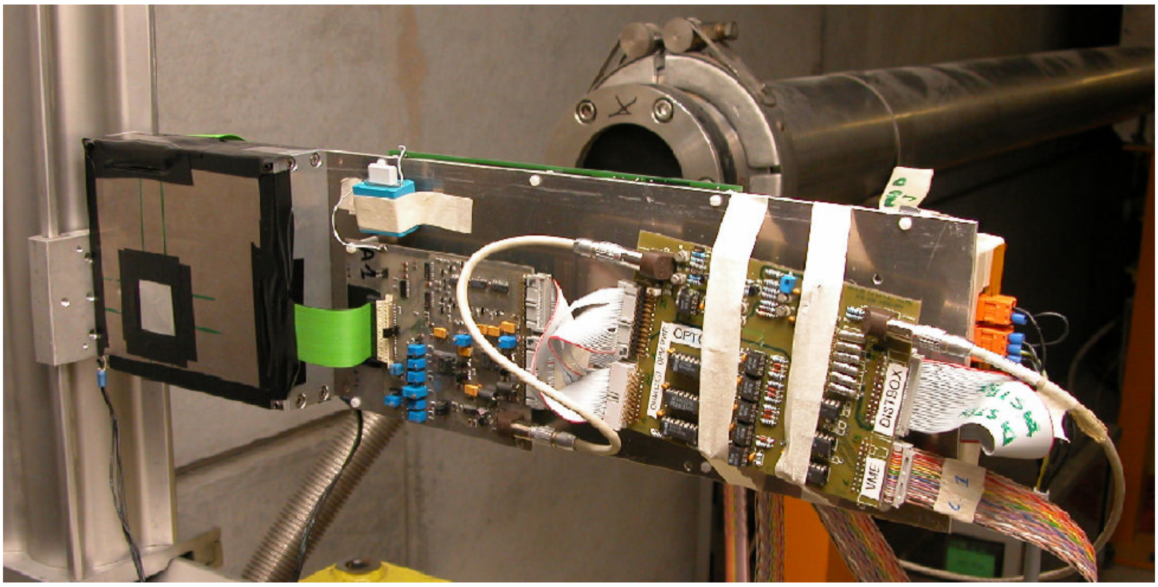

Figure 3.1. The second version of silicon detectors with electronic modules

3.1.2 The goniometer

The highest energy of particle used in our experiments is 400 GeV, at this energy the planar channeling critical angle is 10 μrad, and being this the lowest angle involved in our experiments it determines the required angular goniometer resolution. The crystals typically have a transverse thickness ranging from some hundred of mm to some cm. Such quantity constrains on the features of the goniometer, which besides the angular alignment, is designed to allow precise positioning of the crystal on the beam. It consists of:

- a rotational stage in the horizontal plane, which is used to align the crystal with respect to the beam (360° range)
- a cradle in the vertical plane, which is used to reach axial channeling alignment
- a linear stage to position the crystal on the beam (52 mm range)
- a second linear stage to put the crystal holder on the rotational axis (102 mm range).

The translational stages have a positioning accuracy of 1.5 μm , a bidirectional repeatability of 2 μm and a resolution of 5 μm over the whole range. The rotational stage has 1 μrad average accuracy, 1 μrad repeatability and 1 μrad resolution. The accuracy is defined as the difference between the real and the nominal position of the stages; the repeatability is the spread of the stage positions in case of repeated motion to the same value. The resolution is defined as the smallest possible step of the translation/rotation movement. In order to improve the mechanical stability of the goniometer and to precisely define its relative position with respect to the beam, the whole system was installed on a granite table with high planarity and small roughness. The readout of the angular and linear stages position is performed by optical encoders; the system is remotely controlled via PC and the information from the encoders is stored in dedicated data files by the data acquisition system.

The different parts are assembled as in Fig 3.2

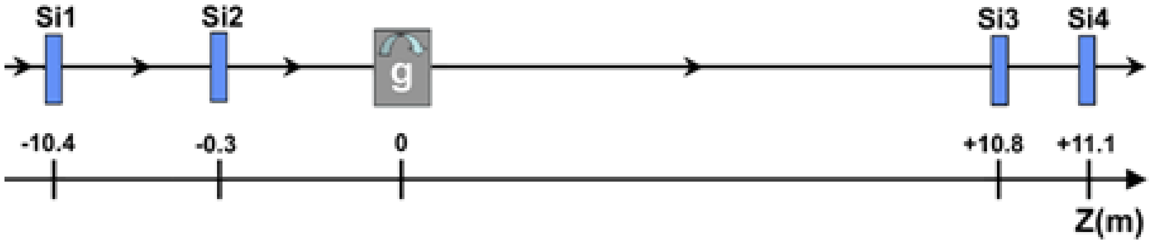

Figure 3.2 **Experimental layout on the H8 beam line at the CERN SPS. Si1-Si4 are the silicon microstrip detectors, g is the goniometer. The beam axis line is shown.** The distances indicated in the figure are typical of every setup, but may slightly vary from experiment to experiment depending on the available space on the experimental area.

Such experimental setup, together with dedicated data analysis software, allows on-line reconstruction of particles trajectories with angular resolution of few μrad. Typical output of the data analysis software is a picture as the Fig. 3.3.

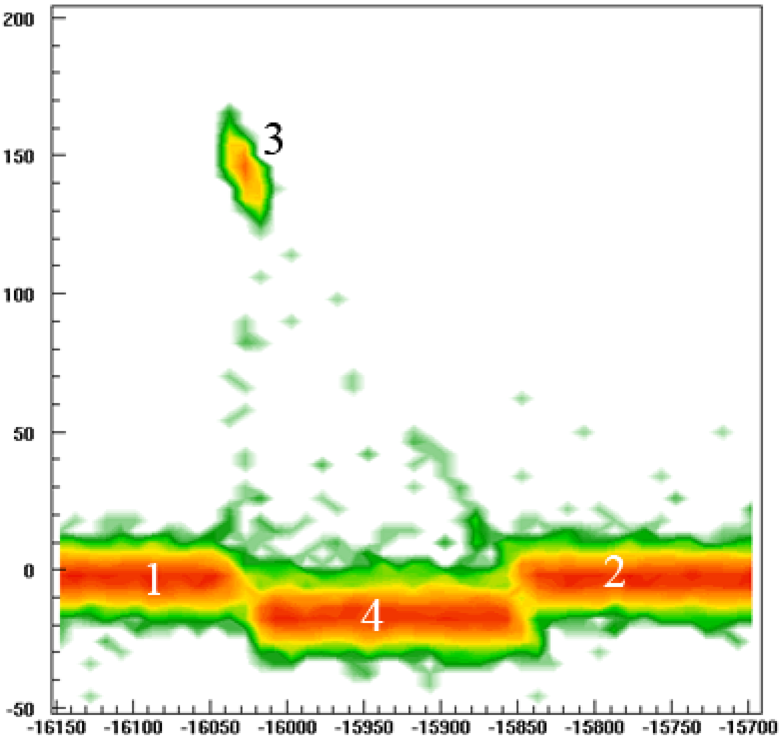

Figure 3.3 Typical result of an angular scan. In regions (1) and (2) the crystal is misaligned with respect to the beam, in (3) is in channeling, and in region (4) in VR. More details will be given later

The horizontal axis is the goniometer angular position, the vertical one is the deflection angle of the particles which interacted with the crystal. Channeling and VR effect correspond to regions (3) and (4), respectively. In regions 1 and 2 the crystal is misaligned and behaves as an amorphous.

3.2 Setting up.

After fixing the crystal to its holder on the goniometer some preliminary operations are accomplished in order to speed up the experiment.

3.2.1 Crystal pre-alignment

The first operation to accomplish is to pre-align the angular position of the crystal with respect to the beam direction. This procedure is absolutely needed to fasten the angular alignment of the crystal to the particle beam.

Assuming that the particle beam is parallel to the beam pipe, and that the crystalline planes are parallel to the crystal surface, a laser is positioned in such a way to be as most as possible parallel to the particle beam pipe. With a pentaprism the laser is directed onto the crystal surface, and is subsequently reflected back. Using the goniometer, the crystal is rotated until the incident and the reflected laser beam coincides, this is achieved vanishing the distance *d* in Fig.3.4.

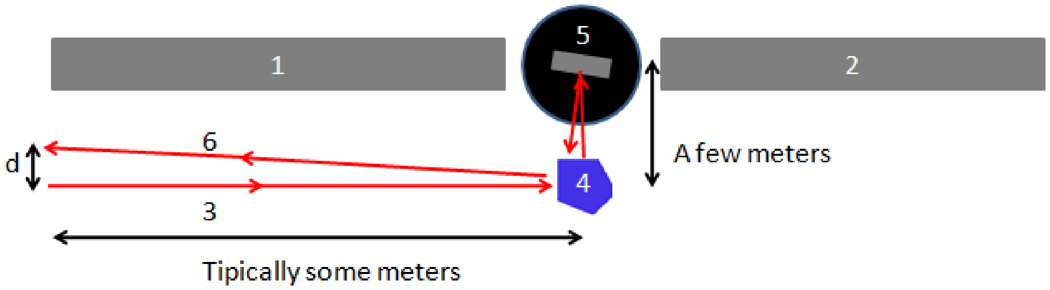

Figure 3.4 Prealignement system 1 and 2 are the particle beam pipe, 3 and 6 the incidendent and reflected laser beam, 4 the pentaprism, 5 the goniometer (black) and the crystal (grey)

In such a way the crystal is angularly pre-aligned to the beam typically within 1 mrad accuracy.

3.2.2 *Lateral alignment*

The lateral position of the crystal is pre-aligned with respect to the beam path (see Fig. 3.5)

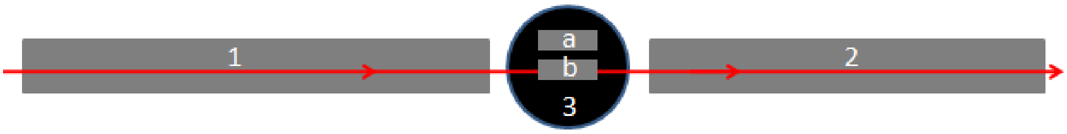

Figure 3.5 lateral pre-alignment of the crystal with respect to the particle beam (in red).(1) and (2) the beam pipe, whose center is taken as reference 3 is the goniometer with the crystal (in grey) If the crystal is position a it does not intercept the beam. The goniometer is set up in such a way that that the crystal is in position b, i.e. roughly on the beam path.

A preliminary pre-alignment of the crystal is realized by visual inspection of the position of the crystal with respect to the center of the beam pipe, which is taken as reference of the particle beam path. Accuracy of this alignment is typically within 1 cm. The beam size is typically 2-3 mm, so a fine scan is made in order to precisely position the crystal on the beam path. Fig. 3.6a shows the particles angular deflection in horizontal direction as a function of the horizontal crystal position when the crystal is not on the beam, while Fig. 3.6b shows the same quantities when the crystal is correctly positioned on the beam. In correspondence of the crystal the beam divergence is increased due to multiple scattering with the crystal, this allows to easily recognize the crystal position on the beam.

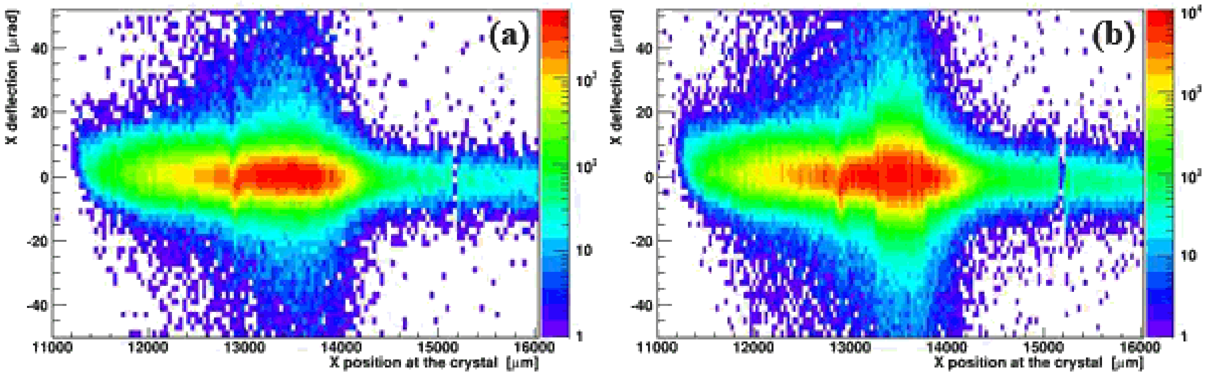

Figure 3.6 Beam deflection in horizontal direction as function of the horizontal position on the crystal. a crystal is not on the beam b the crystal is in the center of the beam and is clearly recognized due the multiple scattering caused to the beam.

3.2.3 Torsion compensation

Exploiting the possibility offered by silicon detectors and data analysis software to reconstruct the particle tracks, it has been found that the crystal is subject to mechanical torsion due to imperfections in its mounting and/or mechanical imperfections of the bending holder. Fig 3.7a shows the beam deflection angle as function of the vertical position along the crystal.

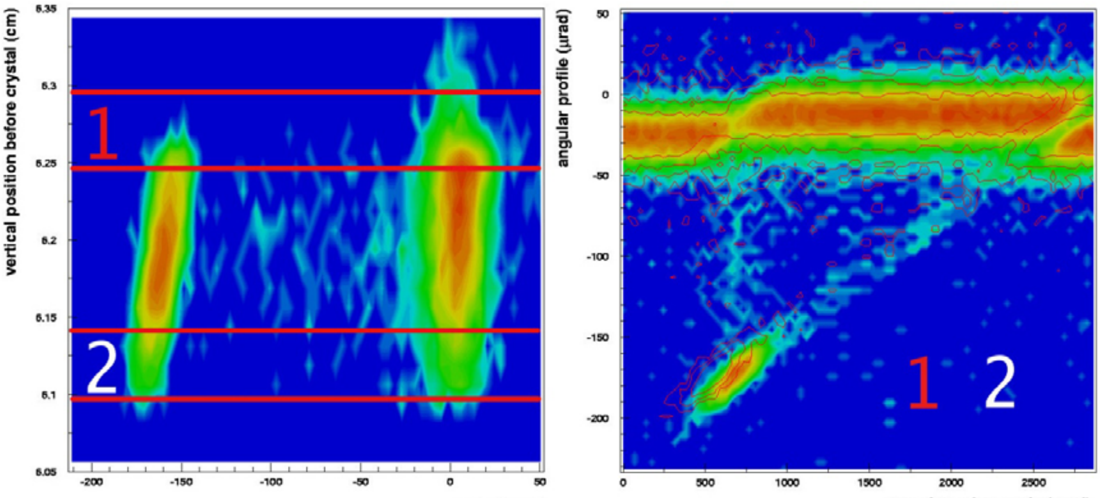

(a) (b)

Figure 3.7. (A) deflection angle in channeling alignment as function of the vertical position of the crystal, b angular scans corresponding to two different slices of the crystal.

By selecting only the particles impinging onto the portion of the crystal marked as 1 in Fig. 3.7a, the angular scan represented with red contour lines in Fig 3.9b has been obtained, while selecting the particles impinging on a region lower of 1500±100 μm (indicated as 2) we obtain the colored angular scan of Fig 3.8b. The distance between the two channeling peaks is 14.37±2.65 μrad, which is due to torsion by 9.58±1.89 μrad/mm. A significant improvement the crystal holder used in this first experiment allows complete removal of torsion in a strip-like crystals. In Fig 3.8a is represented particle deflection angle as a function of the vertical position along the crystal before torsion compensation. Region 1 corresponds to channeled particles, 2 to undeflected particles and 3 to volume reflected particles. Fig 3.8b shows beam deflection as a function of the vertical position after torsion compensation. Each portion of the crystal intercepted by the beam is acting now in the same way. A linear fit of the deflection angles allows to measure torsion, which is decreased from 34 to 0.9 µrad/mm.

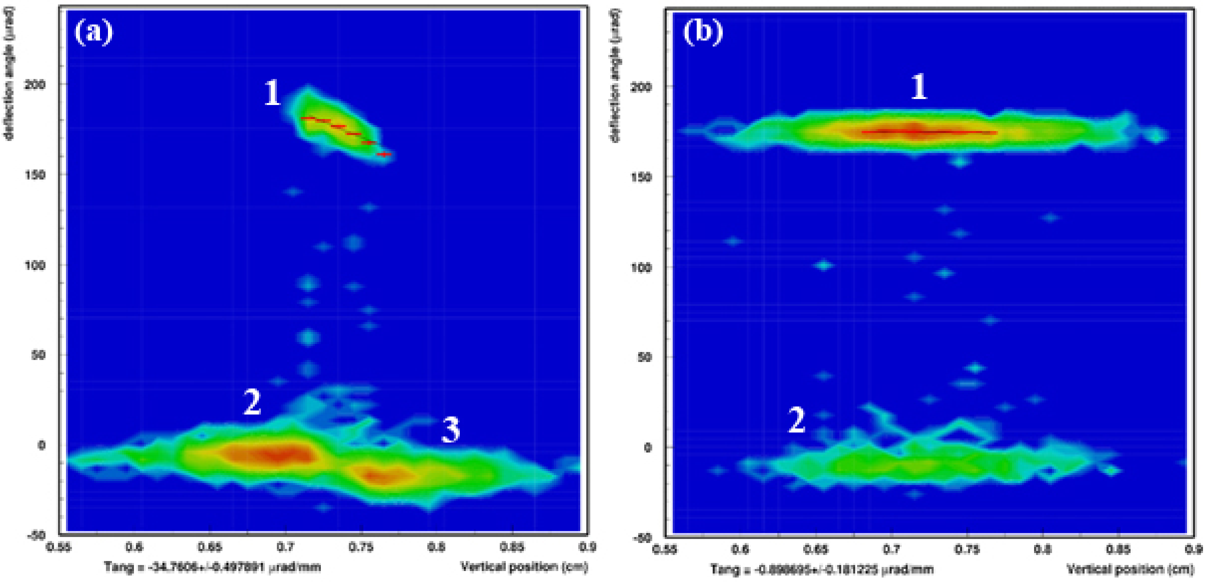

(a) (b)

Figure 3.8. Particles deflection angle as function of vertical position along the crystal. a before torsion correction b after torsion correction. In both a and b region 1 represents the deflected beam and 2 the undeflected beam. In a, region 3 corresponds to volume reflected particles. Due to crystal torsion different regions of the crystal are oriented in different way along the vertical direction, so a region of the crystal is aligned in such a way to excite VR instead of channeling. After torsion compensation this spot is not more present. A linear fit of the deflection maximum of deflection angles give the torsion in µrad/mm.

3.3 Planar channeling in short bent crystals

A previous work [5.2] studied channeling deflection efficiency of a 450GeV protons as a function of the bending angle of a 50mm long silicon crystal bent in a range from 50 m to 4 m. Top deflection efficiency was found out to be lower than 50%. With the aim to increase deflection efficiency and to study its dependence on the bending radius in short crystals, we fabricated by anisotropic chemical etching a strip crystal with (110) channeling planes and length along the beam of 1.94 mm. The crystal, named ST9, was bent at several bending radii spanning from 2.4 to 38 m.

Channeling efficiency as function of the bending radius is presented in Fig. 3.9 for a beam divergence of 5 µrad.

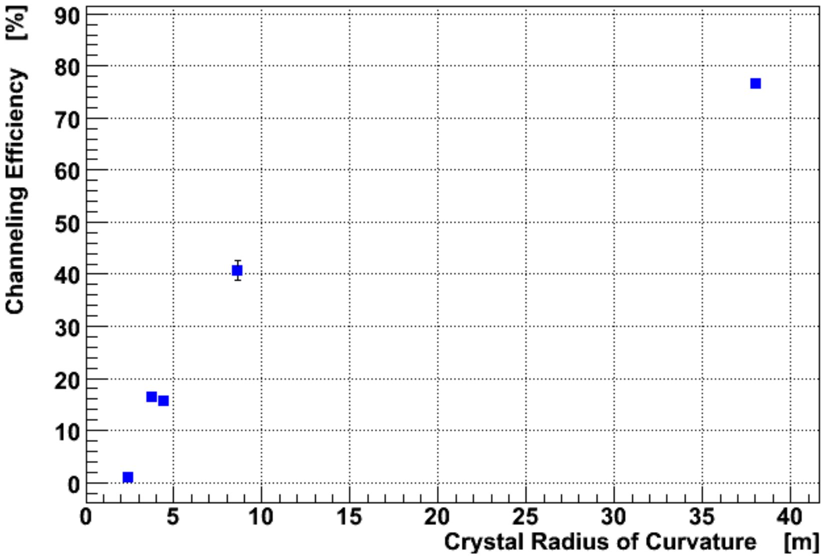

Figure 3.9 Channeling efficiency as function of the bending radius for a short crystal

At low bending radius the real values of channeling efficiency are limited by crystal torsion, while at larger radius torsion is not present. In fact, for such samples the procedure of torsion compensation was not worked out.

Data for the larger bending radius have been extensively analyzed. By selecting the particles impinging onto the crystal at different angles it is possible to study the channeling efficiency as a function of the incoming beam divergence. The fractions of particles with horizontal incident directions inside contiguous angular windows each of 2 μrad width were selected. For the case of 38 m bending radius, Fig.3.10 shows the measured deflection efficiency values (blue squares interconnected by segments) for each beam fraction as a function of the window center position. The maximum value of the deflection efficiency corresponding to the optimal choice of the incoming particle directions is P_d=(83.4±1.6$_{\mathrm{stat}}$±0.9$_{\mathrm{syst}}$)%. Such a value is significantly larger than the upper theoretical limit established for long crystals [5.2, 3]. The simulation results, based on the model described in [5.3], are shown in Fig.10 as circles interconnected by segments. The agreement of simulation and experimental results is rather good in a wide range of incident angles around the incoming beam axis

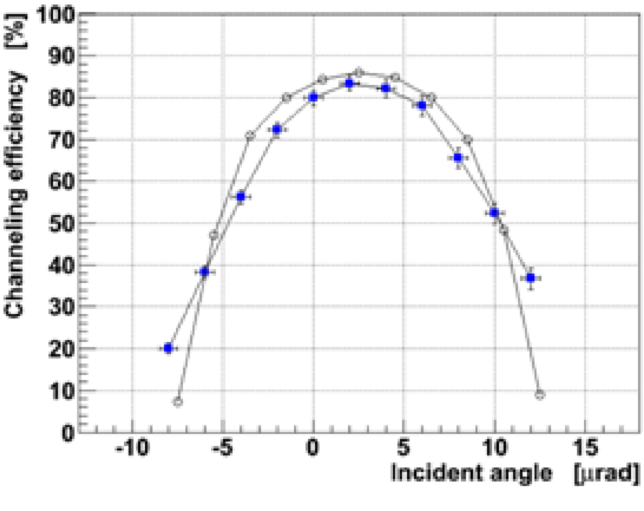

Figure 3. 10 Deflection efficiency for a narrow beam fraction, which is inside an angular window of 2μrad width, as a function of the window center position. The maximum value of the efficiency is (83.4±1.6stat±0.9syst)%. Circles indicate the simulation results.

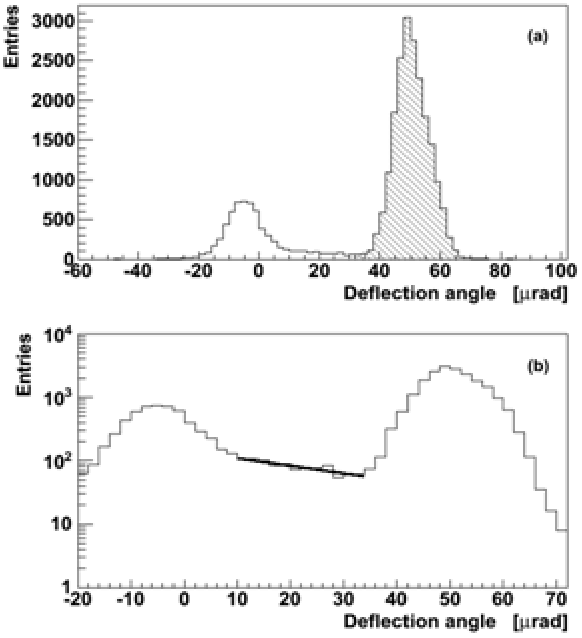

Figure 3.11. Distribution of deflection angles for 400-GeV/c protons in the silicon crystal bent along (110) planes, the crystal length is 1.94 mm. Only particles hitting the crystal with the horizontal and vertical angles |θxo|, |θyo| < 5μrad were selected. (a) The deflected fraction 76.6% is hatched. (b) Logarithmic scale along Y axis. The exponential fit, which gives the nuclear dechanneling length, is shown by the line between the two maxima.

A so high deflection efficiency can be explained measuring the nuclear dechanneling length. As discusses in chapter 1, some particles may leave their bound state due to multiple Coulomb scattering on either nuclei (MSN) or electrons (MSE) of the crystal atoms (dechanneling processes).

Fig 3.11 shows the beam profile under channeling alignment. The fraction of particles deflected by angles greater than θ_d-3σ_d (hatched area in Fig.3.11a) determines deflection efficiency P_d. For a divergence of 5μrad we have P_d=(75.2±0.7$_{\mathrm{stat}}$±0.5$_{\mathrm{syst}}$)%. The peak on the left side in Figs.3.11a and 3.11b is due to the particles that were not captured into the channeling states at the crystal entrance. They were deflected to the opposite direction due to volume reflection (see chapter 1). Particles with deflection angles between the two maxima in Figs.3.11a and 3.11b are dechanneled due to MSN. Using the relation $l=R\theta$ between the deflection angle θ and crystal length l traversed by a particle before the dechanneling event, the exponential fit of the area of dechanneling (see the line in Fig.3.11b) gives the value of the nuclear dechanneling length L_n=(1.53±0.35$_{\mathrm{stat}}$±0.20$_{\mathrm{syst}}$) mm, which is in a good agreement with the value L_n=1.5 mm estimated by numerical simulations.

For protons of 400 GeV energy scattering with electrons leads to a dechanneling length of about 22 cm (See Chapter 1, Eq. 1.13), so deflection inefficiency of so short crystals relies only on nuclear dechanneling. By simulations it has also been found that capture efficiency in stable channeling states at the entry face in the crystal is 95% so deflection inefficiency due to the MSN, which also determines the fraction of dechanneled particles, is about 10%.

Our experimental results show that the deflection efficiency limit of higher than 80% for a nearly parallel beam predicted by theory in a single passage through a short crystal is really achievable. A fast stage of particle dechanneling due to multiple scattering on the atomic nuclei has been observed. The measured value of nuclear dechanneling length allows estimating the deflection efficiency for all possible applications of short crystal deflectors.

3.4 Deflection of 400 GeV proton beam by means of axial channeling

Theoretical considerations on the possibility to steer particles beams by means of axial channeling have been already exposed in chapter 1. Pioneering experiments [5.2, 4] actually did not observe the beam deflection due to AC. Such experiments mainly highlighted a strong feed-in of particles into skew planar channels stretched to the side opposite to that of bending. A small beam fraction deflected up to the full crystal bending angle in the experiment described in Ref. [5.2] was later interpreted by simulation as partly generated by hyperchanneled particles [5.5].

With the aim to observe deflection of particles beams by axial channeling, the ST9 crystal (70x1.94x0.5mm^3) with the large faces parallel to the (110) crystallographic planes was used for the purpose. This crystal allows to study axial channeling along the <111> crystalline direction. Crystal was placed in a vertical position in such a way that the proton beam entered the crystal through its side face nearly parallel to the large faces (see Fig. 3.12).

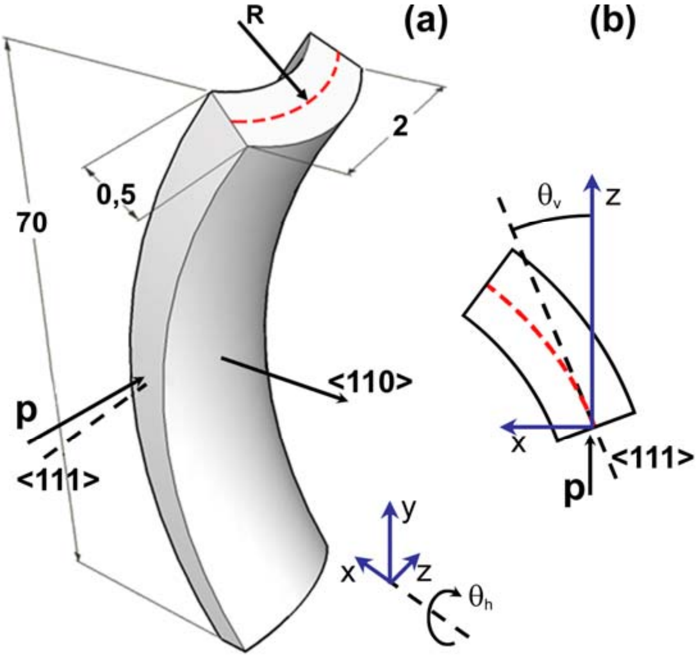

Figure 3.12. (A) Schematic picture of a silicon crystal bent by anticlastic deformation along the <111> axis. b Cross-sectional view of the crystal. Dimensions are expressed in mm.

The bending angle was α=50 μrad and the corresponding bending radius R=38 m. The critical angle for AC of 400 GeV/c protons along <111> direction is ψ_C=20.7 μrad (i.e., more than two times the critical angle for planar channeling), the equalization length λ=15.8 μm, and thereby condition (see Chapter 1, Eq. 1.22) was satisfied.

The angular divergence of the primary beam along the horizontal and vertical planes were measured as σ_x=8.8 μrad and σ_y=5.2 μrad (root mean squared values), respectively.

After installation, an angular scan of the crystal around the vertical axis (θ_v) was done to make the (110) planes parallel to the beam direction. Then, angular scans were performed at different cradle angles (θ_h) to reach the best possible alignment of the <111> axis with the beam.

Fig.3.13 shows beam intensity distributions as a function of the particle deflection in the horizontal (θ_x) and vertical directions (θ_y) due to interaction with the crystal at three different values of θ_v. When the beam direction is far from the axial direction the beam is undeflected, resulting in a spot, not shown in the figure, centered in (θ_x, θ_y)=(0,0) with standard deviations equal to the beam divergence quoted above. As θ_v becomes close to the alignment condition, the distribution in Fig.3.13a is observed. A large fraction of the particles is still undeflected though part of the beam is deflected due to scattering by atomic strings and feeding into skew planar channels. The bottom spot is more intense than the top spot due to non perfect alignment of the crystal with respect to the beam in the direction of θ_h. With increasing θ_v, the distribution is further modified as depicted in Fig.3.13b. Here only a small fraction of the beam remains undeflected. Axial channeling along the <111> axis occurs and deflects the beam by the angle of about 50 μrad, consistently to the previous determination under planar condition. A fraction of the initial axially-channeled particles is leaked into skew planar channels because the <111> axis is the intersection of several planes.

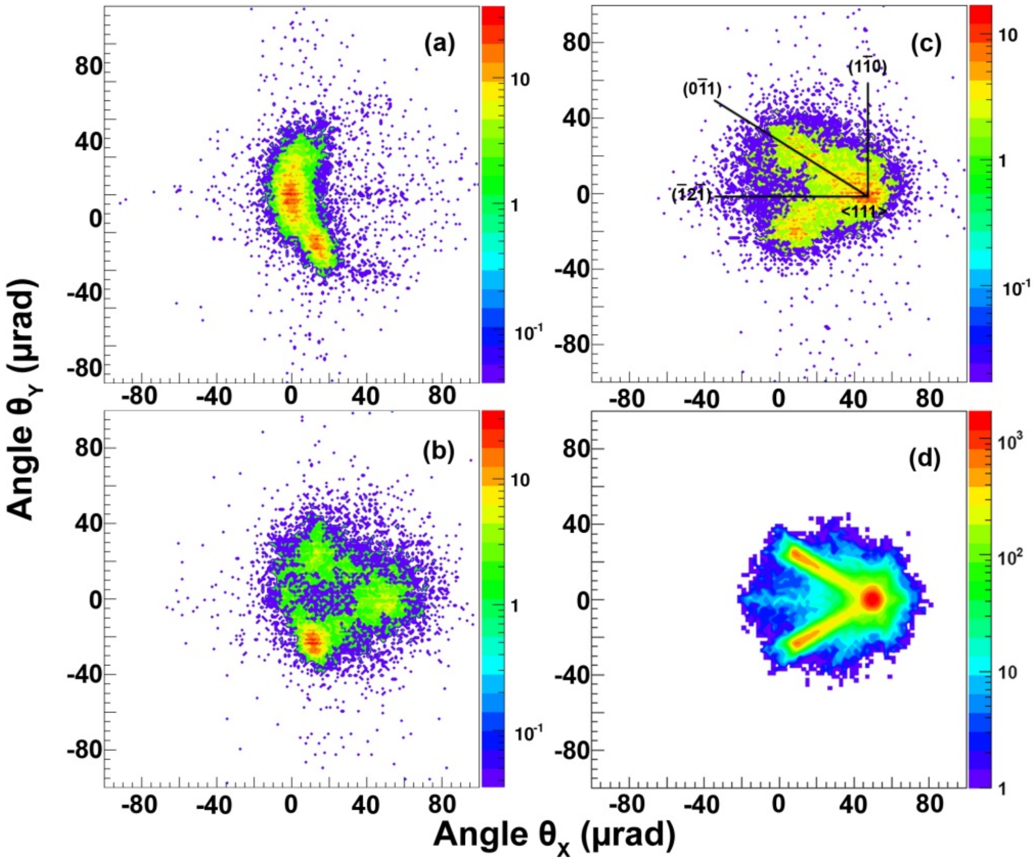

Figure 3.13. Beam intensity distribution as a function of horizontal and vertical deflections at some orientation angles (θv) of the <111> axis with respect to the incident beam direction: (a) -θv = 40 μrad, (b) θv = -15 μrad, (c) θv = 0 μrad. Only the particles hitting the crystal are shown in the pictures. The angular distribution corresponding to the simulation of the experimental conditions, in case of perfect alignment of the <111> axis with the beam direction and of a large number of particles hitting the crystal, is shown in (d) for comparison with the experimental case (**c**).

Scattering with <111> atomic strings can accidentally direct a particle parallel to one of the skew planes, and then the crystal bending strengthens the stability of this planar motion. Deflection of particles due to channeling towards the strongest (110) skew channels is clearly observed as two tails departing from the axial spot.

The best alignment condition is shown in Fig.3.13c. The un-deflected part of the beam has completely disappeared and the spot corresponding to axial channeling is the most populated by beam particles. We clearly observed a “swallow” tail, which is formed by deflection of particles due to axial channeling (rightmost spot), and channeling into skew planar channels (two symmetric spots in the left), as predicted by simulation [5.5]. In contrast to planar channelling, a distinctive feature of AC is the disappearance of the spot pertaining to the unperturbed beam.Fig.3.11d shows the angular distribution for 400 GeV/c protons deflected at a perfect alignment with the <111> axis of a bent silicon crystal as simulated for the conditions of the experiment. The simulation used the model of atomic-string lattice [5.6] with the atomic potential and electron density under the Doyle-Turner approximation for the atomic scattering factors. The simulation allowed one to estimate the contribution of hyper-channeled particles to the distribution peak near the full bending angle, which turned to be smaller than 2% even for perfect alignment of the crystal axis with the beam. Such level is consistent with previous determinations of efficiency.

The horizontal projection of the experimental distribution for almost perfect axial alignment (Fig. 3.13c) is shown in Fig.3.14.

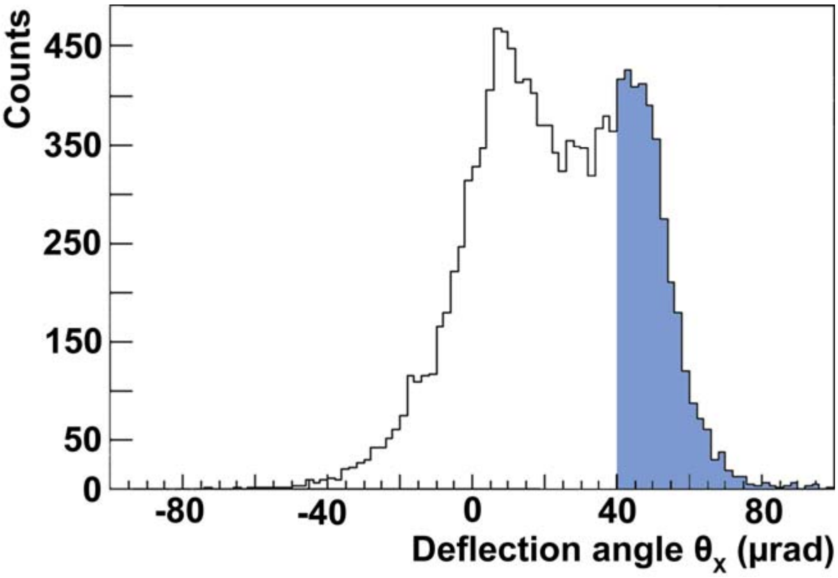

Figure 3.14. Horizontal projection of the two-dimensional distribution shown in Fig.3.13c. The angular region used for efficiency calculation (θv > 40 μrad) is highlighted.

Deflection efficiency due to AC can be estimated as the beam fraction whose horizontal deflection angle exceeds 40 μad. The particles with smaller deflection angles were dechanneled or captured by the skew channels with high probability. Deflection efficiency for AC was about 30%, i.e., beam deflection through doughnut scattering allowed to significantly enhance the number of deflected particles with respect to previous experiment, which relied solely on hyper-channeled particles.

In summary, deflection of high-energy protons via axial channeling in a bent crystal, mainly driven by the mechanism of doughnut scattering, was clearly observed. Hyperchanneling provides only a small contribution ~1% to the deflection efficiency. Summing up the contribution of doughnut scattering and of planar channeling in skew planes (which is a by-product of AC), it comes out that about 90% of the particles are deflected by the crystal.

On the strength of the high efficiency recorded, AC appears to be a traceable method for steering of high energy particle beams. In particular, AC would be particularly suited for the problem of halo collimation since most of the particles interacting with the beam are streamed out with non-negligible angle.

3.5 Single volume reflection in a single crystal

Single volume reflection in a single crystal was preliminary observed in [5.7] with 1 GeV protons and in [5.8] with 70 GeV protons. A third and more clear observation, which will be described here, was obtained at CERN [5.9] with 400 GeV protons using both strip and quasi-mosaic crystals.

A strip crystal of size 3x0.9x70 mm^3 was prepared by mechanical dicing and subsequent removal of the lattice damaged layer by isotropic etch. The crystal, offering (110) channeling planes was bent at an angle of 162 µrad. The planar potential for (110) planes is U_0=22.7 eV and corresponds to a critical angle of 10.6 µrad. Multiple scattering angle of 400 GeV protons in this crystal equals 5.3 µrad, therefore small with respect to the critical angle. The H8 beam line was adjusted to provide a divergence of (8±1) µrad, smaller than the critical angle. The beam spot size was of about 1 mm, i.e. of the same order of the transversal strip crystal thickness.

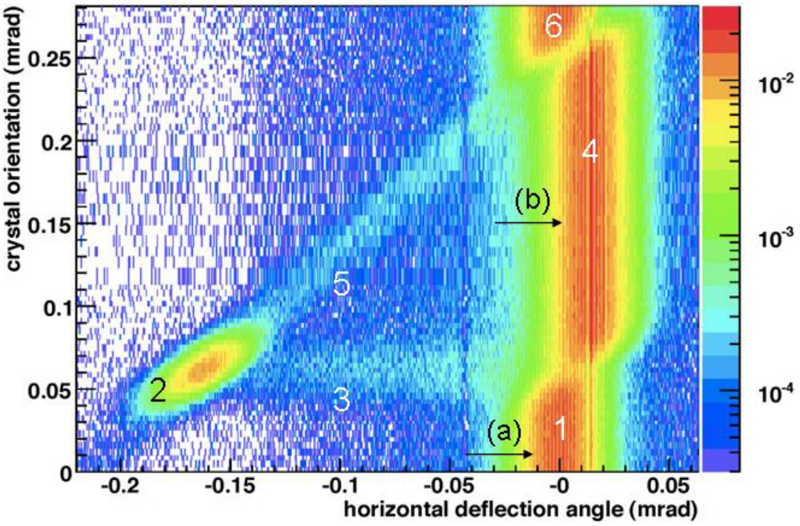

Figure 3.15. Beam intensity recorded by the silicon microstrip detectors as a function of the horizontal deflection angle (x axis) and the crystal orientation (y axis). Six regions can be distinguished: (1) and (6) nonchanneling mode; (2) channeling; (3) dechanneling; (4) volume reflection; (5) volume capture. The wider angular acceptance of volume reflection compared to channeling is clearly visible in the figure.

Fig. 3.15 shows a summary plot of an angular scan performed with the strip crystal. The horizontal angular deflection of the particles measured at 64.8m downstream is recorded on the x-axis of the plot while the crystal orientation angle is on the y-axis. Six distinct regions of interest are visible: in region (1) the beam "sees" the crystal as an amorphous material and no peculiar effect can be observed. In region (2) channeling is effective at an angle of (165±2) µrad, in agreement with the value of the bending angle of the crystal. The measured fraction of incoming particles deflected by the crystal through channeling in region (2) is about 55%. Events in which the particle escapes from the channels along the crystal length (dechanneling), fill the region (3). At larger angles, channeling at the entry face of the crystal is no longer possible, but in region (4) the beam clearly appears to be deflected in a direction opposite to that of channeling. This is the region where volume reflection occurs. A Gaussian fit to the reflected beam distribution yields a deflection angle θ_{vr}=(13.9±0.2(statistical)±1.5 (systematic)) µrad, which is in agreement with the prediction of analytical calculation [5.10] (14.5 µrad) and of Monte Carlo simulation [5.6] 14.7 - 15.0 µrad.

The extension of region (4) along the *y*-axis is comparable to the bending angle of the crystal. Region (5) corresponds to the particles that are volume captured due to multiple scattering on the crystal nuclei and electrons. As the crystal orientation angle increases beyond the bending angle in region (6), the beam interacts with the crystal again as an amorphous material with similar features as in region (1). Analysis of the beam profile for two different crystal orientations, one in region (1) and one in region (4) (see Fig. 3.16), demonstrates that volume reflection does not appreciably alter the profile of the beam.

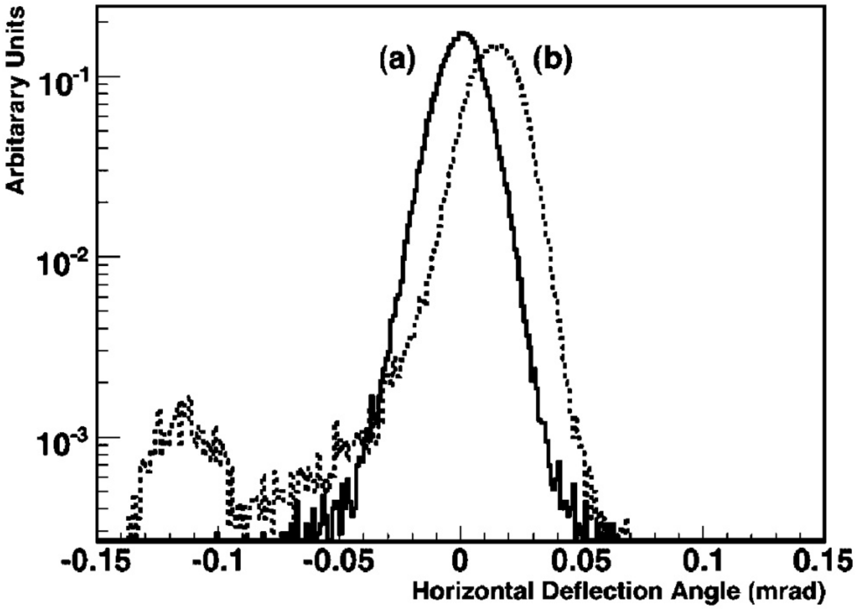

Figure 3.16. Beam profile for a crystal not aligned with the beam and b crystal aligned in VR condition

Volume reflection is a crucial finding for beam steering. In order to quantify this capability, an important parameter is the reflection efficiency, namely the fraction of particles being volume-reflected. A particle is considered as reflected when its angle with the incident beam axis is $\theta_{def}>\theta_{vr}-3\sigma_{vr}$, where σ_{vr} is the RMS deviation for the peak of the reflected beam. For strip crystal the volume reflection efficiency has been estimated to exceed 98%. This high efficiency is by far greater than the ~85% obtainable with channeling in single-pass mode. We also measured the volume reflection effect with a quasimosaic silicon crystal. This crystal had been bent along (111) crystallographic planes, its length and bend angle being equal to 0.84 mm and 72 μrad, respectively. Measured deflection angle of the volume reflected beam was about 13 μrad and the reflection efficiency close to the strip crystal case. A difference between the crystals agrees within the margin of experimental errors.

3.6 Volume reflection dependence on crystal bending radius

In order to study VR dependence on crystal bending radius a crystal of size 70x2x0.5 mm^3 realized by chemical anisotropic etching was bent at different bending radius.

The VR parameters, i.e. the mean deflection angle θ_{VR}, the rms deviation σ_{VR} and the efficiency ε_{VR} were measured as a function of the bending radius. It is shown in [5.11, 12] that in a bent crystal the distribution of the particle deflection angles due to VR is broadened if the centrifugal force F_c acting on the particles increases, which means that for particles of a given energy E a larger crystal curvature leads to a smaller θ_{VR} and a larger σ_{VR}. Such a change of the VR parameters becomes clear when the effective potential variation as a function of the crystal curvature is considered (Fig. 3.17). As already described, VR occurs near the turning points of quasi-channeled particles in the effective potential of a bent crystal, where the particles radial velocity changes its sign. For a small crystal curvature, that is $R>>R_c$, the turning points of all particles gather in a narrow region near the inner wall of a planar channel [Fig. 3.17a].

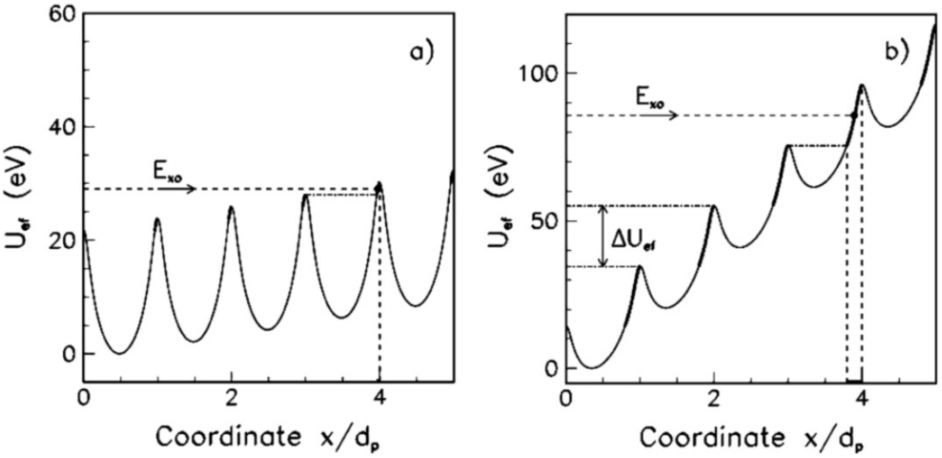

Figure 3. 17. The effective potentials for the (110) planes of a silicon crystal bent with a radius R=35.71 m a and 3.76 m b for 400 GeV/c protons. The coordinate x is measured in the direction opposite to the radial one; dp=1.92Å is the planar inner wall of a planar channel [Fig. 3.17a]. The strong channel width (distance between the two walls of each potential well) and $\Delta Ueff=(pv/r)d_p$ is the potential inclination along the channel. The trajectory of a particle being reflected with a turning point in the fourth channel is shown. The position of the corresponding reflecting plane is shown by a vertical dashed line at $x=4d_p$. The thicker lines show the turning point regions.

For larger crystal curvatures, the turning region of the effective potential increases. This decreases the electric field value at the lower boundary of the turning region and therefore, the average deflection angle due to VR becomes smaller. At the same time, the range of field values near the turning points gets larger and this increases the spread of the particles deflection angles.

Volume reflection efficiency is limited by volume capture (VC). The volume capture probability dependence on the crystal radius R is approximately linear ($P_{VC}(R)\approx R\theta_C/L_d$ [5.13, 14] due to a linear increase of the tangency region length with increasing R. Since VC limits the VR efficiency, that is $P_{VR}(R)=1-P_{VC}(R)$, the VC dependence on R translates in a linear decrease of the VR efficiency with increasing R.

A Gaussian fit to the deflection angle distributions gives the mean θ_{VR} and its rms deviation. As previously, the value of $\theta_{VR}+3\sigma_{VR}$ determines the boundary between the volume-reflected portions of the beam and the non reflected beam, which is due to the volume capture of protons, and allows compute the VR inefficiency ε. The beam broadening is calculated as $\bar{\sigma}_{VR}=\sqrt{\sigma_{VR}-\sigma_{am}}$ where σ_{am} is the beam spread in the crystal amorphous alignment and σ_{VR} is the observed spreading, which is due to the VR process and to spread caused by the fact that, apart from the region of VR, the beam sees the crystal as amorphous. Table I summarizes the experimental results.

TABLE I. VR parameters for the different crystal bend radii R.

R(m)	θVR(μrad)	$\bar{\sigma}_{VR}$ (μrad)	ε(%)
2.41	5.43±0.10±0.64	6.39±0.08±0.47	1.56±0.11±0.1
3.76	8.68±0.14±1.19	4.50±0.12±0.42	2.07±0.21±0.8
4.49	9.89±0.09±0.68	3.80±0.08±0.33	2.64±0.16±0.4
8.7	12.48±0.08±0.45	1.76±0.07±0.17	3.98±0.19±0.2
20.85	13.90±0.16±0.49	1.68±0.15±0.22	5.52±0.31±0.9
38.31	14.08±0.11±0.41	1.10±0.11±0.09	6.22±0.38±1.5

Figure 3.10 shows the experimental and theoretical [5.10, 15] dependencies of θ_{VR} and σ_{VR} on the crystal curvature (R^{-1}) and the dependence of ε on the crystal bend radius R. In the measured range the mean deflection angle θ_{VR} decreases approximately linearly as the curvature increases. This is similar to the dependence of the critical channeling angle in case of moderate crystal bending [5.16, 17] ($\theta_c(R) \sim 1 - R_c/R$). As in the case of θ_c whose decrease is caused by the decrease of the potential well depth, the decrease of θ_{VR} occurs because the effective potential tends to be a straight line.

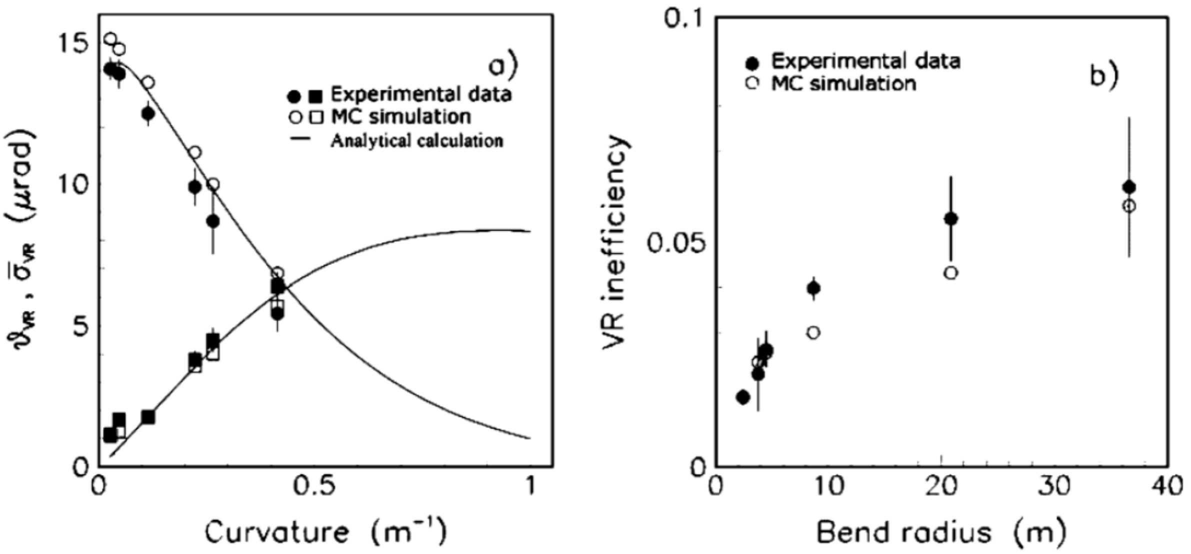

Figure 3.18. The dependencies of the VR parameters on the crystal curvature and the bending radius R: (a) the deflection angle θ_{VR} (dots) and its rms deviation due to the potential scattering σVR (squares), (b) the VR inefficiency.

On the contrary, the rms deviation of θ_{VR} increases approximately linearly within the measured range of crystal curvatures. This increase is caused by the increase in the spread of the electric field strength near the turning points in the effective potential. According to experimental and theoretical estimations θ_{VR} attains its maximum value at a bend radius of about 1.1 m (approximately 1.6 R_C), and decreases with decreasing R because the effective potential becomes closer to a straight line. The reflection inefficiency ε increases with R since the VC probability increases. The simulation results show an almost linear dependence as expected by the theoretical estimation for the VC probability.

Taking into account the observed dependences of the VR parameters on R, an optimal bend radius for a short silicon crystal for beam deflection due to VR is found to be about $10R_C$. This value maximizes the product of the deflection angle times the reflection efficiency times the angular acceptance. The increase of R gives larger θ_{VR} but decreases the efficiency and the angular acceptance. To obtain the same acceptance, the crystal length should be increased but this generates more particle losses in inelastic interactions with the crystal nuclei.

A strong potential scattering of particles for R close to R_C shows that such a crystal can be used as an effective scatterer. The thickness of the crystal scatterer can be reduced down to the wavelength of the particle oscillations in the planar channel (60 μm for 400 GeV protons and 250 μm for 7 TeV protons). In this way the inelastic losses of particles in the scatterer can be minimized.

3.7 Multiple volume reflections

In order to increase the deflection angle achieved by volume reflection, two approaches have been followed. The first one is based on the excitation of VR in a series of crystals (see Fig. 3.19). The second approach relies on excitation of multiple volume reflections in one crystal, as theoretically speculated in chapter 1.

3.7.1 Multiple volume reflections in QM-like crystals

After a preliminary observation of VR from a sequence of two quasi mosaic crystals [5.18], two types of multi-crystal deflectors were developed for this experiment to accommodate either five quasimosaic or fourteen silicon strips.

The quasi-mosaic deflector made use of five crystal plates of 14x10x0.65 mm^3 with (111) atomic planes disposed parallel to the 14x0.65 mm^2 face. Each crystal plate was bent on a cylinder with a radius of curvature of about 2.7 m by clamping between the concave and convex parts of the bending device to provide a about 110 μrad quasi-mosaic bend of the (111) planes. On the edge of the bending device, in the area where the proton beam should pass through the crystal, a special opening with a size of 5x3 mm^2, or 6x1 mm^2 for different samples was foreseen. Bending devices with clamped crystals were mounted on a support made from a metal plate with narrow deep cuts to provide the fine angular alignment of crystals using piezoelectric elements put in these cuts.

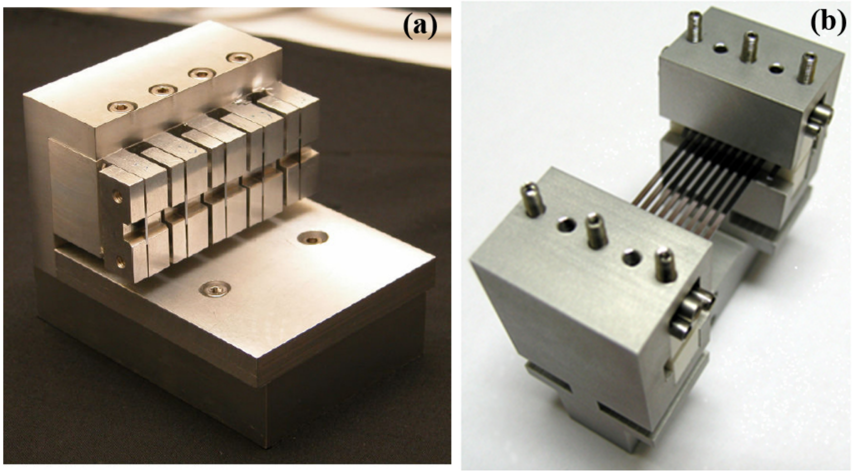

Figure 3. 19. On the left a multi quasi mosaic assembly, on the right a multi-strip crystal

Before installation of the crystals on the beam they were reciprocally aligned within about 2 mrad with a laser system, then the angular position of each crystals was finely adjusted on the proton beam by using piezoelectric driven elements.

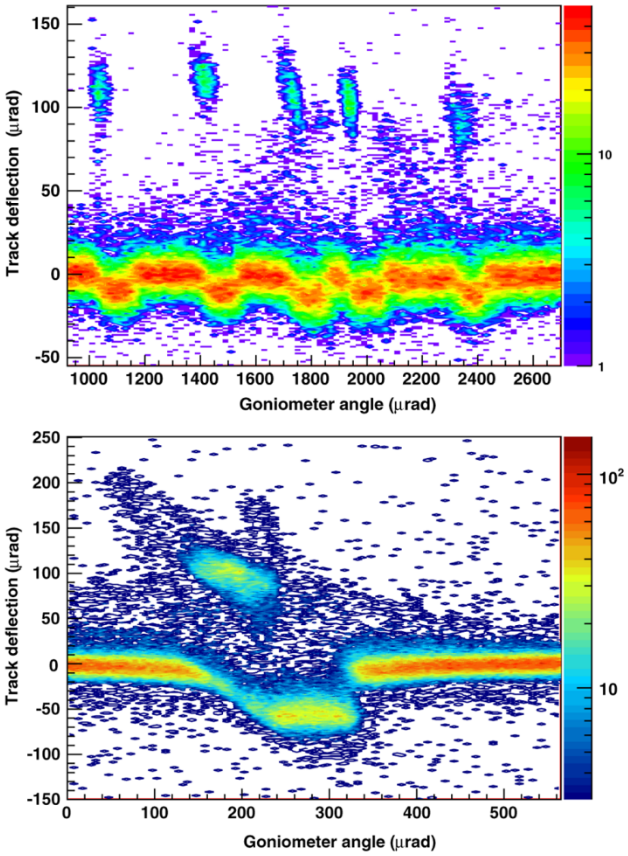

Figure 3.20. Beam intensity distributions observed in the angular scans performed before (top) and after (bottom) the relative alignment of the five crystals. The beam intensity is reported as a function of the track deflection angle (vertical axis)

Beam intensity distribution as a function of the track deflection angle (vertical axis) in different goniometer angular positions (horizontal axis) is shown in Fig. 3.20 as measured in the angular scans performed before (top) and after (bottom) the relative alignment of the five crystals. Before crystal alignment, the deflection effects arising from the proton interactions separately in each crystal are visible as peculiar structures in the track deflection angle distribution corresponding to five distinct goniometer orientation intervals, the crystal are aligned within 1.4 mrad. The channeling peak, at positive deflection angles of about 100μrad, and the VR region, for negative deflection angles of about 10μrad, is found in each interval for increasing values of the goniometer angle. A Gaussian function has been used to describe the deflection angle distributions for volume reflected tracks in each crystal. In Table II the mean deflection angles measured for the volume reflection in the five crystals are reported, as well as the corresponding goniometer angular ranges.

TABLE II. Mean deflection angles for volume reflected (θ_{VR}) protons as measured with the five not aligned crystals. The corresponding goniometer position intervals (α_{VR}) are also reported.

α_{VR}	θ_{VR} (μrad)
$\alpha \in [1080,1100]$	9.6±0.3
$\alpha \in [1480,1500]$	9.6±0.3
$\alpha \in [1780,1800]$	12.5±0.4
$\alpha \in [2020,2040]$	10.2±0.4
$\alpha \in [2380,2400]$	11.8±0.4

Deflection angle and efficiency for the fivefold volume reflection have been measured. In Fig. 3.20 (bottom) a net superposition of the volume reflection effect from the five crystals is clearly visible, corresponding to a track deflection angle of ~50 μrad towards negative values. Conversely, deflection towards positive angles due to channeling is still of the same magnitude as in the unaligned crystals run, but the channeling peaks due to single crystals are merged for contiguous goniometer positions.

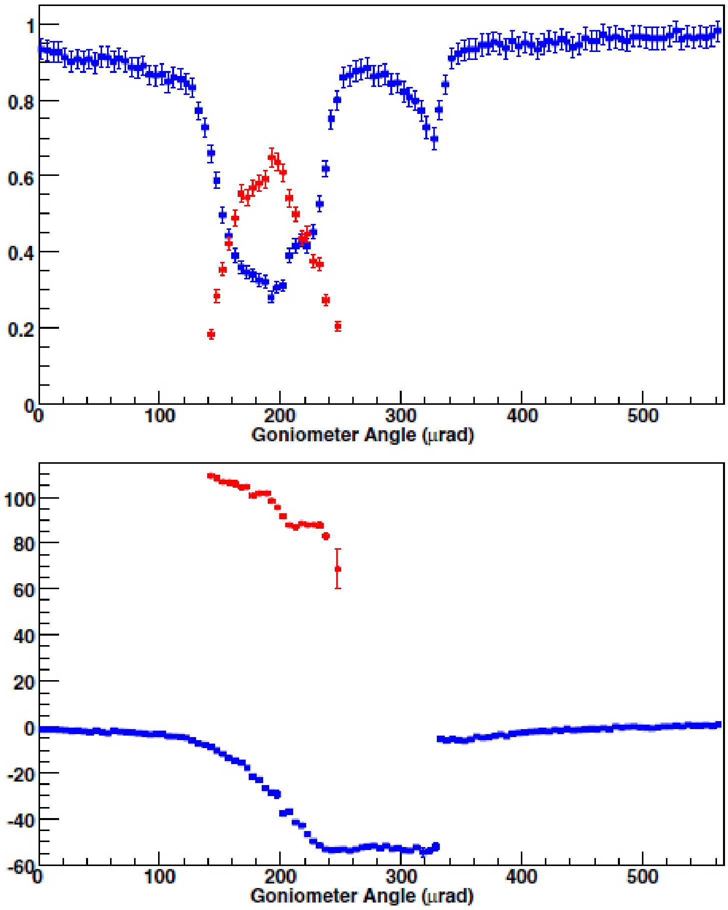

Figure 3.21. Beam intensity distributions observed in the angular scans performed before (top) and after (bottom) the relative alignment of the five crystals. The beam intensity is reported as a function of the track deflection angle (vertical axis) in different goniometer angular positions (horizontal axis)

A Gaussian fit to the track deflection angle distributions was used to estimate the mean deflection angle (θ) and its dispersion (σ) for channeled and volume-reflected beam fractions as well as for the undeflected beam. The ratio between the number of events within $\pm 3\sigma$ around the fitted peak value and the total number of collected events at each goniometer orientation defines the corresponding raw efficiency ε_R for the beam component under study. Volume reflection efficiency is then obtained as $\varepsilon^{VR} = \varepsilon_R^{VR} = \varepsilon_R^{U}$ where $\varepsilon_R^{U} = 96 \pm 0.6\%$ represent raw efficiency in absence of deflection effects. The systematic uncertainties on the deflection angle are mainly related to the single Gaussian model used to fit the track deflection angle distributions. The sum of several Gaussian functions has been used to describe more in detail the deflection peaks but no systematic effect in the measured deflection angle has been found within the statistical accuracy. The systematic uncertainty on the efficiency measurement is mainly related to the criterion used to define the number of tracks associated to the fitted peak: multiple Gaussian fits and different widths of the association window were used to check the measurement stability and to estimate the systematic error in the efficiency value.

The results from the fit procedure are summarized in Fig. 3.21. The uppermost panel reports the raw efficiencies measured on channeled, volume reflected and unperturbed beam components as a function of the goniometer orientation. The corresponding fitted values of the mean deflection angle are shown in the bottom panel. The transition towards the channeling effect is observed at the beginning of the angular scan: tracks are nearly undeflected up to a goniometer orientation of about 140 μrad where a steep increase of the channeled beam component is observed. Two beam components can be distinguished in the subsequent steps of the angular scan: the channeled tracks, which dominate up to 230 μrad and the dechanneled beam fraction steadily deflected towards negative angles. The onset of volume reflection is observed at goniometer orientations where the channeling effect comes to its end: a mean deflection angle θ=52.96±0.14µrad is observed in a wide interval of the goniometer orientation ($245<\theta<315$ µrad) with VR efficiency greater than 80%. Measured deflection is consistent with the sequence of reflections in the five crystals as it can be estimated from the sum of the deflection angle values obtained for the single crystals ϑ_{1-5}=53.7±0.8 µrad. The maximal volume reflection efficiency, ε^{VR}=0.90±0.01±0.03 is recorded for $250<\theta<290$ µrad. The VR effect extinction appears for $315<\theta<340$ µrad: a unique Gaussian peak is used to describe the deflection angle distributions in the subsequent scan steps. In the very last part of the angular scan, $\theta>475$ µrad, no deflection effects are observed: only events collected at these crystal orientations are used to study the unperturbed beam properties and to determine the ε_R^U value.

Results obtained in this experiment was very encouraging and showed the possibility to largely increase the deflection obtainable by VR interaction using a series of crystals. Nevertheless, this required a complex alignment system based on piezo-electric elements, whose alignment required much beam time and a quite cumbersome holder.

With the aim to eliminate such inconveniences we developed a multi-strip crystal able to excite multiple volume reflections in a series of strip-crystals. Such system is self-aligning, i.e. it does not require any external intervention to properly align the strips, and is much less cumbersome

3.7.2 MVR in multistrip crystals

The MVR effect from a series of crystals has been observed also using multi-strip crystal. A crystal made of 14 strips 0.96 mm thin each was realized by anisotropic etching and bent to a bending angle α~276µrad using the holders described in chapter 2.

Fig 3.22 shows the angular scan of a multistrip crystal made of fourteen strips, twelve of which were aligned to build up MVR.

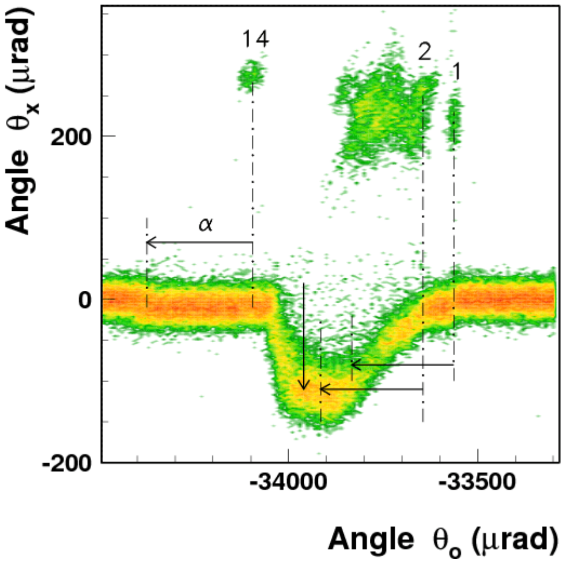

Figure 3.22 Angular scan obtained with a multistrip crystal made of 14 strip, 12 of which are correctly aligned.

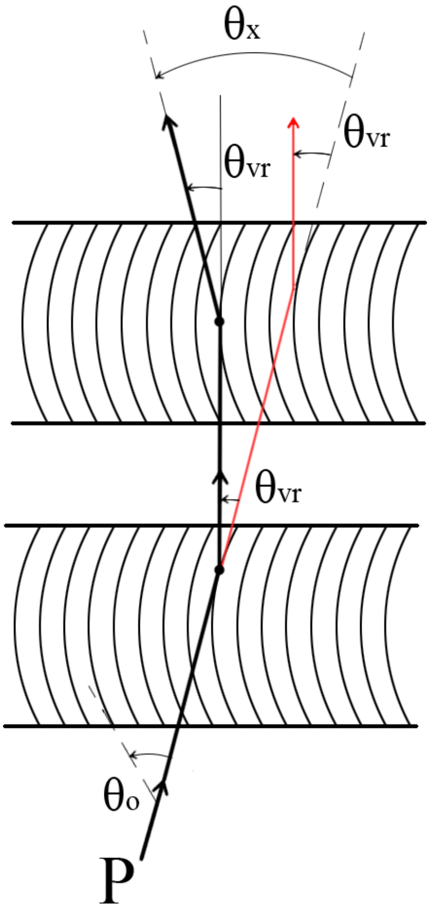

Spots numbered as 1,2 and 14 in the upper region of the picture pertain to the channeling peaks by the corresponding strips. Between them there is a “cloud” of channeling peaks for most of the strips. 12 strips were correctly aligned for MVR, and allow to achieve a record deflection angle of 122 μrad. Interaction with eleven strips allowed to largely increase, with respect to previous experiments, the deflection angle obtainable by MVR, arising at 110 μrad.

The horizontal arrows in Fig 3.22 highlight the angular regions for VR of the first two and the last crystals, while the vertical one identifies the position for which high statistics data is available. It was found that in this position only eleven strips were working coherently.

In that case, deflection efficiency is surprisingly as large as 88%. From the study of dependence of VR on the bending radius the 0.98 efficiency of each strip would result in $0.98^{11}=0.80$ efficiency of the array of 11 strips. The higher level of the experimental observation of MVR efficiency can be explained by considering that the particles subject to volume capture (in red in Fig 3.23), are channeled by an angle lower than the full crystal bending angle and are likely to undergo VR somewhere in one of the following crystals, i.e. they are recycled for MVR.

Fig. 3.24 shows the simulated beam profile resulting after the MVR process. The left peak corresponds to the MVR peak, the shadowed region indicates the particles that are subject to VR after VC in a previous crystal. From the figure it is clear that VC considerably contributes to build up the peak of deflected particles.

Figure 3.23 VR assisted by VC. (See the text for explanation).

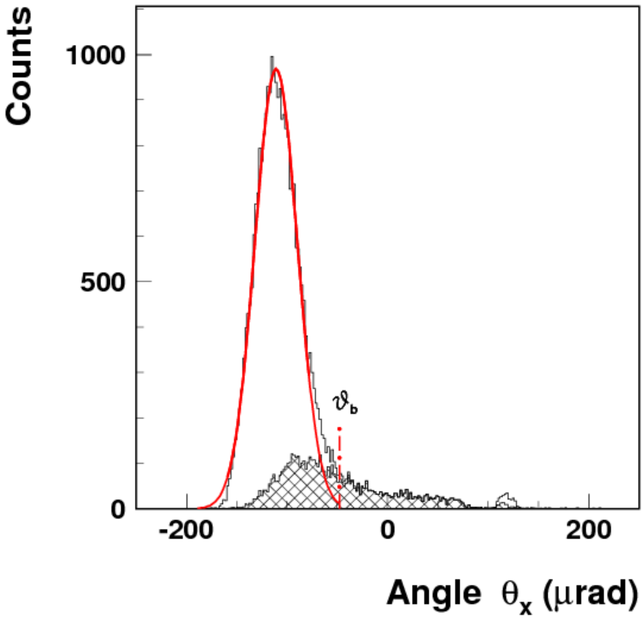

Figure 3.24 Simulation of MVR process in 11 aligned strips. The left peak corresponds to VR particles, to which contributes particles which are subject to VC in a first crystal, and deflected by VR in a subsequent crystal.

In summary, this experiment has highlighted that MVR can be a very powerful and efficient method to steer particle beams. VC, which is normally recognized to be a limiting factor for individual VR, assists in fact MVR, raising up the total deflection efficiency.

3.7.3 Multiple volume reflection in a single crystal

The description of the process of multiple volume reflection in a single crystal has been already provided in chapter 1. This phenomenon have been experimentally observed in the interaction of protons of 400 GeV energy with <111> axis of a specifically designed strip-like silicon crystal of size 70×4×0.5 mm^3. The strip crystal, with the largest faces parallel to the (110) planes and with the side faces parallel to the (111) planes, was fabricated by anisotropic etching of silicon as described in chapter 2. The proton beam entered parallel to the (110) planes. At 400 GeV the axial critical angle is 20.7 μrad, thus in order to satisfy condition (1.23), the crystal was bent at an angle of 350 μrad. Measured RMS deviations for the horizontal and vertical divergences of the beam were σ_x=(11±0.06) μrad and σ_y=(9.13±0.03) μrad, respectively. After alignment of the crystal axis with the particle beam with accuracy less than the axial critical angle, the crystal was rotated of 170 μrad in the horizontal direction, and 85 μrad in the vertical one, allowing the observation of multiple volume reflection in a single crystal.

Fig. 3.25a shows distribution reflection in the horizontal and vertical deflection angles of the proton beam after interaction with the crystal. Fig.3.25b shows the horizontal projection of the distribution. Gaussian fit of the peak on the right side gives the value θ_{mvr}=(66.53±0.27) μrad for the maximum deflection angle.

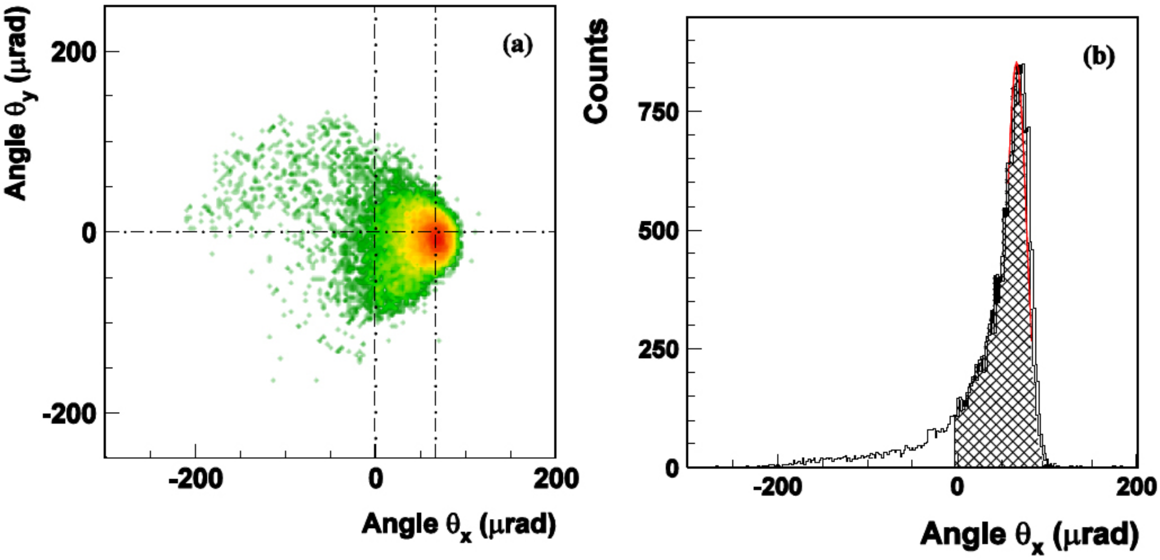

Figure 3.25. (a) Intensity distribution of the proton beam in the horizontal and vertical deflection angles acquired due to multiple volume reflections from different planes in one bent silicon crystal around the <111> axis. Maximum position is shown by dot-dashed line. (b) The horizontal projection of the distribution. The distribution part with θ_x>0 (about 84%) is hatched. Gaussian fit gives for the maximum position θ_{mvr}≈66.5 μrad.

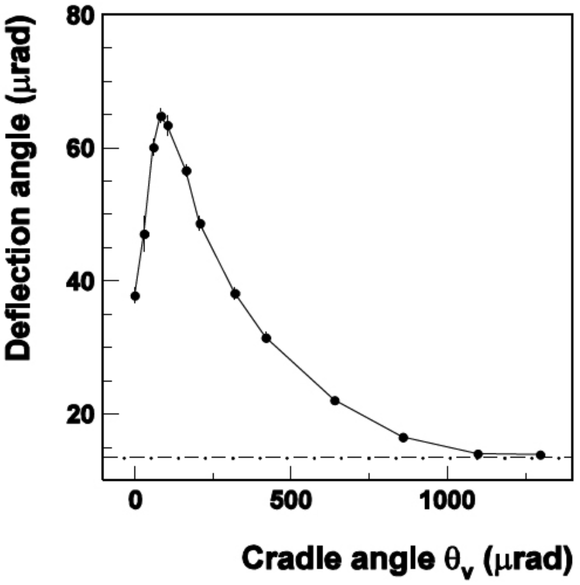

Figure 3.26. Dependence of the MVR deflection angle θmvr on the vertical (cradle) angle of the crystal orientation θ_v. Dot-dashed line shows the deflection angle for a single VR from the (110) vertical plane, $\theta_{vr}\approx 13.35$ μrad

Single volume reflection deflection angle, as measured at an angle 1.3 mrad from the axis was θ_{vr}=(13.35±0.17) μrad. The deflection angle obtained by proper alignment of the crystal with respect to the beam in the axial direction allows VR from skew planes, providing an enhancement of the deflection angle equal to four times the one obtainable without the interaction with them. The deflection efficiency to the side opposite to the crystal bend was $P_d(\theta_x>0)$=(83.86±0.26)%. The distribution tail to the bending side is due to volume capture of protons into the channeling regime, occurring as they cross the tangency areas with different crystal planes. A small shift of the maximum position in the vertical direction (see Fig.3.25a) can be explained by an incomplete compensation of the contributions from the symmetric skew planes, i.e. by a not perfect alignment with respect to the crystal axis.

In order to study the contribution to MVROC from the different skew planes we made a cradle scan varying the orientation of the crystal axis with respect to the beam. Changing the incidence angle, we selectively excluded some of the skew planes. Fig.3.26 shows the dependence of the MVROC deflection angle θ_{mvr} on the vertical (cradle) angle of the crystal orientation θ_v relative to the axial alignment. The deflection angle has a maximal value at the cradle angle $\theta_v=\theta_v^*$=85 μrad. At angles $\theta_v \ll \theta_v^*$, stable proton motion is no more stable and influenced by string potential, reducing VR angle. At angles $\theta_v \gg \theta_v^*$ a decreasing number of skew planes is involved in the MVROC, so the deflection angle decreases quickly. At an angle θ_v>1mrad none of the skew planes is involved in MVROC, the interaction between the crystal and the beam reduces to a single volume reflection.

By requiring an angular alignment in two directions, MVROC is experimentally a bit more difficult to achieve with respect to VR, though it leads to an increase by a factor ~5 of the particles deflection angle, i.e. a single crystals aligned in a way to excite MVROC plays the role of 5 crystals aligned in a way to excite VR. Such feature fully justifies the efforts required to reach the proper alignment conditions. Efficiency proved to be as high as 83%, and acceptance in both vertical and horizontal angles proved to be comparable to the acceptance of VR.

3.8 Discussion

The use of short bent crystals allowed to study and identify new mechanisms for beam steering and deflection. Such coherent effects of particle-to-crystal interaction offer innovative schemes for beam collimation in new generations of hadronic machines. Table III summarize some advantages and disadvantages for each interaction scheme.

Scheme	Advantages	Disadvantages
PC	• Control of deflection angle through the crystal bending angle • Large deflection angle • High efficiency	• Low angular acceptance without control
AC	• Control of deflection angle through the crystal bending angle • Large deflection angle • Efficiency even higher than for PC	• Need for two angular alignments
VR	• High angular acceptance • Efficiency close to 100%	• Low deflection angle • Deflection angle determined by beam energy
MVR	• High efficiency • High deflection angle	• Stringent requirements on the crystals alignment • Non negligible amount of material involved in the interaction.
MVROC	• High efficiency • High deflection angle	• Need for two angular alignments

Basing on the characteristics of studied mechanisms and on technical aspects, the UA9 collaboration, which will be described in the last chapter of this thesis, is currently investigating the halo collimation of the circulating in the SPS.

References

[5.1] L. Celano *et al.*, Nucl. Instr. and Meth. A. **381** 49 (1996)
[5.2] A. Baurichter *et al.*, Nucl. Instr. and Meth. B. **119** 172 (1996)
[5.3] A. M. Taratin, Phys. Part. Nucl. **29** 437 (1998)
[5.4] J. F. Bak *et al.*, Nucl. Phys. B. **242** 1 (1984)
[5.5] A. A. Greenenko and Shul'ga N. F., Phys. Lett. B. **454** 161 (1999)
[5.6] A. M. Taratin and Vorobiev S. A., Phys. Lett. A. **115** 401 (1986)
[5.7] Y. M. Ivanov, JETP Lett. **84** 372 (2006)
[5.8] Y. M. Ivanov *et al.*, Phys. Rev. Lett. **97** 144801 (2006)
[5.9] Scandale *et al.*, Phys. Rev. Lett. **98** 154801 (2007)
[5.10] V. A. Maisheev, Phys. Rev. ST Accel. Beams. **10** 084701 (2007)
[5.11] A. M. Taratin and Vorobiev S. A., Nucl. Instrum. Methods Phys. Res., Sect. B. **512** 26 (1987)
[5.12] Y. M. Ivanov *et al.*, Phys. Rev. Lett. **97** 144801 (2006)
[5.13] Y. A. Chesnokov *et al.*, Nucl. Instrum. Methods Phys. Res. B. **69** 247 (1992)
[5.14] V. M. Biryukov, Nucl. Instrum. Meth. Phys. Res. B. **234** 23 (2005)
[5.15] A. M. Taratin and Vorobiev S. A., Zh. Theor. Fiz. **55** 598 (1985)
[5.16] V. V. Kaplin and Vorobiev S. A., Phys. Lett. A **67** 135 (1978)
[5.17] E. N. Tsyganov, Fermilab Preprint TM-682, TM-684 Batavia (1976)

Chapter 4

Coherent interactions between negatively charged particle beams and crystals

Negatively charged particles coherently interacting with crystals are subject to attractive potential, as a result the probability of close collisions with the crystal atoms is higher than for their positive counterparts. Thereby, dechanneling becomes stronger and the use of short crystals is demanded.

Up to now, knowledge of coherent interactions between negatively charged particle beams and crystals is not as deep as for positive particles. For example, up to now, in the attempt of steering high energy beams, only a broadening of the angular distributions towards the crystal bend side has been observed [4.2-3].

Thanks to availability of short quasi-mosaic and strip crystals, the H8-RD22 and UA9 collaborations investigated beam steering and radiation emission in the interactions between negatively charged particle beams of 150 GeV energy and crystals. Experiments have been carried out at the external line H4 at CERN with the setup described in chapter 3.

4.1. Planar channeling and VR of negative particles

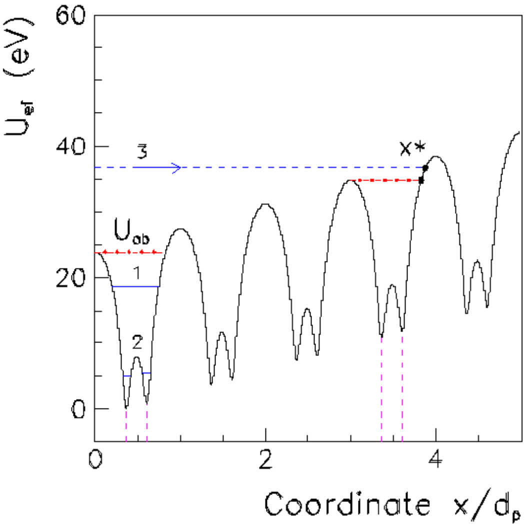

Figure 4.1 The effective potential for the (111) planes of a silicon crystal bent with the radius R=12.92m for 150 GeV/c π-mesons. The coordinate x is measured in the direction opposite to the radial one, d_p=3.136 Å is the channel width. U_{ob}=23.88 eV is the depth of the planar potential well. The lines 1-3 show the particle states: (1) channeling states bounded with one plane of the pair and (2) with both planes of the pair; (3) the above barrier states, which lead to volume reflection. x* is the turn point of the particle (3) in the potential. The vertical dashed lines show the plane positions in the first and forth potential wells (they are the same along the whole crystal thickness).

The dechanneling length for negative particles is much shorter than for positive ones [4.1]. For this reason up to now the deflection of negative particles by bent crystals has not been observed in experiments with long crystals [4.2-3].

Fig.4.1 shows the effective potential in a quasimosaic bent crystal for 150 GeV/c π^- and the different states realized for particles. The transverse energy of a particle in state 1 is smaller than the potential barrier between the pair planes. In this channeling state the particle moves along the trajectory winding on one of the pair plane. The particle transverse energy for state 2 is smaller than the potential well depth of the plane pair, $E_{xo}<U_{ob}$ (U_{ob}=23.88 eV and the corresponding critical angle θ_{cb}=17.84 μrad). In this channeling state the particle trajectory oscillates between both the

planes of the pair. For the above-barrier state 3 with $E_{xo}>U_{ob}$ the particle comes to the turn point $x*$ in the effective potential where either the volume reflection or volume capture occurs.

The divergence of the beam incident on to the crystal measured with the detector telescope was characterized by the RMS deviations σ_x=(34.4±0.06) μrad and σ_y=(28.2±0.04) μrad in the horizontal and vertical planes, respectively.

Fig.4.2 shows the intensity distribution of the beam after crossing the quasimosaic crystal in the deflection angles of particles (*Y*-axis) at the different angular positions of the goniometer (*X*-axis). Only the particles hitting the crystal with a horizontal angle $|\theta_{xo}| < 10$ μrad were selected.

The picture is very similar to the one obtained in the experiment with 400 GeV/c protons. Therefore, the different areas in the figure are marked in the same way. Areas (1) and (6) are the ones where the crystal scatters particles as an amorphous material. Moving from the right to the left of the figure we pass first the crystal orientations where a considerable fraction of the incident beam is captured into the bound states with the (111) planes and deflected by the crystal bend angle (channeled particles) (2). Area (3) shows the fraction of particles dechanneled during the passage through the crystal. The wider area (4), whose width is determined by the crystal bend angle, is the volume reflection area. Area (5) shows the particle fraction captured into the bound states with the bent planes in a tangency area due to multiple scattering on the atomic nuclei (volume capture) and therefore undergo a smaller angular deflection.

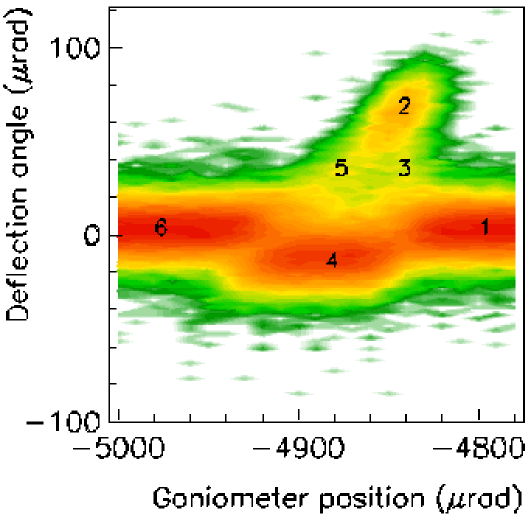

Figure 4.2 The intensity distribution of deflected π- beam after crossing the bent silicon crystal as function of the crystal angular positions with respect to the beam. The following areas are indicated: (1) and (6) amorphous scattering, (2) deflection due to channeling, (3) dechanneling, (4) volume reflection, (5) deflection of volume captured particles. Only particles hitting the crystal with a horizontal angle $|\theta_{xo}| < 10$ μrad were selected.

Fig. 4.3a shows the distribution of particle deflection angles for the crystal orientation optimal for channeling. The right peak was generated by particles deflected by the crystal in channeling states. Particles, which were not captured into the channeling states and were deflected to the side opposite to the crystal bend due to volume reflection, generate the left peak. The beam fraction between the two peaks outside the fits determines the dechanneled fraction of the beam (about 14%). The Gaussian fit of the channeled fraction gives the mean deflection angle θ_d=(63.24 ± 0.24) μrad and the RMS deviation σ_d=(10.16±0.19) μrad. In the assumption of a uniform bend, the crystal bend radius, which corresponds to this deflection angle, is R=12.92 m. The deflection efficiency determined by the beam fraction under the fit (hatched area) is P_d=(30.24±0.38)%.

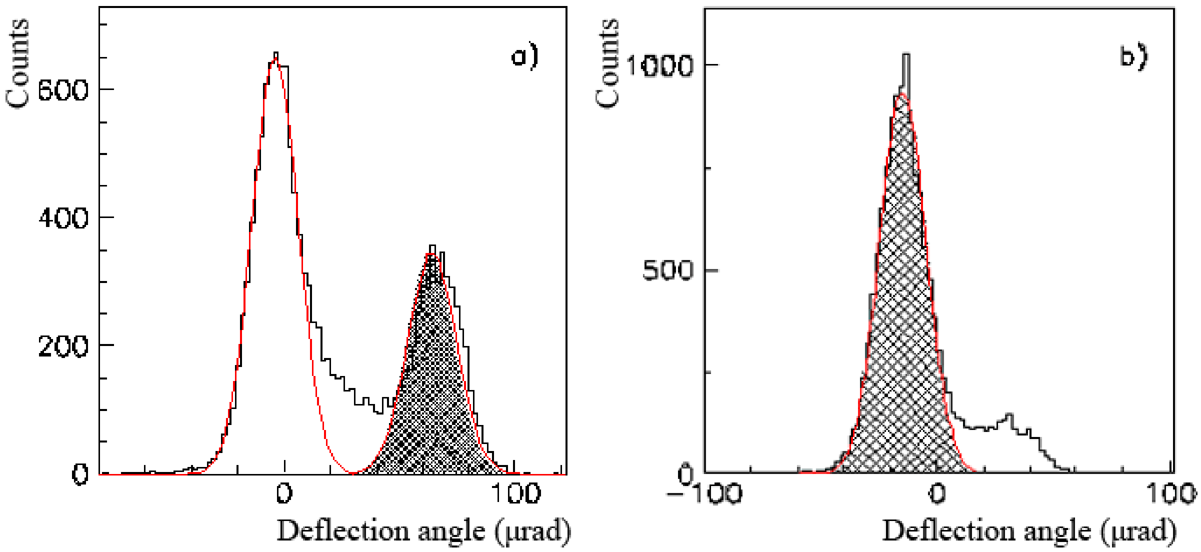

Figure 4.3 The deflection angle distribution of π- mesons crossed the (111) bent silicon crystal (QM2) for the crystal orientations optimal for channeling (a) and volume reflection (b). The curves show the Gaussian fits of the peaks. The hatched areas show the deflected fractions of the beam due to channeling (a) and VR (b).

Fig. 4.3b shows the distribution of the deflection angles of particles for the crystal orientation in the middle of the VR area. The Gaussian fit gives the peak position, the VR deflection angle, θ_{vr}=(-14.64±0.12) μrad and its RMS deviation σ_{vr}=(10.06±0.11) μrad. The VR deflection angle is about $0.8\theta_c$. A considerable distribution tail with $\theta>0$ is caused by particles, which were volume captured and then partly dechanneled.

As usual, VR efficiency is determined as the beam fraction under the Gaussian fit with angles $\theta<\theta_{vr}+3\sigma_{vr}$. This gives P_{vr}=(82.74±0.28)%. The large distribution tail on the bend side indicates that the probability of volume capture into the channeling states is considerably higher for negative particles because they undergo strong multiple scattering on the atomic nuclei passing the potential well center where they have large transverse velocities. Simulation shows that about 50% of particles are volume captured in the considered case. However, most of them is quickly dechanneled because of the same strong multiple scattering. Nevertheless, VR inefficiency due to volume capture approaches 20% for 150 GeV/c π^-mesons, which is about one order of magnitude higher than for 400 GeV/c protons.

Fig. 4.4 shows the distribution of the deflection angles of 150 GeV/c π^- for the strip silicon crystal when the optimal orientation for channeling occurs. The crystal, prepared by anisotropic etching techniques had length along the beam of 0.98 mm and was bent along the (110) planes, which are equidistant.

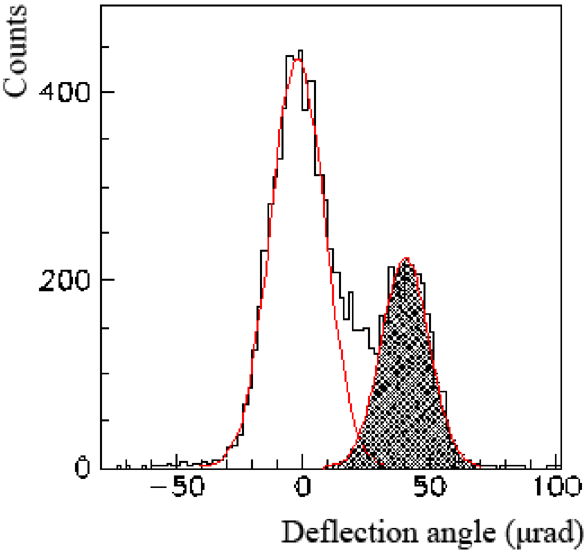

Figure 4. 4 The deflection angle distribution of π- mesons crossed the (110) bent silicon crystal (ST10) for the crystal orientations optimal for channeling. Only particles hitting the crystal with a horizontal angle |θxo| < 5 μrad were selected.

For this case the potential well depth U_{ob}=22.08 eV and the critical angle θ_{cb}=17.15 μrad. The Gaussian fits for channeled and reflected fractions are overlapped here due to a smaller bending angle of the crystal. The fit of the channeled fraction gives the mean deflection angle θ_d=(40.54±0.36) μrad and the RMS deviation σ_d=(9.41±0.29) μrad. The crystal bending radius, which corresponds to this deflection angle, is R=22.79 m. The deflection efficiency defined as the beam fraction under the fit (hatched area) is P_d=(28.81±0.47)%.

From the distribution of the particle deflection angles for the VR crystal orientation the VR deflection angle for the ST10 crystal was determined to be θ_{vr}=(11.53±0.23) μrad. For negative particles, in contrast to the positive ones, the VR deflection angle is smaller for the (110) planes than for the (111) ones, $\theta_{vr}=0.66\theta_c$. The same definition as used above gives for the VR efficiency P_{vr}=(76.75±0.32)%. The VR efficiency is smaller than for the quasimosaic crystal because the volume capture probability of particles is higher due to the larger bending radius.

The parameter values for channeling and volume reflection of π^- mesons obtained for the quasimosaic and strip crystals in the experiment and in simulations are listed in Table I.

Table I. Channeling and VR parameters for 150 GeV/c π^- in (111) and (110) Si

	Crystal	θ_c (μrad)	R (m)	θ_{vr} (μrad)	P_{vr} (%)	P_d (%)
Quasimosaic , (111) planes	Experiment		12.29±0.09	14.64±0.12	82.74±0.28	30.24±0.38
	Simulation	18.34		16.6±0.07	78±0.13	30.11±0.15
	Theory			14.28		
Strip, (110) planes	Experiment		22.79±0.22	11.53±0.23	76.75±0.32	28.81±0.47
	Simulation	17.39		12.84±0.11	74.77±0.14	28.67±0.14
	Theory			11.81		

The agreement is rather good. However, the values of the VR deflection angles obtained in the simulation using the Molier approximation of the atomic potential are 10-15% larger than the measured ones, which is similar to what we observed with 400 GeV/c protons. The angle values calculated using the explicit expression [4.4] and the atomic potential obtained through the experimental X-ray scattering factors are closer to the measured values (see Table I).

Our experimental results have shown that, despite the attractive potential to which negatively charged particles are subject, they can be deflected by means of planar channeling thanks to the existence of bound states. Besides, they have shown that volume reflection in bent crystals occurs also for negative particles in spite of the attractive character of the forces acting between the particles and the crystal planes.

4.2. Deflection of negative particles by axial channeling

The ST9 strip crystal, crystal used to study VR and planar channeling of negative particles was used also to study axial deflection of a 150 GeV/c π^- beam. After reaching the planar channeling alignment the crystal was rotated in order to align the crystal axis to the particles beam as already done in the axial deflection of protons. Fig. 4.5 shows the beam intensity distribution in the deflection angles of particles in the horizontal θ_x and vertical θ_y directions for the different orientation angles θ_h (see fig 3.12) of the <111> crystal axis with respect to the beam direction. Exploiting the tracking capabilities of the telescope detector system only the particles impinging on the crystal axis within the angles θ_x and θ_y satisfying the condition $(\theta_{x0}^2+\theta_{y0}^2)<10$ µrad were selected.

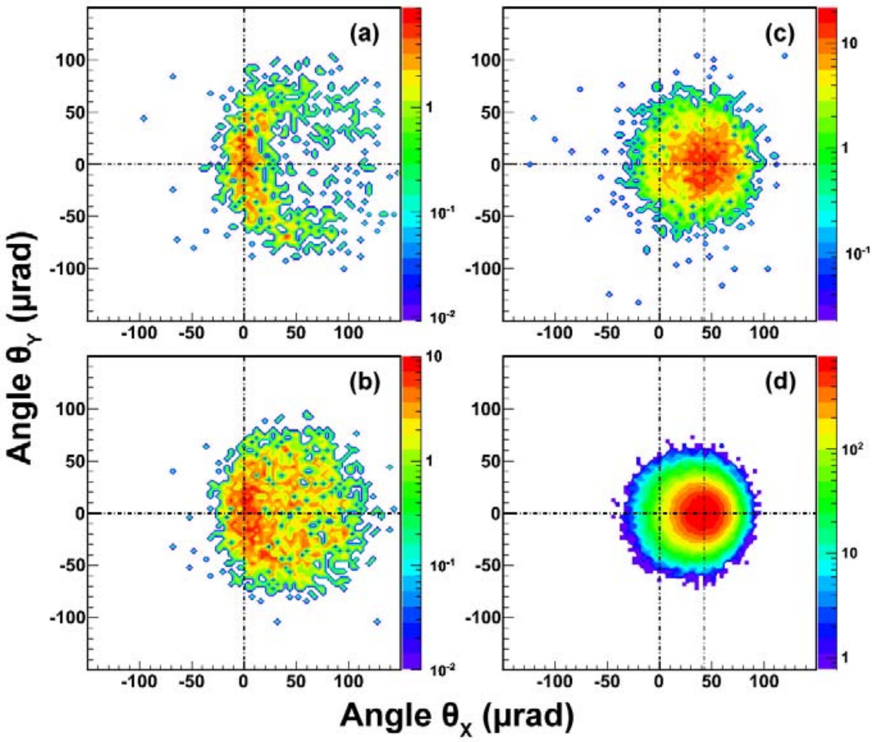

Figure 4.5 Beam intensity distribution in horizontal θx and vertical θy directions realized with axial channeling deflection for different orientation angles θh of the <111> crystal axis with respect to the beam: (a) θ_h=−40 µrad, (b) θ_h=−20 µrad and (c) θ_h=0

When the crystal is not aligned with the beam, particles undergo ordinary Coulomb multiple scattering as in an amorphous substance and the beam is not deflected. When the crystal axis becomes close to the beam direction particles motion is determined by the averaged potential of atomic strings. Particles undergo multiple scattering by the atomic strings, as a result the transverse momentums of particles is partly randomized. At misalignment angles with respect to the crystal axis comparable to the axial critical angle, for example θ_h=-40 µrad, such interaction leads to a shape of the deflected beam resembling an arc, whose radius is determined by the particle angles to the axis direction at the crystal entrance $|\theta_v|$ and exit $|\theta_v|+\alpha$. For the orientation angle θ_v=-20 µrad (b), the distribution shape becomes close to a circle, which is shifted to the bending side. However, the maximum of the beam intensity continues to be near the incident beam direction. At nearly perfect alignment, θ_v=0 (c), the whole beam is deflected of the quantity corresponding to the bending angle. Differently from the axial deflection of positive particles, for negative ones there is no leakage of particles into skew planar channels intersecting the <111> axis because the planar motion of axially channeled negative particles having would be not stable. After interaction with the crystal the beam is considerably broadened, this is due to the multiple scattering of particles by the atomic strings, which leads to the randomization of their transverse momentum and to strong incoherent multiple scattering on the atomic nuclei. The beam deflection efficiency toward one side with respect to the initial direction largely exceed the efficiency in planar mode, we have in fact $P(\theta_x>0)$=(90.6±0.5)%. Fig. 4.5d shows the two-dimensional intensity distribution of the beam traversing the crystal at a perfect alignment, which was obtained by simulation for the experimental conditions. The model of atomic-string lattice [4.5] with the atomic potential and electron density obtained in the Doyle–Turner approximation for the atomic scattering factors was used for simulation.

Fig. 4.6 shows the horizontal projection of the two-dimensional distribution for nearly perfect alignment as in Fig. 4.5c. The position in the maxium of the distribution corresponds to a crystal bend angle, α=43 µrad and has width FWHM equals to (55±2) µrad.

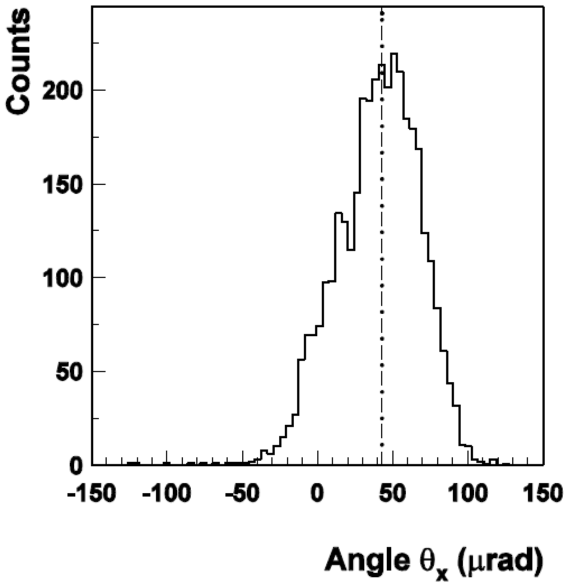

Figure 4.6 Horizontal projection of the beam intensity distribution shown in Fig. 1(c). The dotted line shows the crystal bend angle value α = 43 µrad.

The observed high level for deflection efficiency is partially due to the fact that the particles leaving the channel are readily rechanneled due to strong scattering on the atomic nuclei.

Fig. 4.7 shows the simulated dependence on the penetration depth into the crystal of the particles fraction in the bound states to the atomic strings, i.e. the particles fraction with transverse energies $E_x<U(R_s)$, where $U(R_s)$=99.4 eV is the potential value at the distance

equal to the string radius R_s (half the distance between the strings).

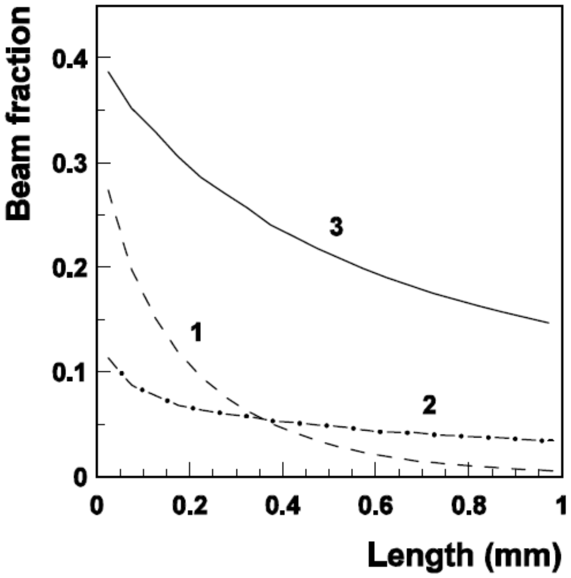

Figure 4.7 Fraction of particles in the bound states with the <111> atomic strings as a function of the penetration depth into the crystal (curve 3). Curve 1 is for the hyperchanneled fraction. Curve 2 is for the fraction recaptured into the bound states. The dependencies were obtained by simulation for the perfect alignment of the <111> axis with the beam.

Capture efficiency of particles into bound states for the experimental conditions is about 42%. However, the particles readily leave the bound states due to strong multiple scattering on the atomic nuclei. The contribution of hyperchanneled particles, which have crossed the whole crystal length in bound states is about 5.5% (see curve 1). However, dechanneled particles can easily be recaptured into the bound states thanks to incoherent multiple scattering. The fraction of particles recaptured in a certain crystal thickness is shown by the curve 2. The recapture process occurs along the whole crystal length. The total number of particles in the bound states with the atomic strings increases due to the recapture (the curve 3). The beam fraction deflected at the bend angle in the bound states is about 15%. Fig. 4 shows the trajectory of one of the particles, which underwent a few recaptures while crossing the crystal. The particle entered in the crystal in correspondence of the blue spot and captured in bound motion by a first atomic string. After a short path in the crystal the particle leaves the bound state, but due to scattering it is recaptured in bound state from a second string. The process of dechanneling and recapture in bound states happens again and the

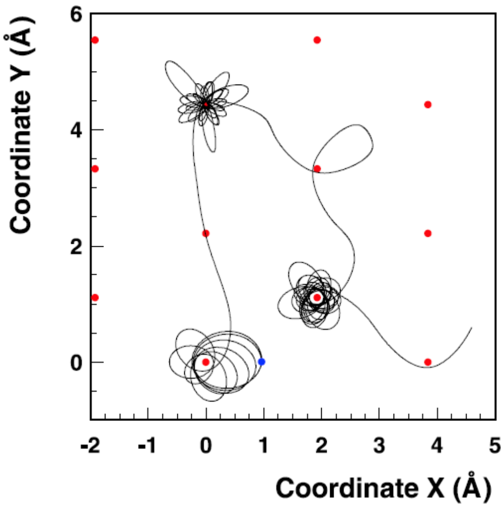

Figure 4.8 **Trajectory in the transverse space calculated for a particle captured into the bound state with the atomic string located at (X, Y) = (0, 0) at the crystal entrance and then two times was recaptured by the neighboring atomic strings. The bound states are seen by the precessing elliptical orbits. Red dots indicate the <111> axes positions and the blue one — the position of the entrance point of the particle.**

particle is captured by a third string.

Our experimental results have shown a high-efficient deflection of ultrarelativistic negative particles by means of axial channeling. The deflection mainly occurs due to doughnut scattering of particles by the atomic strings. Besides, it was shown by simulation that strong incoherent multiple scattering of particles on the atomic nuclei causes not only fast dechanneling but also a high probability of the reverse capture of particles into the bound states with the atomic strings, such mechanism leads to a high deflection efficiency.

4.3. Emission of radiation in the VR process

While several papers (see [4.6] and literature therein) has dealt with coherent radiation emitted by particles (in particular by electrons and positrons) in the channeling regime in not bent crystals, emission of radiation arising from interaction between charged particles and bent crystals (both in channeling and VR mode) is still not completely understood, some preliminary results obtained at the CERN Super Proton Synchrotron (SPS) with 180 GeV/c volume-reflected electrons and positrons will be described in the following.

4.3.1 Radiation from bent crystals

In a recent paper [4.7] the radiation by positrons and electrons was considered in the volume-reflection case. The theoretical explanation of this process is based on the analytical description of volume reflection [4.4] and on the equations derived with the quasiclassical operator method [4.8], where the probabilities of QED processes may be expressed by classical trajectories of charged particles in electric fields.

The radiation emitted by a relativistic particle can be described [4.8] by parameter $\rho = 2\gamma^2 < v_t^2 - v_m^2 > / c^2$, where γ is the particle Lorentz factor, $(v_t^2 - v_m^2)$ is the squared mean deviation of the transverse velocity from its mean value v_m, and c is the speed of light. If $\rho << 1$, the radiation intensity is the result of interference over a large part of the particle trajectory and depends on the peculiarities of the particle motion. If $\rho > 1$, the particle radiates during a small part of the trajectory (its motion direction does not change with the angle $1/\gamma$) and the contributions from far parts can be neglected. The case $\rho \sim 1$ is an intermediate one.

In straight crystals, the first case ($\rho << 1$) occurs when the particle planar angle θ is much larger than θ_b, the characteristic angle defined as $\theta_b = U/mc^2$ (m is the particle mass and U is the planar potential barrier): this type of radiation is known as coherent bremsstrahlung. The opposite case ($\rho > 1$) corresponds to synchrotron-like radiation and occurs when $\theta << \theta_b$. It is important to note that in a thin crystal a particle preserve the radiation type during its motion.

In a bent crystal, the planar angle θ changes during the particle motion; if volume reflection occurs, the radiation type during the particle motion is also modified. In other words, far from the reflection point, $\rho << 1$ and the radiation is due to coherent bremsstrahlung [4.9]. Approaching the reflection point, the ρ parameter increases: if the bending radius is significantly greater than the channeling critical one [4.10], the mean volume reflection angle is $\theta_{\mathrm{VR}} \approx \sqrt{2}\vartheta_{ch}$ for positrons and $\theta_{\mathrm{VR}} \approx \vartheta_{ch}$ for electrons

Using the expression for ρ for an oscillation near the reflection point, it is possible to estimate $\rho=\gamma\theta_b$ for positrons and $\rho= 0.5\gamma\theta_b$ for electrons. At $\rho=1$, E corresponds to 12 GeV for positrons and 24 GeV for electrons for the (110) and (111) planes of a single silicon crystal.

An estimation for emitted photons energy range is given by the equations [4.8]

$$\omega = \frac{2\gamma^2\omega_0}{1+\rho/2} \qquad \text{(Eq. 4.1)}$$

$$E_{\gamma,\max} = \frac{\hbar\omega E}{E+\hbar\omega} \qquad \text{(Eq. 4.2)}$$

where $\omega_0=2\pi/T$ and T is the period of one oscillation in channeling or VR regime. These relations are written for the radiation first harmonic and for the case of an infinite periodic motion. In other words, Eqs. (3.1) and (3.2) define the maximum energy, while the minimum energy is close to zero. Nevertheless, the estimations computed with these relations are in good agreement with calculations (in fact, when $\rho \le 1$ the first harmonic gives the main contribution to the radiation).

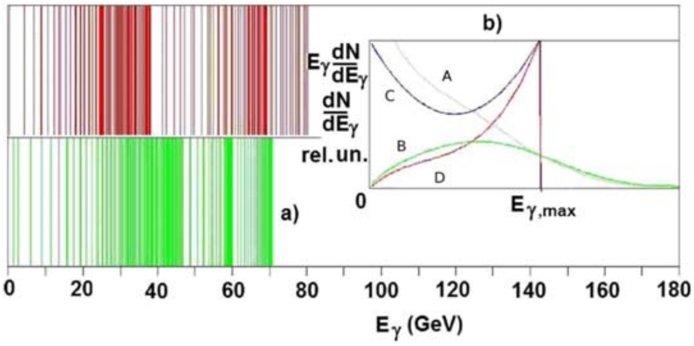

Figure 4.9 Maximum energies of the γ quanta (a) calculated according to Eqs. (3.1) and (3.2) from the corresponding frequencies of the motion. Red (top) and green (bottom) lines correspond to 180-GeV/*c* positrons and electrons, respectively. The shapes (b) of the γ-quantum spectra and energy losses in periodic structures: the gray (*A*) and green (*B*) curves are the spectrum and distribution of energy losses for a structure with one period. The blue (*C*) and red (*D*) curves are the same values but for an infinite periodic structure.

Fig. 4.9 shows the energy range of the emitted γ-quanta calculated according to Eqs. (3.1) and (3.2): for every oscillation the γ parameter was found and the corresponding energy was represented in the figure by a vertical line. Figure 4.9b shows the behavior of the intensity and the number of γ's as a function of the energy for a simple harmonic motion. Maximum energies of the γ quanta (a) calculated according to Eqs. (1) and (2) from the corresponding frequencies of the motion. Red (top) and green (bottom) lines correspond to 180-GeV/c positrons and electrons, respectively. The shapes (b) of the γ-quantum spectra and energy losses in periodic structures: the gray (A) and green (B) curves are the γ spectrum and distribution of energy losses for a structure with one period. The blue (C) and red (D) curves are the same values but for an infinite periodic structure. In a periodic structure (like an undulator) when this structure has only one oscillation and an infinite number of periods. Even if in the one-period structure the energy could exceed the maximum energy $E_{\gamma,max}$, it is possible in any case to use Eqs. (1) and (2) to estimate the radiation spectra because the number of emitted γ quanta rapidly decreases above $E_{\gamma,max}$. The greater $E_{\gamma,max}$ the smaller the probability of radiation of the first harmonic as a whole. The relation $I_{max}=[1+(1+x)2](1-x)/x$ (from the theory of coherent bremsstrahlung [4.11]) describes the relative variation of radiation intensity as a function of x:

in the considered case, $x = E_{\gamma,max}/E$. This behavior is due to an increase of the longitudinal recoil momentum and hence a decrease of the process formation length.

The expected radiation energy spectrum peaks approximately at 35 and 45 GeV for positrons and electrons, respectively; the predicted number of γ's can be observed up to 70–80 GeV for positrons and up to 70 GeV for electrons due to the influence of the narrow plane. It is clear that the present semi qualitative study is valid for electron (positron) beams (and silicon crystals) in the range of hundreds of GeV: at energies >1 TeV the synchrotron-like character of the radiation in a thin crystal should become the dominant one.

4.3.2 Experimental setup

The experimental setup, represented in Fig 4.10 is an improved version of the currently used setup to study beams deflection.

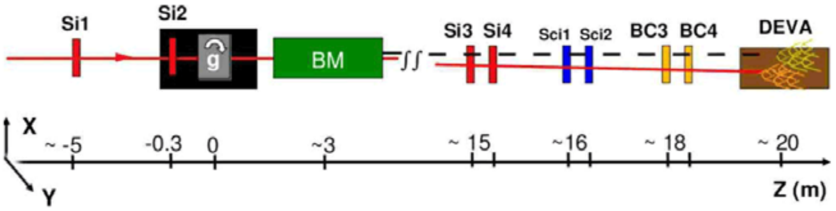

Figure 4.10 The setup: the microstrip silicon telescope (Si*X*), the high-precision goniometer (g), a bending magnet (BM), the 9.5X9.5 cm^2 silicon beam chambers (BC3, BC4), a pair of scintillators (Sci*X*), and the electromagnetic calorimeter (DEVA).

The incoming particle trajectory (with respect to the crystal orientation) is computed with the silicon telescope detectors already described. Si1 and Si2, while the outgoing one is based on the information from Si2 and BC3 (because of multiple scattering, BC4 is used in place of BC3 only in the case of a missing hit on BC3 due to a dead channel). The beam particles (which could be light leptons, muons, or light hadrons) are "discriminated" by an electromagnetic lead-scintillator calorimeter (DEVA) that can also be used in the trigger system (together with a pair of scintillators Sci*X*). DEVA is formed by 12.2 cm-thick (15x15 cm^2) scintillator tiles and 11 lead tiles (for a total of 13.07X_0): the scintillator light is brought out to a 16-channel photomultiplier tube (PMT, H7546, Hamamatsu) by 2 mm diameter wavelength shifter (WLS) fibers. The beam is formed by muons (65%), hadrons (12%), and light leptons (23%). In order to collect just the most interesting events, DEVA was part of the trigger, using as a signal the coincidence of the last two scintillators tiles. In the analysis, an event has been identified as a light lepton if its signal overcomes an energy threshold of 10.000 analog-to-digital conversion (ADC) units. For these preliminary studies on radiation, a ~2cm diameter quasimosaic crystal (named QM2) and a 2x2 cm^2 one (named QM1) have been used. The first crystal has a thickness along the beam of 840 μm and was bent at *R*=12m, the second one is 900 μm thick, and bent at *R=9* m. Both of them offers (111) channeling planes.

After lateral alignment of the crystal to the beam, an angular scan is performed, see Fig 4.10. The VR region is largely spread along the lower vertical direction, this is due to particles which lost energy in the VR process and are largely deflected.

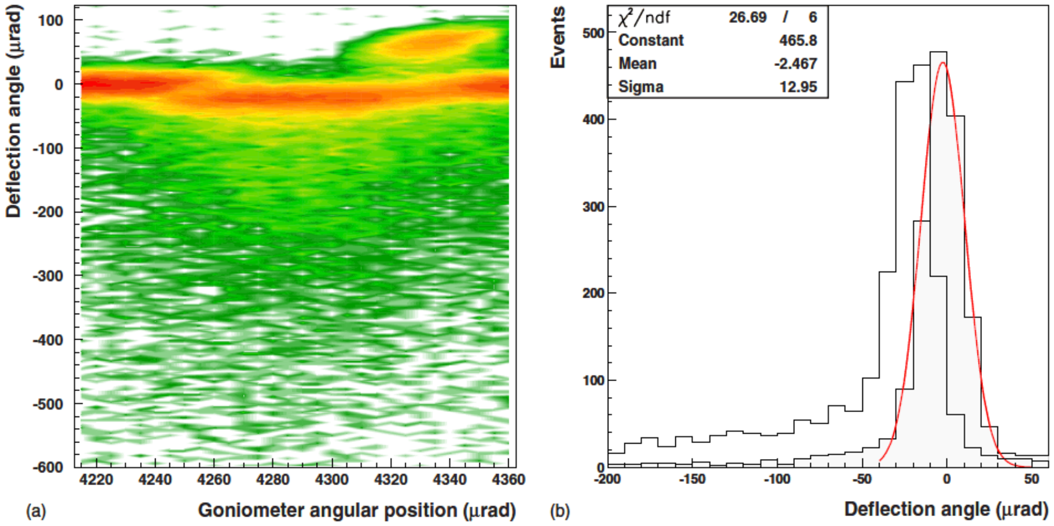

Figure 4.11 a) Angular scan: the *x* axis is the goniometer angle, that is, the crystal angle with respect to the beam, and the *y* axis is the deflection angle defined as the difference between the incoming and the outgoing angles. (b) The deflection angle distributions in the amorphous (gray) and VR (white) positions: the particles in volume reflection are steered by about 25 μrad with a high efficiency. The VR Gaussian left tail (which corresponds to the particles that have lost energy) is much higher than the amorphous one.

4.3.3 The spectrometer method

The radiation spectrum can be evaluated by exploiting what can be defined as a spectrometer method, which is schematically shown in Fig. XX.

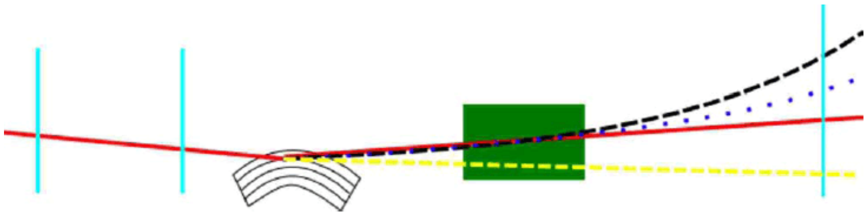

Figure 4.12 The spectrometer method: a particle in VR can emit photons (yellow dashed line), decreasing its momentum. A bending magnet steers particles depending on their momentum: the solid red line corresponds to a 180-GeV/c particle, while dashed black and dotted blue lines correspond to particles that have lost energy. Silicon detectors are able to reconstruct the particle trajectories.

A particle that impinges onto the crystal can be in the amorphous, volume-reflection, or channeling state depending on the incoming angle with respect to the crystallographic plane. In all these conditions, the particle can emit photons (yellow dashed line) and lose momentum. In a bending magnet a particle is deflected depending on its momentum, following the equation

$$p\vartheta = 0.3BL \qquad \text{(Eq. 4.3)}$$

where p is the particle momentum (GeV/c), θ the deflection angle (μrad), B the magnetic field (T), and L the magnet length (m). In this experiment BL=1.041 Tm); for unperturbed particles it is possible to define θ_0=0.3 × 1.041/180=1735 μrad.

Considering Eq. (3), a deflection angle distribution can be translated into an energy loss one: the main peak corresponds to the 180 GeV/c particles, while the tail is due to the particles that have lost part of their energy. Fig. 4.13 shows the energy loss distribution for the VR case. Finally, the energy spectra *dN/dE* vs *E* can be computed: the number of particles in a given bin is divided by the bin width energy value and normalized. The normalization is given by the number of particles in the energy loss distribution (*N*); events with an energy smaller than 0 GeV or greater than 180 GeV are due to the system intrinsic resolution.

The errors on the experimental energy spectrum are given by the uncertainty on the particle numbers in a given bin:

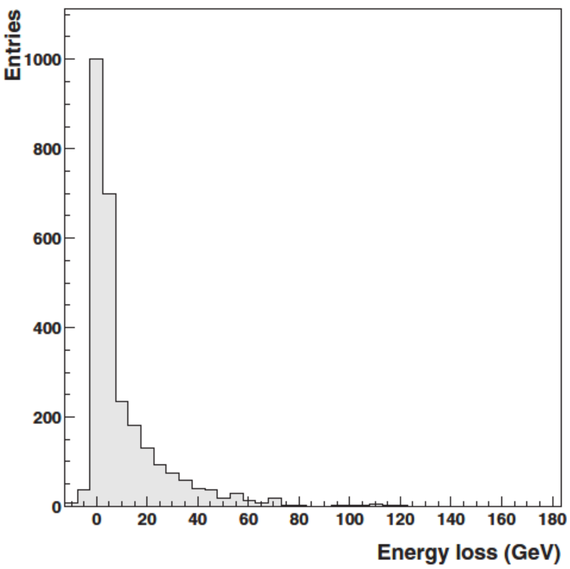

Figure 4.13 Energy loss distribution for the volume-reflection case.

$$\sigma^2_{dN/dE} = \frac{1}{(NdE)^2} dN \qquad \text{(Eq. 4.4)}$$

As far as the momentum uncertainty is concerned, it is evaluated according to Eq. 4.3

$$\sigma^2_{loss} = \left(\frac{0.3BL}{(\theta - \theta_0)^2} \right)^2$$
$$\sigma^2_{\theta} = \frac{(180 - p)^4}{(0.3BL)^2} \sigma^2_{\theta} \qquad \text{(Eq. 4.5)}$$

σ_θ is the angular error mainly due to the multiple scattering contribution of the material before the bending magnet and is of the order of 15 μrad.

4.3.4 The amorphous contribution

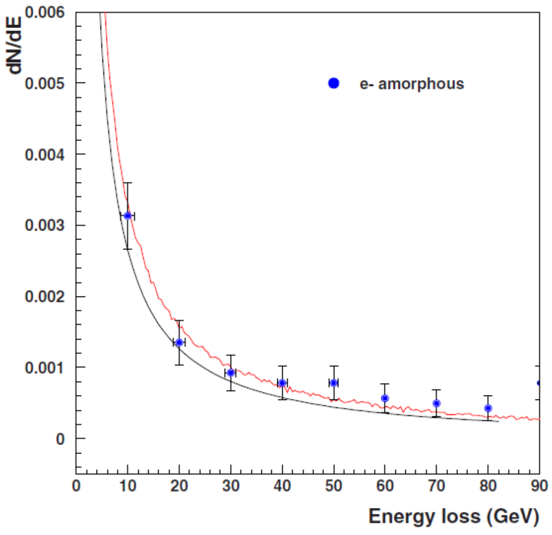

Figure 4. 14 Amorphous spectrum for an electron beam: the figures show a good agreement between experimental data (blue dots) and calculated (black line) and simulated (red line) ones.

The amorphous spectrum is given by the bremsstrahlung radiation in the different materials before the bending magnet; a positron that loses energy after the magnet cannot be distinguished from an unperturbed one, so the materials after the magnet must not be taken into consideration. The materials before the bending magnet were (1) two silicon detectors (2x300 μm); (2) four aluminum sheets in the detector active windows (4x20 μm); (3) six beam pipe flanges (Mylar) (6x180 μm); (4) about 3m of air; and (5) the quasi-mosaic crystal (~900 μm).

The amorphous radiation spectrum has been simulated in two ways: by considering the analytical calculation [4.4] and by a GEANT3 simulation. The experimental data have been compared with the simulation ones: Fig. 4.14 shows the comparison between the experimental data (blue dots) and the calculated (black line) and simulated ones (red line) for electrons.

4.3.5 VR Spectra

The volume reflection radiation experimental data have been compared with the simulation ones as shown in Fig. 4.15(a) [Fig. 4.15(b)] for positrons (electrons). As stated in Sec. II, radiation is usually described in terms of energy loss, that is, as *(dN/dE)E* vs *E*. Figs. 4.16(a) [Fig. 4.16(b)] shows the experimental results (blue dots for amorphous and red or green dots for VR) compared with the calculated ones (black lines) for positrons (electrons).

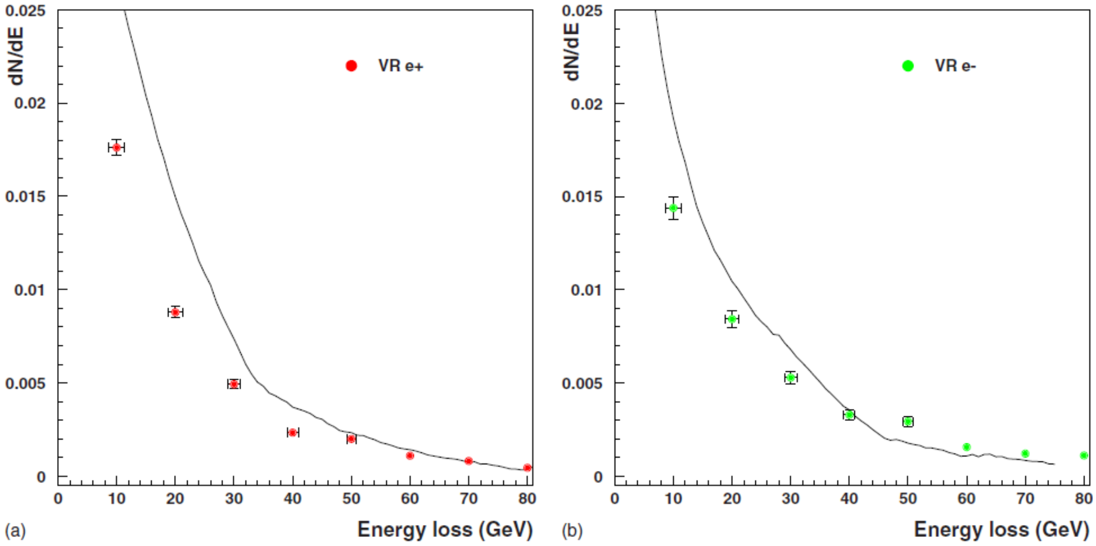

Figure 4.15 Volume-reflection spectrum for positrons (a) and electrons (b): experimental data (red and green dots) are compared with the calculated ones (black line).

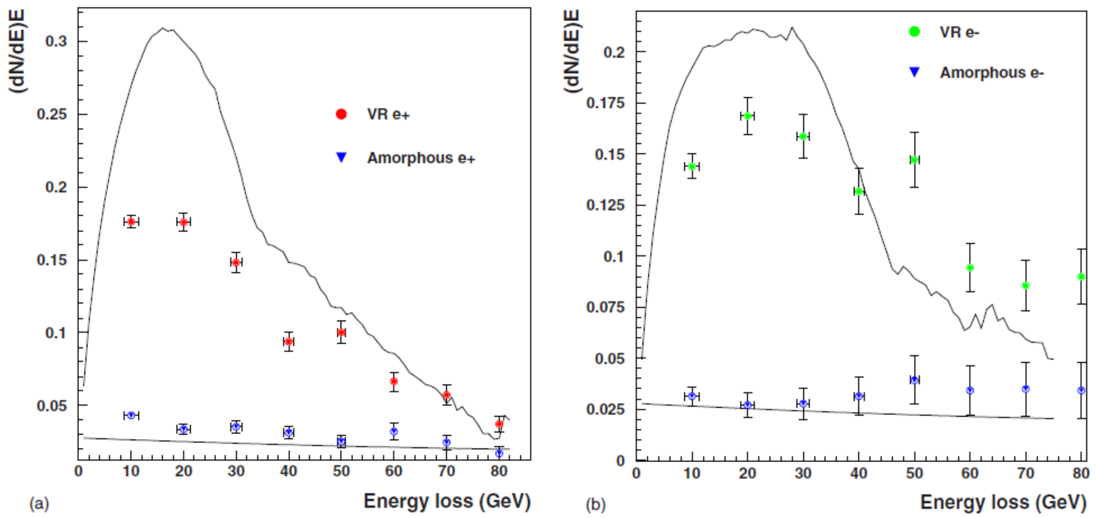

Figure 4.16 Energy loss spectra [(*dN/dE*)*E* vs *E*] for the positron (a) and electron (b) cases: the blue dots are the experimental amorphous data, the red and green dots represent the volume-reflection experimental results, the black lines identify the volume reflection and amorphous calculated spectra.

The comparison between the experimental and calculated energy loss spectra suggest the following considerations.

(1) There is good agreement between the experimental and calculated energy ranges of emitted γ-quanta for positrons and electrons with these ranges corresponding to the ones in the semiquantitative analysis of previous section.

(2) The experimental energy losses are smaller than the computed ones by a factor ~1.7 for positrons and ~1.2 for electrons.

(3) There is good agreement between experimental and computed spectra for the nonoriented case.

The theoretical calculation method has been described in [4.12] and is based on quasiclassical considerations of QED processes in electric fields [4.8]. Because of the integration of strongly oscillating functions, the radiation calculation is very complicated and some simplifications of the volume-reflection process have been made. Moreover, in this paper, an averaging procedure over all the particle trajectories has been introduced, in contrast to [4.13]. Taking into account these considerations, the observed disagreement can be explained as follows.

(1) Multiple scattering of particles on the crystal atoms has not been considered in the analytical calculations.

(2) The presence of nonhomogeneity of the quasimosaic crystal structure and in particular the dependence of the bending radius on the particle hit position and the torsional effect due to the holder.

(3) A consistent number of particles (10–15 %) may be captured in the channeling regime; even if they can exit channeling quickly, the motion changes.

(4) The radiation of two or more γ quanta by one particle has not been considered in the calculation.

Radiation emitted by light particles volume-reflected in bent crystals is still an unexplored field from the experimental point of view. The realized study presented has been performed at the CERN SPS H8 line with 180-GeV/c volume-reflected electrons and positrons and a quasimosaic crystal. The radiation spectrum has been measured with a silicon-based spectrometer allowing a resolution better than 1.5 GeV. Experimental data, the analytical calculation and simulation show good agreement for the amorphous case. As far as the spectrum in the VR case is concerned, the energy loss is lower than expected from the calculation; the possible reasons for the disagreement have been considered.

4.5 Discussion

The above experiments showed the possibility to efficiently deflect negatively charged high-energy particle beams. Among the studied steering mechanisms, axial channeling offers the highest efficiency. Such study opens up the possibility to efficiently manipulate the trajectories of negatively charged particle beams through coherent interactions with a bent crystal. In particular, accelerators under construction may take advantage of this know-how, adopting collimation systems based on crystals. Among them we could quote FAIR, which is expected to operate with antiprotons having an energy as high as 15 GeV. Crystal channeling technology can also find application in a variety of experiments having energy in the range of

1 GeV, such as MAMI, Dafne and KEK. At this energy, a high deflection efficiency can only be obtained with very thin crystals described in chapter 2.

Several applications can be foreseen also for radiation emitted by light particles in bent crystals at volume reflection; a very preliminary list could be the following:

(1) the generation of intense γ beams for a positron source [4.14];

(2) the generation of positron beams at a future linear collider [4.15]

(3) VR radiation could be used to monitor the proper working conditions of a crystal used as beam deflector

(4) the generation of intense γ beams for medical applications.

New tests are foreseen by the collaboration with an improved experimental setup (calorimeters to tag electrons and to measure the photon spectrum, reduction of the multiple scattering due to air, selection of a dedicated crystal) at low and high energy in the near future to characterize steering effects and to study emission of radiation in bent crystals.

References

[4.1] H. Backe *et al.*, Nucl. Instrum. Methods Phys. Res. B. **266** 3835 (2008)
[4.2] J. F. Bak *et al.*, Nucl. Phys. A. **389** 533 (1982)
[4.3] A. Baurichter *et al.*, Nucl. Instr. and Meth. B. **119** 172 (1996)
[4.4] V. A. Maisheev, Phys. Rev. ST Accel. Beams. **10** 084701 (2007)
[4.5] A. M. Taratin and Vorobiev S. A., Phys. Lett. A. **115** 401 (1986)
[4.6] V. A. Arutyunov *et al.*, Nuclear Physics B. **363** 283 (199)
[4.7] Y. A. Chesnokov *et al.*, JINST. **3** P02005 (200)
[4.8] V. N. Baier *et al.*, *Electromagnetic Processes at High Energies in Oriented Single Crystals*. 1998, Singapore: Word Scientific.
[4.9] V. A. Arutyunov *et al.*, Nuclear Physics B. **363** 283 (1991)
[4.10] E. N. Tsyganov, Fermilab Preprint TM-682, TM-684 Batavia (1976)
[4.11] H. Bilokon *et al.*, Nucl. Instrum. Methods Phys. Res. B. **204** 299 (1983)
[4.12] V. M. Biryukov *et al.*, *Crystal Channeling and Its Application at High-Energy Accelerators*. 1997 Berlin: Springer.
[4.13] Y. A. Chesnokov *et al.*, JINST. **3** P02005 (2008)
[4.14] T. Suwada *et al.*, Phys. Rev. ST Accel. Beams. **10** 073501 (2007)
[4.15] A. Seryi *et al.* in Proceedings of the Particle Accelerator Conference PAC 07, Albuquerque, New Mexico, 2007 (unpublished). 2007.

Chapter 5

The UA9 experiment

5.1 The problem of collimation in the LHC

Halo collimation is an essential part of a particle accelerator and is a not trivial aspect for any particle accelerator operating at high intensity such as the LHC.

LHC halo, which is being generated due to beam dynamics like beam-beam interaction and scattering on the residual gas in the vacuum system, may in fact cause super-magnet quenching and radioprotection issues. LHC nominal working conditions would allow to circulate two 7 TeV protons beam, each of them will store an energy of 362 MJ [5.1], a fraction of about 10^{-9} of the full beam could already quench a magnet [5.2].

Traditional collimation systems are based on the use of massive amorphous elements that intercept and absorb beam halo particles. In high energy accelerators like the Tevatron and LHC the high stored energy requires the use of a more sophisticated collimation.

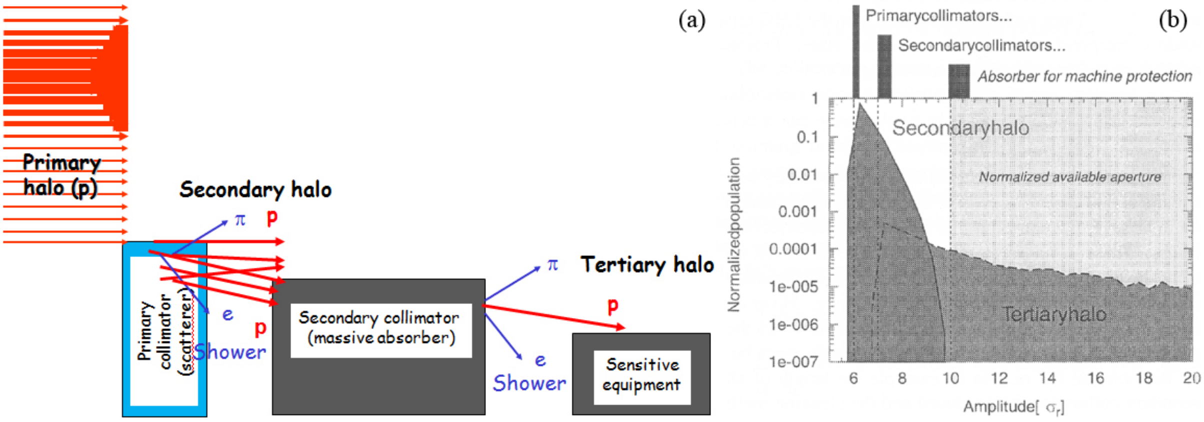

Figure 5.1 (a) scheme of collimation system for collimation in high energy accelerators. Primary halo beam is scattered by a first element, which generates a secondary halo beam intercepted by a massive collimator, the tertiary halo beam generated in this interaction is intercepted by a third massive collimator. (b) Population of secondary and tertiary halo.

The LHC collimation scheme is based on

1) A first stage equipped with a short primary collimator to intercept the halo at 6σ with impact parameter between 100nm and 1µm. This generates a "*secondary halo beam*" with largest divergence.
2) The second stage is equipped with secondary massive collimators which intercept the beam at 7σ with impact parameter of 200 µm. The largest halo fraction is intercepted by this second stage, while the remaining part originates a "*tertiary halo beam*".
3) Other absorbers and collimators are placed to intercept the tertiary halo at 10σ along the ring.

At the present time LHC is still not operating at the nominal luminosity and energy, and a collimation system based on traditional schemes has already been installed. Due to the high intensity at which LHC is planned to operate in the future, an improved collimation system is needed. Such system will require the use of many collimators [5.2, 3] and will be more complex. As will be shown in the following, the use of bent crystal may assist traditional collimation schemes

Thus, following the positive results of beam extraction and collimation in Tevatron [5.4-6], SPS [5.7] and IHEP [5.8, 9] and basing on the results of the campaign research illustrated in chapter 3, the UA9 collaboration started in 2009 an experiment at CERN with the aim to collimating the beam circulating in the SPS by using bent silicon crystals. Differently from a massive collimator that spreads the halo, a bend crystal coherently deflects all the particles to the same direction and allows collecting them onto a massive absorber. The UA9 setup is installed in the two-dipole empty cells of the straight section 5 of the SPS, across the cavern previously hosting UA1. UA9 alternates the use of four single crystals operating in planar channeling. Two of them are already operational; the other two were recently installed and will be operated in 2010.

The mechanism of interaction through planar channeling has been preferred to the other schemes in section 3.8 because it allows inserting a minimum amount of material across the beam, because channeling can be easily operated with the same crystal at any energy and satisfies the need for an easy and fast alignment of the crystal with the beam.

5.2 The UA9 experimental setup

The experimental setup of the UA9 experiment is based on:

- a tank inside of which two crystals, a Cherenkov detector, and a thin tungsten target have been installed. The tank contains three feed-through for 100 cables, which in future may be needed to drive a piezoelectric system for alignment of the crystals in multi-crystal assemblies.

Figure 5.2 the UA9 tank with installed crystals and the tungsten scatter

- The ST9 strip crystal ST9, extensively tested on H8 external line (2mm thick along the beam) and a quasi mosaic crystal tested on H8 line 1 mm thick along the beam.

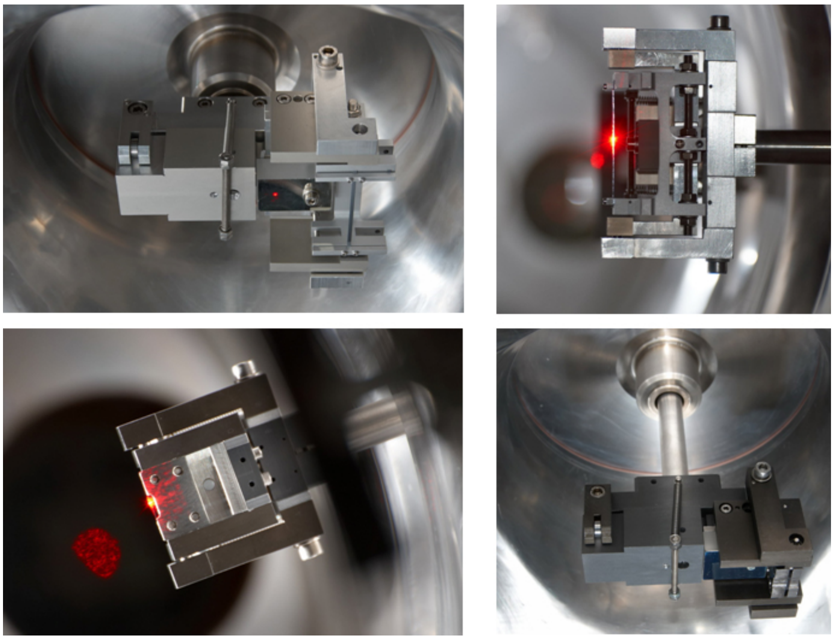

Figure 5.3 different views of ST9 strip crystal (upper crystal) and the quasi mosaic crystal mounted on their holder and installed in the UA9 tank. The red spot is the spot of a laser beam used to pre-align the crystal to the beam.

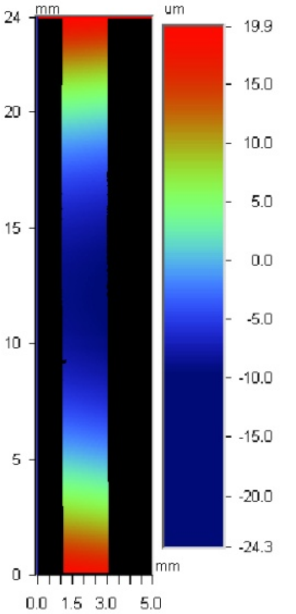

Figure5.4 shape of ST9 strip crystal measured by white light interferometry techniques prior to insertion in the UA9 tank.

The strip crystal ST9, was bent at a bending angle of 140±10 μrad and torsion was adjusted to 4.8±1 μrad/mm, crystal bending parameters was checked by optical interferometry (Veeco NT1100), see Fig 5.4.

- Two goniometers with an approximate resolution of 10 μrad, i.e. of the same order of the critical angle for channeling.
- A pre-alignment system used to pre-align the crystal to the beam based on a self-built autocollimator with resolution of few μrad and different optical components to align the crystal surfaces to the axis of the tank.
- A quartz which is used as Cherenkov detectors to count the number of particles impinging on the crystal.
- A movable thin target made of tungsten, used as primary collimator to compare its performance with the crystals ones
- In the upstream and downstream regions of the tank two gas electron multipliers (GEM) detectors. Their counting rate is proportional to the background. When the crystal is on the beam the count rate of the downstream GEM becomes proportional to the rate of nuclear reactions in the crystal.
- A scintillator telescope, which provides information similar to the ones provided by the GEM detectors.
- A collimation tank containing a tungsten absorber 600mm long and 30x30mm^2 wide.
- A set of beam loss monitor (BLM) used to detect beam losses.
- A Medipix [5.10] detector used for imaging purposes of the deflected beam and to measure the collimation efficiency.

- A prototype of LHC collimator based on a massive absorber, used to measure the collimation efficiency and for comparison purposes.

Figure 5.5 shows the layout and the main components of the UA9 experiment, while Fig 5.6 shows a schematic representation of the UA9 tank and components installed inside of it.

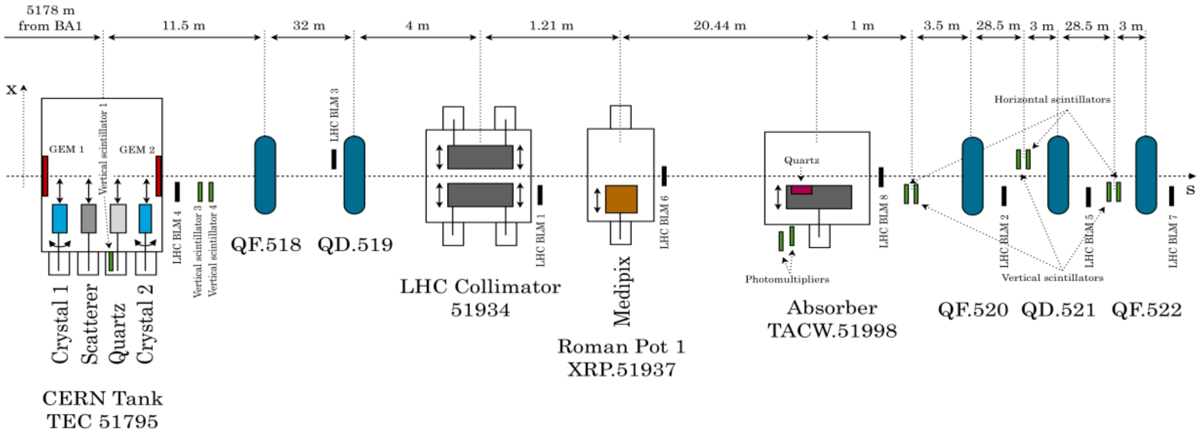

Figure 5.5 the layout of UA9 experiment

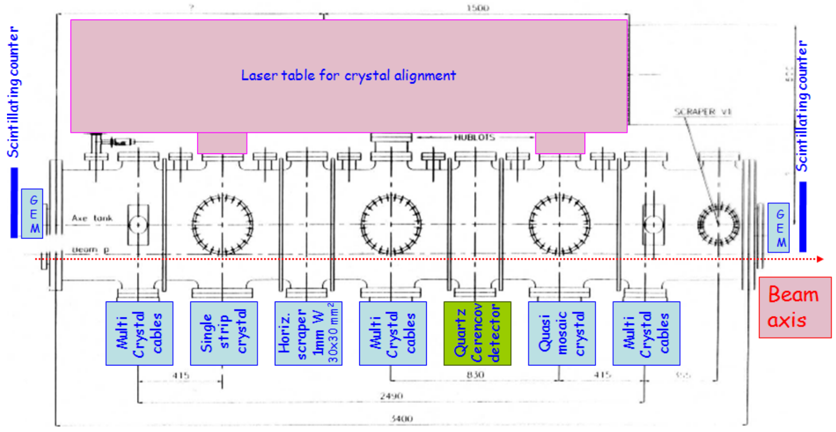

Figure 5.6 A scheme of the UA9 tank and the components installed inside of it.

5.3 UA9 preliminary results

In 2009, 5 dedicated runs were assigned to UA9 experiment. Protons circulated at 120 GeV in storage mode with 10^9 to 10^{12} stored particles. Under this condition the SPS is very stable, beam lifetime lasts in fact 80 h, and so a diffusive halo of a few 10 to 10^3 particles per turn was realized by perturbing the beam.

After a lateral positioning of the crystal with respect to the beam at 6σ from its axis, the crystal was rotated in order to find the channeling position. Interaction with the beam was detected by measuring the nuclear interaction losses with the beam loss monitors, the GEM detectors, the scintillators telescope and with the Medipix detector.

Fig 5.7 shows the nuclear interaction losses measured with the scintillators telescope when the ST9 crystal is on the beam. From left to right the crystal is oriented with respect to the beam in “amorphous condition”, then in channeling, in VR and again to “amorphous”. Interaction between the crystal and the beam increases or decreases the losses of the SPS as function of the angular alignment position. In particular, alignment in channeling position decreases the losses by a factor of 5.

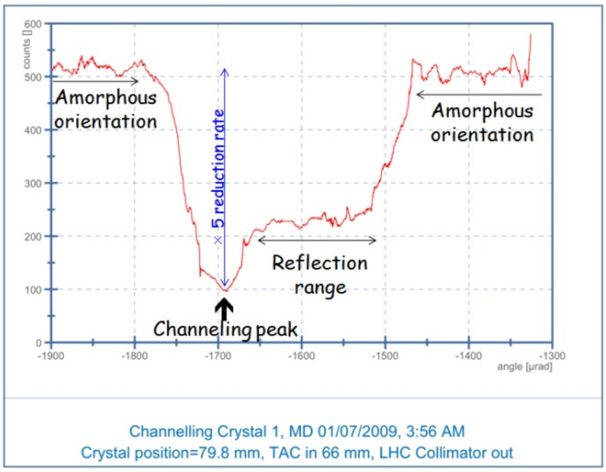

Figure 5.7 measurement of nuclear losses obtained with a scintillators telescope placed downstream the crystals.

Fig 5.8 shows the signal from GEM detectors, obtained in a wider angular range.

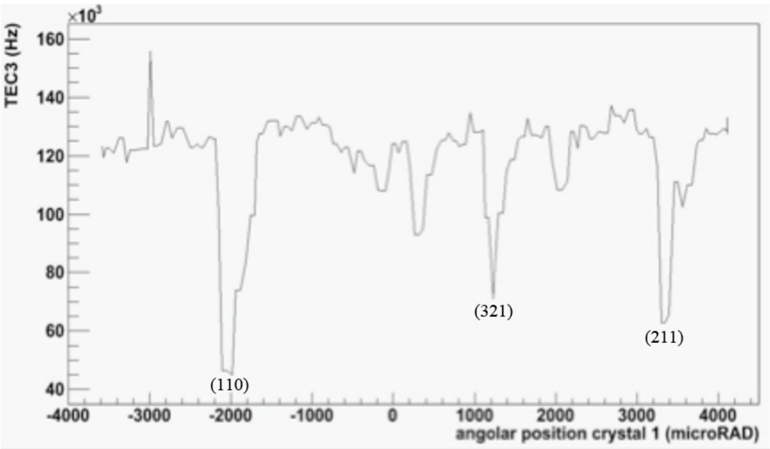

Figure 5.8 channeling and VR from main plane and skew planes observed on the SPS circulating beam

The most intense peak corresponds the (110) main plane, while the less intense ones correspond to channeling from different planes, whose angular positions are labeled in Fig 5.8. In order to avoid the detection of skew planes the crystal should have been installed with a larger tilt of the crystal axis with respect to the beam direction.

Fig 5.9a shows the deflected beam as seen by a Medipix detector, while Fig 5.9b shows the beam profile corresponding to the maximum position of the peak.

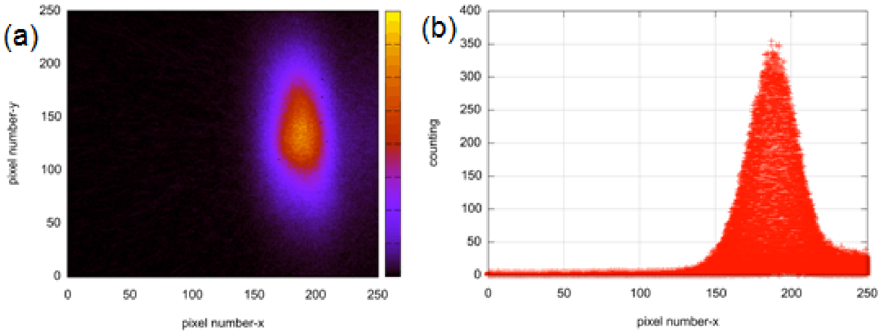

Figure 5.9 deflected beam as seen by Medipix detector (a) the beam impinging on the detector (b) the beam profile in the maximum region

The different detectors used in the UA9 experiments showed a clear evidence of channeling and volume reflection phenomena in the interaction between the crystals and the circulating beam. Collimation efficiency have been measured with two distinct methods.

5.3.1 Collimation efficiency measurement

Collimation efficiency is defined as the ratio between the number of particles deflected by the crystal and the number of particles interacting with the crystal. Experimental determination of collimation efficiency relies on two methods.

5.3.1.1 The LHC collimator scan

A lateral scan was performed with the LHC collimator, in order to make it partially or fully intercept the channeled beam as shown in Fig 5.10.

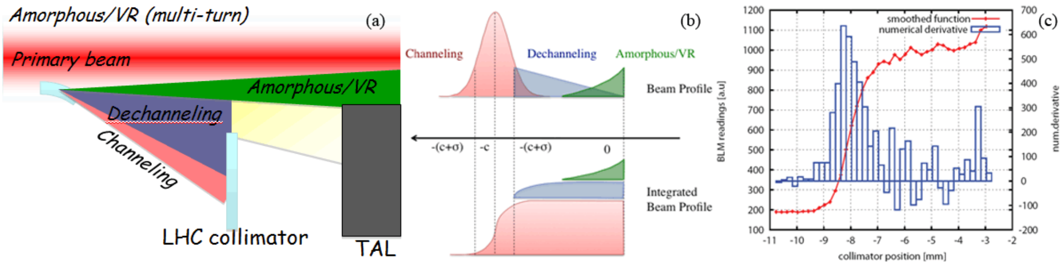

Figure 5.10 (a) schematic representation of collimation efficiency using LHC collimator scan (b) The BLM readings as function of the LHC collimator position. When the collimator intercept the channeled beam there is a decrease in the BLM readings.

Variation in the lateral position of the LHC collimator causes a change in the signal collected by the beam loss monitor, whose shape is the integrated beam profile (see Fig 5.10c). Data collected during the LHC scan allows calculation of the number of particles impinging on the crystal and, knowing the distance between the crystal and the LHC collimator, to measure the deflection angle. This kind of measurements suffer from a large uncertainty, as different measurements gave significantly different values [5.11] .

Very preliminary estimations of the collimation efficiency reached with the quasi mosaic crystal is as high as 77.4%, while with the strip crystal we obtained an efficiency of 74% [5.11].

5.3.1.2 Collimation efficiency using Medipix

A second method to measure collimation efficiency relies on measuring, vs. time, the number of circulating particles at $t=t_0$ and subtracting from this value the number, the particles being counted by the Medipix detector, i.e. the number of particles deflected by the crystal. Comparison of this value with the number of circulating particles is shown in Fig. 5.11.

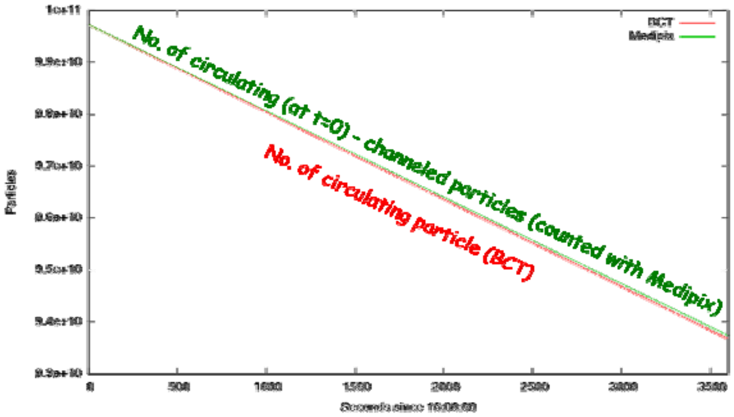

Figure 5.11 Measurement of collimation efficiency using Medipix. In green the difference between the number of circulating particles at t=t0 and the particles deflected by the beam and in red the number of circulating particles. Decrease of circulating particles is due only to interaction with the crystal.

As can be seen from Fig. 5.11, the decrease in the number of circulating protons is due only to the protons deflected by the crystal. This result showed collimation efficiency larger than 86%, and compatible with 100%.

6 UA9 future developments

Even if preliminary, the first results obtained by the UA9 experiment show the possibility to of beam collimation in circular accelerators and were very encouraging to continue the experiment. It is important to remark that silicon crystals are able to withstand high particles rates, as demonstrated in [5.4, 8, 12] and that beam extraction from circular accelerators have been already successfully achieved [5.4, 7, 8].

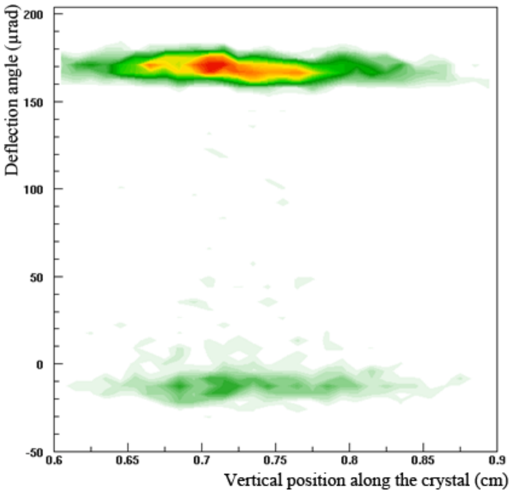

Figure 5.12 Beam deflection as function of vertical position along the St18 vertical position (characterization have been realized on H8 line)

Deeper investigation, which will be carried on in 2010, is needed to measure more precisely the collimation efficiency and to prove the possibility to use bent crystals in the LHC environment.

For this purpose, recently two additional single crystals, which will be operated in channeling mode at the energy of 270 GeV, have been installed in a second tank in the SPS circulating beam.

Both of them were preliminary characterized on the external line H8 with 400 GeV protons.

The strip crystal, which is 2mm thick along the beam, was bent at 176 μrad, and its torsion lowered to a negligible value of 0.6 μrad/mm (at 270 GeV energy the critical angle is about 40 μrad). Measured channeling efficiency is as high as 80%. The quasi mosaic crystal, which is 2mm thick along the beam, was bent at 150 μrad.

Data taking for such crystals will be done in 2010.

References.

[5.1] R.Schmidt *et al.* in Proceedings of PAC07,. 2007. Albuquerque, USA.
[5.2] C. Bracco, *École politecnique fédérale de Lausanne*. 2009.
[5.3] O. Aberle *et al.*, *CERN Report TS-2008-013*
[5.4] R. A. Carrigan *et al.*, Phys. Rev. ST Accel. Beams. **5** 043501 (2002)
[5.5] R. A. Carrigan *et al.*, Nucl. Instr. and Meth B. **119** 231 (1996)
[5.6] R. A. Carrigan *et al.*, Phys. Rev. ST Accel. Beams. **1** 022801 (1998)
[5.7] X. Altunab *et al.*, Phys. Lett. B. **357** 671 (1995)
[5.8] A. G. Afonin, Phys. Rev. Lett. **87** 094802 (2001)
[5.9] V.M.Biryukov *et al.*, *Crystal Channeling and its Application at High Energy Accelerators*. 1997, Berlin: Springer.
[5.10] http://medipix.web.cern.ch/MEDIPIX/.
[5.11] V.Previtali.Available from: http://indico.cern.ch/getFile.py/access?sessionId=8&resId=0&materialId=0&confId=71773.
[5.12] Baker *et al.*, Nucl. Instrum. Meth. B. **90** 119 (1994)

Conclusions

In this work we have shown the procedures developed at Sensors and Semiconductor Laboratory of Ferrara University to fabricate crystals through non conventional silicon micromachining techniques and their characterization in interaction with charged particle beams.

The crystals developed in this work have been positively tested at CERN external line H8 with 400 GeV protons and at H4 with negative particles, leading to the discovery of new coherent interactions between high-energy particles and a crystal and a consistent raising up of efficiency of more established planar channeling.

Among the different tested crystals, two of them have been selected for installation in the SPS and are successfully used by the UA9 collaboration in a collimation experiment with a 120 GeV proton beam circulating in the SPS. Preliminary results highlight very high collimation efficiency. This last observation opens up new perspective for crystal-assisted collimation in the LHC.